PLASMONIC INTERACTIONS IN GOLD::VANADIUM DIOXIDE HYBRID NANOSTRUCTURES

By

Davon Wayne Ferrara

Dissertation

Submitted to the Faculty of the

Graduate School of Vanderbilt University

in partial fulfillment of the requirements

for the degree of

DOCTOR OF PHILOSOPHY

in

Physics

May, 2011

Nashville, Tennessee

Approved:

Richard F. Haglund, Jr., Department of Physics and Astronomy

David E. Cliffel, Department of Chemistry

Leonard C. Feldman, Department of Physics and Astronomy

Anthony B. Kaye, Department of Physics and Astronomy

Thomas J. Weiler, Department of Physics and Astronomy

Sharon M. Weiss, Department of Electrical Engineering and Computer Science

To Mom, for setting the example.

ACKNOWLEDGMENTS

This dissertation would not have been possible without the support of many people. First, I would like to thank the Department of Physics and Astronomy and the Institute of Nano Science and Engineering (VINSE). There are many administrators, professors, and research associates who have provided the resources and behind the scenes support to keep everything from equipment to travel reimbursements working smoothly. This research was partially supported by the Office of Science, U. S. Department of Energy, under grant number DE-FG02-01ER45916. Additional research funds were provided by ITT Corporation's National Security Technology Applications Division. For their invaluable guidance and input, I want to thank my dissertation committee members: Professors Leonard C. Feldman, Sharon M. Weiss, David E. Cliffel, Thomas J. Weiler, and Anthony B. Kaye. Professor Kaye has also provided valuable guidance and mentorship as a collaborator over the past few years.

For their friendship, collaborations, and support, I would like to thank the other members of the Applied Optical Physics group and VINSE, both past and present: Jed Ziegler, Charlie Adams, Ben Lawrie, Krishen Appavoo, Joyeeta Nag, Andrej Halabica, Nicole Dygert, Stephen Johnson, Kevin Tetz, Eugene Donev, John Rozen, Jae Suh, Evan MacQuarrie, and Matthew McMahon. I especially want to thank Joyeeta for many fruitful discussions about vanadium dioxide. I would like to acknowledge Evan, whose undergraduate research efforts are not only an important part of this dissertation, but who has influenced my professional development in many ways.

To my Mom, Dad, Derrick, Danielle, my grandparents, and all of my family: Thank you! Ultimately, none of this would be possible without their support and patience throughout these years. A close friend, Heather Day, helped in proofreading this dissertation. Thank you!

Finally, a very special thanks to my adviser, Professor Richard F. Haglund, Jr., for his immense patience, understanding, and constant encouragement from the first years of graduate school to the last. For any research interest I expressed, no matter how "out there," his response was always encouraging.

Thank you!

PREFACE

> *It has long been an axiom of mine that the little things are infinitely the most important.* - from the Adventures of Sherlock Holmes, by Sir Arthur Conan Doyle

From Sherlock Holmes to Columbo, the great detectives tend to solve their cases by paying attention to the little details that would not seem to matter to most people. As detectives of nature, scientists gain a better understanding of the world around us by looking at "little things" for clues. In optics, little things are especially known to have big effects. Michael Faraday understood that the colors of certain solutions containing gold was due to the presence of small, colloidal particles.[1,2] Lord Rayleigh correctly explained the color of the sky to be the result of scattering by particles much smaller than the wavelength of visible light.[3,4] Atoms and subatomic particles are responsible for all macroscopic behavior of substances. Much of modern physics involves understanding how these tiny components dictate the properties of the solids, liquids, gases, and other phases of matter that make up our universe.

The latter half of the 20$^{\text{th}}$-century saw technological leaps that allowed very precise manipulation of particles from the micro- to the atomic-scale and has led to the birth of nanoscience and engineering. As fabrication techniques continue to improve, significant efforts have been devoted to the study of electromagnetic interactions with nanostructures, known as nano-optics. Furthermore, because of their ability to concentrate electromagnetic energy into small volumes and their relatively easy to manipulate optical properties, interactions specifically between *metal* nanostructures and photons have garnered much scientific interest. In metal nanostructures, the collective oscillation of the free electrons dominates the optical properties of the structure below the plasma frequency. This fundamental excitation is known as the *surface plasmon resonance* and defines the subfield known as *nanoplasmonics*.[5] In nanoparticles (NPs) this oscillation is known as a *localized* surface plasmon resonance (LSPR). Reference [5] provides a good introduction to the subject of plasmonics.

The applications of nanoplasmonics are broad. Nanoscale manipulation of EM energy and structures have led to applications such as using metal nanostructures to detect brain activity, sense biomolecules, or focus EM energy into small volumes using a tapered metal waveguide.[6–8] A major concentration of research involves the control of macroscopic optical properties based on the collections of individual nanostructures. Examples include broadband polarizing filters made from silver nanoparticles (e.g., Thorlabs, product number LPVIS100), EM cloaking devices, and negative-refraction materials.[9,10] Many of these applications have led to a new class of man-made materials, known as *metamaterials*, where the subwavelength structures are used to create materials with optical behavior not found in nature.[5,11]

The work presented in this dissertation bridges the gap between nanoscale interactions and macroscopic control over optical properties by focusing on nanostructures

created by coating arrays of gold NPs with a vanadium dioxide (VO_2) film. The VO_2 semiconductor-to-metal (SMT) phase transition leads to a temperature-dependent shift in LSPR wavelength in the Au::VO_2 structure. Understanding the interactions between the Au NPs and VO_2 film is essential for designing applications using these hybrid structures. More specifically, the interaction of the Au NPs with the VO_2 interband transitions at energies centered at 1.4 eV leads to damped resonances that present a challenge for researchers looking to develop applications at visible to near-infrared energies.

In the following chapters, aspects of the structure will be explored in detail. Chapter I presents an introduction to plasmonics and VO_2, followed by a summary of the experimental methods and tools used for fabrication and optical measurement in Chapter II. Chapter III specifically deals with the interaction of single Au NP arrays with the VO_2 film. We show that the NPs can act as "nanoantennas" sensitive to small changes in the VO_2 optical properties during the phase transition. In Chapter IV, experiments with arrays of nanodimers, pairs of NPs, will show that the sensitivity of the LSPR to the VO_2 phase transition can be increased in systems of coupled particles. Chapter V will report a 37% decrease in threshold power for switching VO_2 using low-power laser heating, demonstrating that the coupling between the NPs and the film can enhance the photochromic behavior of the composite structure over the plain film.

As with all relevant scientific research, the little things that we study in order to answer the questions of nature lead to more unanswerable questions concerning "little things." In Chapter VI, the story will conclude with a discussion of some of these unanswered questions and the impact this work has on the field of nanoplasmonics. The vivid colors of the 13^{th}-century stained glass windows featured in Figure 1.6 and the unique dichroism of the 4^{th}-century Lycurgus cup (Figure 1.5) are both due to the presence of metal NPs demonstrating that a collection of little things can have a major impact on the larger picture.

TABLE OF CONTENTS

LIST OF ACRONYMS

BR	Bruggeman effective medium
EBL	Electron beam lithography
EDA	Electrostatic (quasistatic) dipole approximation
EM	Electromagnetic
FDTD	Finite-difference time-domain algorithm
FE	Finite element analysis
FF	Flat field
FOM	Figure of merit
FWHM	Full width half maximum
FW90M	Full width 90% maximum
ITO	Indium-tin-oxide
JC	Johnson and Christy (Au dielectric function)
LD	Lorentz-Drude model (dielectric function)
LSP	Localized surface plasmon
LSPR	Localized surface plasmon resonance
MG	Maxwell-Garnett effective medium
N. A.	Numerical aperture
NC	Nanocomposite
ND	Nanodimer
NIR	Near infrared
NP	Nanoparticle

PLD	Pulsed laser deposition
PMMA	poly(methyl methacrylate) (EBL resist)
SEM	Scanning electron microscope
SG	Savitzky-Golay smoothing function
SMT	Semiconducting-to-metal (phase transition)
SRR	Split-ring resonator
VS	Visible

LIST OF TABLES

LIST OF FIGURES

CHAPTER I

INTRODUCTION

Hybrid nanostructures consisting of gold (Au) or other noble metals and vanadium dioxide (VO_2) have received much interest in the last several years in large part because of the ability to tune the optical properties of the structures in response to external stimuli such as incident light or heat.[12–23] This capability is of primary interest in the development of active plasmonic structures for use in such applications as optical switches, sensors, and metamaterials,[12,16,17,20–22] and recently, Au::VO_2 structures have shown promise at electromagnetic (EM) wavelengths longer than 1500 nm as possible optical limiters and modulators. Although designing structures that extend the wavelength range into the visible (VS) and near-infrared (NIR) spectrum is desirable for many applications,[21–24] the interband transitions of VO_2 lead to significant plasmon damping at evergies above 0.7 eV.[25,26] Figure 1.1 clearly demonstrates the difference in extinction efficiency for 140 nm particles in air compared to those covered by a 60 nm VO_2 film. Despite the challenge of adopting Au::VO_2 structures to applications in the VS, these structures present a unique opportunity to study the interactions between the fundamental free-electron excitation of a metal, the plasmon, and the strongly-correlated electronic behavior of the semiconductor-to-metal phase transition (SMT) of the VO_2. In particular, for Au nanoparticle (NP) arrays and VO_2 thin films at wavelengths between 600 and 1200 nm, the interactions between the Au plasmon and the VO_2 interband transitions crucially determine the optical character-

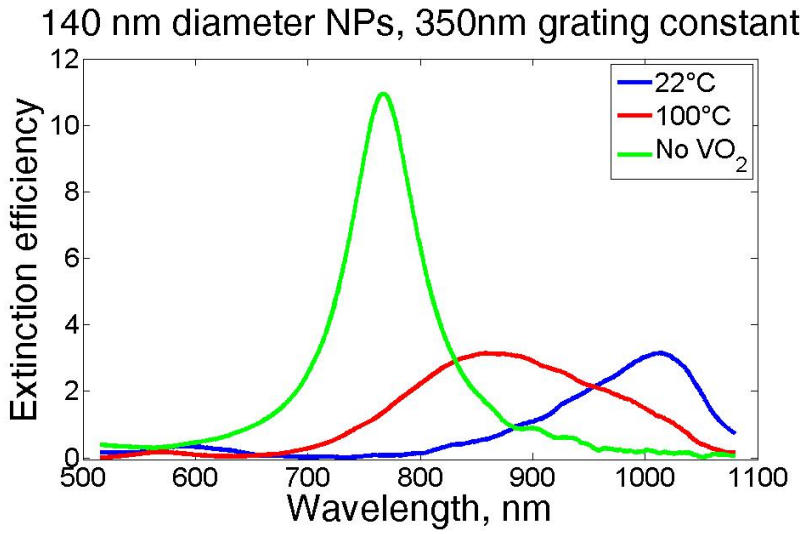

Figure 1.1: A comparison of the extinction efficiency for an array of 140 nm NPs in air versus coated with 60 nm of VO_2. The array was used in the experiments described in Chapter V.

istics of Au::VO_2 structures and lead to several interesting results. Section 1.1 will further discuss the motivation for this dissertation in the context of current research and summarize the experimental results of this dissertation.

The rest of this chapter discusses the theoretical background necessary to understand the results presented in Chapters III through V. Section 1.2 reviews resonant behavior of EM interactions with metal NPs embedded in a dielectric material. Sections 1.3 and 1.4 discuss the characteristics of the two primary materials studied in this dissertation, namely Au and VO_2 and include the physical interpretation of the dielectric function describing the material response to EM fields. The final section, Section 1.5, presents an outline for the rest of this dissertation.

1.1 Motivation and Background

Metal nanostructures are at the forefront of nanoscience and engineering research, at least partly due to their highly tunable optical properties and ability to focus EM energy into small regions. Both of these attributes are a result of the fundamental, collective oscillation of the free-electron gas in a metal known as a plasmon. In metal structures with characteristic dimensions of the same size or smaller than the wavelength of incident light, the localized surface modes excited by the EM field can exhibit resonant behavior that dominates the optical properties of the structure at a wavelength known as the localized surface plasmon resonance (LSPR). The study of EM interactions with metal nanostructures has become one of the cornerstones of nanoscience and technology research and defines the subfield of *nanoplasmonics*. Many possible applications of nanotechnology, including active plasmonics and metamaterials, optical switching, plasmonic transistors, and optical limiting, call for the ability to control the plasmonic response of the nanostructures in response to external stimuli such as heat, changes in incident light intensity, and chemical or biological contamination. Due to the sensitivity of the LSPR to the local dielectric function of the medium surrounding the structure, the use of thermochromic, photochromic, and electrochromic materials as embedding media have gained much attention (for examples, see [20, 27, 28]).

As demonstrated by several studies, hybrid structures consisting of Au nanostructures and VO_2 thin films provide this capability through the SMT of the VO_2.[12–20, 22, 23] Metal::VO_2 hybrid structures have an advantage over many other solid-solid transition

materials because the critical temperature at which the transition occurs, approximately 68°C, is above room temperature. The key characteristic of hybrid metal::VO_2 nanocomposites (NC) is the resulting change in LSPR wavelength due to the SMT; for structures with metal NPs, the SMT blueshifts the LSPR for VS and NIR wavelengths, as seen in Figure 1.1.[12–17,19]

Most studies with Au::VO_2 structures focus on the temperature-dependent shift in the LSPR and the resulting change in overall transmission or absorption through the composite structure. Suh *et al.* and Seo *et al.* studied perforated Au and VO_2 films, and both observed a change in transmission upon the phase transition. In the case of the former, it was found that transmission for hole arrays at 800 nm increased by a factor of 8 in the metallic state over that of the plain film.[18] Seo *et al.* showed that for terahertz radiation, an extinction ratio of 10^5:1 can be achieved using arrays of Au nano slot antennas in conjunction with a VO_2 film, seen in Figure 1.2.[20] Driscoll *et al.* and Dicken *et al.* fabricated structures consisting of noble metal split-ring resonators (SRRs) and VO_2, shown in Figure 1.3.[21–23] Driscoll *et al.* showed that Au SRRs on top of a VO_2 film exhibited a tunable resonance around 1.5 THz that decreases as the VO_2 completes its phase transition due to the capacitative response of the SRR "shorting out."[22] Dicken *et al.* studied several configurations of Ag SRRs in contact with VO_2 films and even VO_2 SRRs at wavelengths between 1.5 and 5 μm, demonstrating that coupling the SRRs to other resonant structures or SRRs can lead to a narrower resonance width. Figure 1.3, from [21], shows the effect of switching the VO_2 in a Ag::VO_2 SRR. Dicken defines a figure of merit (FOM) as the ratio of the shift in LSPR position to the full-width half-maximum (FWHM) of the resonance; the

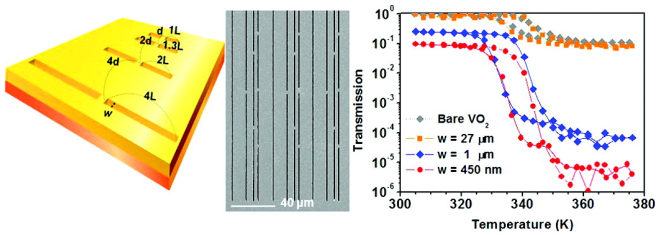

Figure 1.2: From [20], a metamaterial consisting of Au slot antennas on a VO_2 film.

largest FOM achieved in this study was 0.14.[21] Two notable theoretical studies for Au::VO_2 structures propose using Au::VO_2 structures to measure the Casimir force at a boundary and for a hybrid structure that self-regulates its temperature.[29,30] Studies on Au::VO_2 structures in the visible have been conducted using Au island films and Au suspended in a VO_2 matrix, both non-ordered structures.[12–16] This dissertation builds on the work by Suh *et al.*, who conducted the first study of Au::VO_2 structures on lithographically prepared arrays of Au NPs coated with 60 nm VO_2 and showed a shift in LSPR of nearly 100 nm.[17]

1.1.1 Metamaterials and Au::VO_2 Structures

The ability to fabricate precise subwavelength structures has led to the creation of composite structures known as EM *metamaterials* which have a wide range of optical properties, many of which cannot be found in nature. The exact definition of a metamaterial has not been established by the scientific community, however an essential characteristic is an underlying lattice of subwavelength structures within an embedding medium leads to an effective EM response of the composite structure that

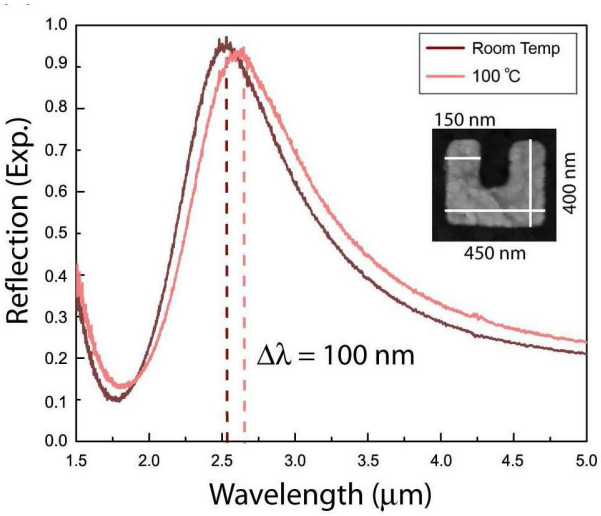

Figure 1.3: From [21], a metamaterial consisting of Ag::VO_2 SRRs.

is not found in the individual properties of the isolated constituent materials.[11] This is analogous to the optical response of single molecules and atoms determining the optical properties of the medium in which they form. In this sense, "macroscopic" refers to length scales of several wavelengths or longer. The concept of a metamaterial has been extended beyond EMs and into other fields, leading to the creation, for example, of acoustic metamaterials.[31]

Depending on the wavelength of EM radiation, the subwavelength structures may be visible to the naked eye. Figure 1.4, taken from [9], shows a metamaterial consisting of split ring resonators (SRRs) designed to cloak objects from detection at microwave frequencies. Each SRR in the image is 3 mm in width. In addition to cloaking objects, metamaterials can also be designed to have such novel properties as artificial magnetism and a negative index of refraction.[10] Within these structures,

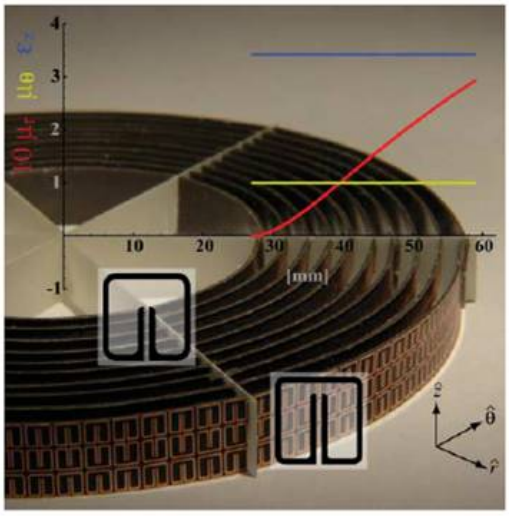

Figure 1.4: From [9], a metamaterial consisting of SRRs designed to cloak objects from detection at microwave frequencies. Each SRR is 3 mm in width.

metal NPs and more complex nanostructures, such as SRRs, are playing a critical role in emerging nanotechnologies with a range of applications.[9,21–23,32]

The Au::VO_2 structures previously mentioned are arguably all examples of metamaterials since the subwavelength structures change the response of the composite material relative to the individual constituent materials in a predicable and controllable manner. Effective dielectric functions characterizing the modified optical response can, in principle, be found using an appropriate effective medium theory.[33–37] In the case of Au::VO_2 structures, the macroscopic optical properties can be tuned by external stimuli, making this class of metamaterials of particular interest for both fundamental and applied research efforts.

1.1.2 Major Contributions

Although the precise wavelength tunability of Au::VO_2 structures has been established in the literature, a detailed analysis of the interactions of the Au plasmon with the surrounding VO_2 has been limited, especially at VS and NIR wavelengths. In addition to the ability to shift the LSPR, Au::VO_2 structures with resonances between 600 and 1200 nm provide a unique way to study the EM interactions between the Au nanostructures and the VO_2 embedding medium. This region is of special interest due to the interband transitions of VO_2 occurring in a region between 1 and 1.5 eV which coincides with the vanadium split $d_{||}$-bands that come together during the SMT to form the metallic state conduction band.[26] The lithographically prepared NP arrays studied here, with their relatively simple geometry, are ideal for studying Au::VO_2 structures at these wavelengths since precise control of the geometry allows for a more detailed analysis of the Au plasmon interaction with the surrounding VO_2 than non-ordered geometries. Understanding the interactions between the LSPR of the Au NP and the VO_2 film is essential for developing applications of Au::VO_2 structures in this part of the spectrum. Each of the three experimental chapters in this dissertation is concerned with a unique aspect of this interaction.

In Chapter III, we study the interaction of the VO_2 with single arrays of NPs by measuring the change in LSPR wavelength and width as a function of temperature. The resulting *plasmonic hysteresis* serves as a sensitive probe of the SMT, and we relate changes in the LSPR to the increasing metallic fraction of VO_2 domains and the changes to the band structure of the film. This is the first study to take advantage of

the nanoantenna aspect of Au NPs to probe the SMT. One conclusion drawn from this study is the realization that the widely used VO_2 dielectric constants as measured by Verleur and colleagues may not accurately describe the effective medium surrounding the Au NPs as fabricated for this study. We use the LSPR to estimate the difference in value between our film and that reported by Verleur in [38]. The contrast in optical extinction between low and high temperature states is relatively poor compared to what has been reported at terahertz wavelengths, and the LSPR is highly damped compared to Au NPs in air with a reduction in extinction efficiency by a factor of 3.5. Most interestingly, the interband transitions lead to a 30% reduction in NP dephasing time during the SMT for NPs coupled to the $d_{||}$-transitions.

Chapter IV describes the use of arrays of Au NP pairs (nanodimers) to study the effect of near-field interactions between particles on the sensitivity of the LSPR to the phase transition of VO_2. This chapter extends the theoretical analysis of Jain *et al.* in [39] to ellipsoids and polarization modes in the direction perpendicular to the dimer axis (i.e., the short axis). Smaller interparticle spacing leads to an increase in sensitivity to changes in the gap for light polarized along the dimer axis (long axis), but has the inverse effect for light polarized along the short axis of the dimers. This increased sensitivity to changes in local dielectric function may be used in several applications, such as increasing the signal-to-noise ratio for detectors employing Au::VO_2 structures. Although not as sensitive to changes in ND gap, the LSPR of the short-axis polarization mode retains sensitivity at larger distances than the long-axis mode. This work is the first to measure ND interactions within an absorbing medium, and present evidence that the VO_2 interband transitions reduces

the coupling strength between interactions NPs.

Although the contrast at VS and NIR wavelengths may limit future applications of Au::VO_2 structures which rely on the modulation of Au LSPR, the ability of Au NPs to absorb EM radiation and increase the temperature of the surrounding medium has been documented.[40,41] Chapter V measures the effect of the Au NPs on the VO_2 switching behavior for low-power laser irradiation. The presence of Au NPs within the VO_2 film lead to a higher sensitivity to laser irradiation, lowering the intensity necessary to switch the film by over a third for an array of 140 nm diameter NPs with grating constant of 350 nm. This may have important implications for optical switches and optical limiting applications, and is, to our knowledge, the first time Au NPs have been used to enhance the low-intensity photochromic response of VO_2. The relationship between the substrate and thin film is also considered, and an analysis of the results show that heat transport into the substrate significantly hinders switching of the film.

Finally, although detailed conclusions are presented at the end of each chapter, some generalized implications of these results are discussed in Chapter VI. The rest of this chapter provides an overview of the relevant physics concepts covered in this dissertation, beginning with a discussion on plasmonics.

1.2 Localized Surface Plasmon Resonance

There has been recently a rather extraordinary amount of experimental and theoretical work on the origin and implications of characteristic energy losses experienced by fast electrons passing through foils. This effort has received great impetus from the suggestion by Pines and Bohm that some of these energy losses are due to the excitation of plasma oscillations or "plasmons" in the sea of conduction electrons and from their work on the

theory of these oscillations. - Ritchie[42]

The fundamental, collective free-electron oscillations in metals alluded to by Ritchie in 1957 are essential to the development of nanotechnology and to the understanding of physics on the nanoscale.[42] The plasma oscillations in the volume of the metal, known as bulk plasmons, can only be excited by collisions with electrons or other charged particles at energies above the plasma energy because of conservation of momentum.[5] In contrast, the dispersion relation – and thus the momentum – for propagating surface plasmons (SPs) below the plasma energy is close enough to photons of comparable energy that they can be excited by EM radiation, resulting in a surface plasmon-polariton (SPP). As we decrease the size of the structure to the nanoscale, the skin depth of the photons become comparable to the characteristic length of the structure, and the SPP becomes the dominant optical response within the metal. In NPs, where the surface modes form standing waves, the plasmon is known as a *localized* surface plasmon-polariton.[5] Traditionally, localized surface plasmon-polaritons are referred to as localized surface plasmons (LSPs) with the coupling to photons understood. The LSPR of metal NPs is sensitive to the particle size, shape, surrounding medium, and interactions with other nanostructures or molecules,[5,39,43–51] making them ideal *nanoantennas*, sensitive to changes in their local environment. Among other applications, arrays of NPs are capable of serving as detectors for chemical and biological contaminants.[6]

The discovery of the plasmon occurred rather late in the development of modern nanoscience, which began over a century earlier with work by Faraday;[1,2] however, the

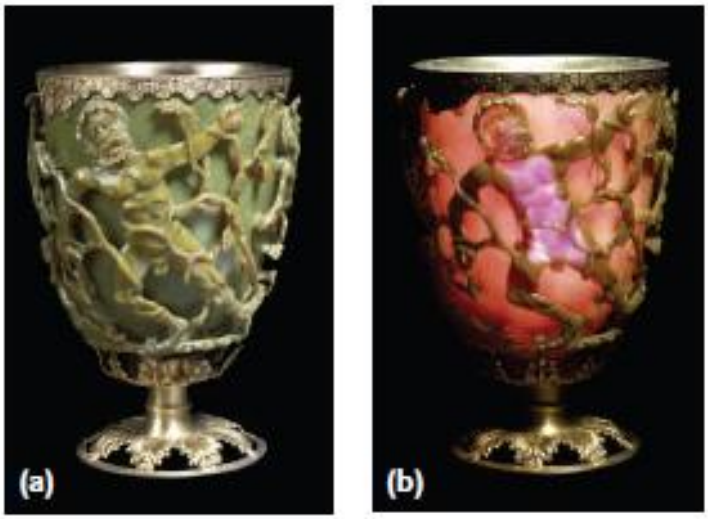

Figure 1.5: From 4$^{\text{th}}$ century Rome, the Lycurgus Cup. (a) When illuminated from the outside, the cup has a greenish-yellow color due to the presence of silver NPs, but (b) when illuminated from the interior, gold NPs produce a ruby color. A detailed analysis of the history and composition of the cup can be found in [52].

history of plasmonics actually begins long before. Although the underlying physics would not be understood for many centuries, using plasmonic nanostructures to manipulate the optical properties of a material dates back to at least 4$^{\text{th}}$ century Rome. Figure 1.5 shows the Lycurgus Cup, which exhibits artificial dichroism due to the presence of colloidal Au and Ag NPs in the glass. A detailed analysis of the history and composition of the cup can be found in [52]. The presence of Au and Ag alone in the glass is not enough to produce the dichroism; the underlying nanostructure of the metals is essential. The 13$^{\text{th}}$-century stained glass windows of the *Cathdrale Notre-Dame de Paris*, France, shown in Figure 1.6, also contain metal NPs to produce the vivid colors.

In 1857 Michael Faraday, out of fascination for the ruby color of colloidal gold,

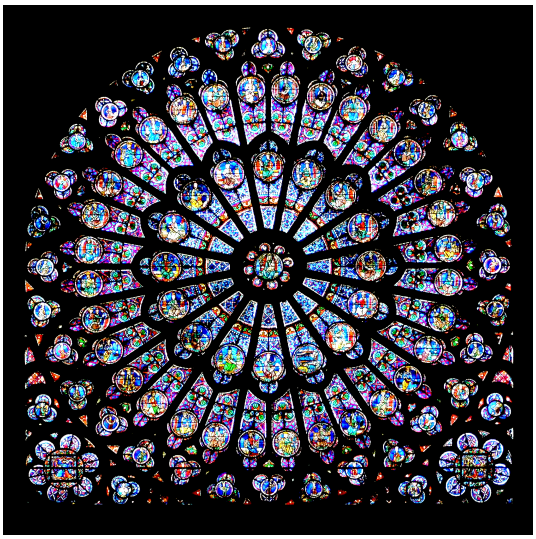

Figure 1.6: Thirteenth century stained glass from the *Cathédrale Notre-Dame de Paris*, France. Image used from `http://en.wikipedia.org/wiki/File:GothicRayonnantRose003.jpg`.

published a study on the optical properties of colloidal metals in aqueous solution. He concluded that the color was due to light interactions with particles too small to see with any available microscope of the day.[1,2] A century later, using the same methods of producing the chemical solutions, electron microscope studies revealed the diameter of the metal NPs to be 6 ± 2 nm.[2] Increased efforts to determine the origin of the dichroic properties of the Lycurgus Cup took place during the 1950s. In 1959, B. S. Cooper at General Electric Company hypothesized that colloidal Au and Ag particles, comprising less than 1% of the glass, were responsible for the unique dichroism of the ancient cup. Transmission electron microscopy conducted in the 1980s confirmed the presence of NPs ranging from 50 to 100 nm in size composed of a Ag:Au alloy (ratio 7:3).[52] In each of these cases, the very presence of Au, Ag, or other

metals is not enough to explain the optical properties described. The shape and size of the metal colloids played an essential role in determining the optical interaction of the metals with light.

In 1908, Gustav Mie developed an exact solution to absorption and scattering by a sphere of arbitrary radius in a medium of arbitrary index of refraction.[53] Mie was not the first to work out a theory describing the interaction of light with small, spherical particles. Ludvig Lorenz and several other scientists developed preliminary theories and were referenced in Mie's 1908 paper.[44,53] Mie worked out the exact solution for spherical particles and correctly predicted multiple resonant modes (Mie resonances) not accounted for in Rayleigh's theory of scattering from small particles.[3,4,44,53] He then applied his theory to understanding Au colloids in aqueous solution. It is now understood that in metal NPs, the surface modes predicted by Mie theory are the localized surface plasmons. In his paper, Mie acknowledged that spherical particles were not sufficient to account for the known polarization dependence of certain scattering experiments.[53] He concludes his paper stating, "To complete the theory it is absolutely necessary to study the behavior of ellipsoidal particles."[53] Although an exact solution has not been found, in the following section we will discuss the optical properties of metal ellipsoids smaller than the wavelength of light using the quasistatic electric dipole approximation.

1.2.1 Quasistatic Electric Dipole Approximation

Unfortunately, lithographically prepared particles are not spherical; they more closely resemble disks. Their shape can be closely approximated as ellipsoids (e.g.,

[54]). However, this forces us to employ approximations to Mie theory in order to develop an analytical model. We will mostly follow the derivation of Bohren and Huffman.[44]

Interactions between particles small compared to the wavelength of incident light and EM radiation can be treated as quasistatic, and their interaction with the electric field can be approximated as an ideal dipole oscillating at the center of the particle. Implicit here is the assumption that self-radiation damping can be ignored; that is, the electrons oscillating on one side of the particle are in phase with those on the other side. For linearly polarized incident light, an ideal dipole located at the origin of a medium with dielectric function ϵ_{m} has a dipole moment of magnitude $p = \epsilon_{\mathrm{m}}\alpha(\omega)E_0$, where $\alpha(\omega)$ is the frequency-dependent particle polarizability, E_0 is the electric field incident on the dipole, and Gaussian units are being used.

In an absorbing medium, the wave number k is complex and must be correctly accounted for when deriving the absorption and scattering cross sections, C_{a} and C_{s} respectively.[44,55] They are given by

$$C_{\mathrm{a}} = \mathrm{Re}\,[k]\,\mathrm{Im}\,[\alpha] \tag{1.1}$$

and

$$C_{\mathrm{s}} = \frac{|k|^4}{6\pi}\,|\alpha|^2\,. \tag{1.2}$$

The extinction cross section C_{e} is the sum of (1.1) and (1.2). We can also define extinction, absorption, and scattering efficiencies Q_{e}, Q_{a}, and Q_{s} by dividing C_{e}, C_{a},

and C_s by the physical cross-sectional area of the particle A (in our case, $A = \pi R^2$). A more extensive discussion of extinction measurements in an absorbing medium are presented in Chapter II.

Using this formalism, predicting extinction cross-sections and LSPR requires calculating α for a given particle. For a sphere of radius R in the quasistatic limit,

$$\alpha = 4\pi R^3 \frac{\epsilon - \epsilon_m}{\epsilon + 2\epsilon_m}, \tag{1.3}$$

where $\epsilon = \epsilon' + i\epsilon''$ is the bulk dielectric function of the material that makes up the particle (Au). So far, this theory applies to both metallic and dielectric particles. For complex numbers, we use the convention that single primes (') denote the real part and double primes (") the imaginary part of the number. The LSPR approximately occurs when the real part of the denominator of (1.3) vanishes. That is, when $\epsilon'(\omega) = -2\epsilon'_m$, where ϵ'_m is positive for dielectric materials. Therefore, ϵ' must be negative in order to satisfy the resonance condition. For metal NPs, this resonant dipole mode is the dominant LSP excitation, and is generally what is meant by the LSPR. Higher order modes exist, and in the case of a sphere, are derivable from Mie theory. The amplitude of the LSPR depends on how freely the electrons in the plasma can oscillate. For a particle embedded in a non-absorbing medium, the imaginary part of the dielectric functions ϵ'' and ϵ''_m work to damp the LSPR by accounting for losses of energy to electron scattering, interband transitions, and the excitation of phonons.

For an ellipsoid, an analogous derivation to (1.3), which is detailed in Bohren and Huffman and summarized in Maier,[5,44] gives a polarizability along the i^{th} ellipsoidal

axis corresponding to the polarization of the incident light as

$$\alpha_i = V \frac{\epsilon - \epsilon_{\mathrm{m}}}{\epsilon_{\mathrm{m}} + L_i \left(\epsilon - \epsilon_{\mathrm{m}}\right)}, \tag{1.4}$$

where $V = \frac{4}{3}\pi R_1 R_2 R_3$ is the volume of the ellipsoid with the length of the i^{th} axis R_i. The geometrical factor L_i for the ellipsoid is given by

$$L_i = \frac{R_1 R_2 R_3}{2} \int_0^\infty \frac{dq}{\left(R_i^2 + q\right) \sqrt{\left(q + R_1^2\right)\left(q + R_2^2\right)\left(q + R_3^2\right)}}. \tag{1.5}$$

The L_i's are constrained by the property $L_1 + L_2 + L_3 = 1$. In the case of maximum symmetry, a sphere, $L_1 = L_2 = L_3 = 1/3$, and (1.4) reduces to (1.3).

Without loss of generality, we can assume that $R_1 \geq R_2 \geq R_3$, which implies that $L_1 \leq L_2 \leq L_3$. The resonance condition implied by (1.4) is

$$\epsilon'\left(\omega\right) = \left(1 - \frac{1}{L}\right) \epsilon'_{\mathrm{m}} = \kappa \epsilon'_{\mathrm{m}}, \tag{1.6}$$

$$\kappa \equiv 1 - \frac{1}{L}, \tag{1.7}$$

where we have dropped the subscript from the geometrical factor since we are always referring to the axis coinciding with the polarization state of the incident field. Equation (1.6) is only an approximation for the position of the LSPR because in real materials ϵ and ϵ_{m} are complex functions. The imaginary parts can shift the LSPR slightly but primarily damp the oscillation and result in a broader resonance with decreased amplitude.[44]

If $L = 1/3$, then (1.6) reduces to the resonance condition for a sphere, where $\kappa = -2$. Breaking the symmetry of a sphere by increasing R_1 and holding R_2 and R_3 constant, causes a decrease in L_1 and thus increasing L_2 and L_3. For frequencies below the plasma frequency and the onset of interband transitions, ϵ' for Au is a monotonically decreasing function less than zero. Therefore, from (1.6), increasing R_1 redshifts the LSPR mode corresponding to the polarization axis of the incident field, but blueshifts the LSPR mode corresponding to the other two axes. This polarization dependence of the LSRP in non-spherical particles is well-documented in the literature and can be found in most textbooks.[5,43,44] The factor κ will be an essential tool for understanding the results in Chapters III and IV.

Nanodisks can be modeled as oblate spheroids, where $R_1 = R_2 > R_3$. Equation (1.5), for polarization along either of the longer axes, then takes the form

$$L_1 = L_2 = \frac{1}{2e^2}\sqrt{\frac{1-e^2}{e^2}}\left[\frac{\pi}{2} - \tan^{-1}\left(\sqrt{\frac{1-e^2}{e^2}}\right)\right] - \frac{1-e^2}{2e^2}, \tag{1.8}$$

where e is the eccentricity given by

$$e^2 = 1 - \left(\frac{R_3}{R_1}\right)^2. \tag{1.9}$$

Inspection of (1.4) through (1.9) shows that, within the limits of this approximation, the ratio of axis lengths determines the position of the LSPR and not the absolute lengths of the axes. In general, this is not the case. For particles with dimensions comparable to or smaller than the mean free path of the electrons, ap-

proximately 20 nm, the LSPR is damped due to scattering at the surface.[43,56] In this range, the bulk dielectric functions ϵ and ϵ_{m} are not adequate for modeling the physics of the LSPR. The chemistry at the interface between the particle and surrounding medium must also be accounted for in determining the width of the LSPR, an effect known as chemical interface damping.[57] This leads to additional broadening of the LSPR and can be modeled by adding a term to the homogeneous linewidth Γ so that the total homogeneous linewidth becomes

$$\Gamma \approx \Gamma_0 + \frac{2\omega_p^2}{\omega^3}\left[\left(\frac{d\epsilon'}{d\omega}\right)^2 + \left(\frac{d\epsilon''}{d\omega}\right)^2\right]^{-1/2} \frac{A v_{\mathrm{Fermi}}}{R}, \tag{1.10}$$

where Γ_0 is the linewidth predicted by Mie theory or the quasistatic approximation, v_{Fermi} is the Fermi velocity and A is a fit parameter that describes the interface. For particles below approximately 10 nm, quantum effects must be taken into account since the electron wavefunction can extend beyond the particle surface.[43,58] For the geometries of interest in this dissertation, quantum size effects and interface damping are negligible.

For particles with characteristic lengths of approximately 100 nm or more, the quasistatic approximation begins to break down, and radiation damping decreases the dipole moment, broadens the LSPR, and shifts the resonance.[5,44,56,59] By adding terms to Equation (1.4), the formalism can be extended to take into account size effects or interactions between particles. Kuwata *et al.* uses dark-field spectroscopy and finite-difference time-domain (FDTD) modeling to take into account size effects

in ellipsoidal particles. The polarizability they derived is given by

$$\alpha \approx \frac{V}{\left(L + \frac{\epsilon_{\mathrm{m}}}{\epsilon - \epsilon_{\mathrm{m}}}\right) A\epsilon_m x^2 + B\epsilon^2 x^4 - i\frac{4\pi^2\epsilon_{\mathrm{m}}^{3/2}}{3}\frac{V}{\lambda_0^3}}, \tag{1.11}$$

$$A(L) = -0.4865L - 1.046L^2 + 0.8481L^3, \tag{1.12}$$

$$B(L) = 0.01909L + 0.1999L^2 + 0.6077L^3, \tag{1.13}$$

where $x = \pi R_i/\lambda_0$, λ_0 is the free-space wavelength.[59] The terms with coefficients A and B are higher order terms that depend on the shape of the particle. The last term in the denominator is a correction that takes into account radiation damping. For particles slightly larger than the quasistatic limit, a radiation reaction field is produced that reduces the dipole moment of the particle by radiating power. The reaction field is, therefore, 90° out of phase with the dipole, and given by $\vec{E}_r = i2k^3\vec{P}/3$. The electric field is then decreased by this amount, and thus the polarizability is reduced proportional to the volume of the particle, as seen in the the third term in (1.11).[56,59] Interactions within a NP array can also be accounted by defining an effective geometrical factor, equivalent to what is done in [39, 56]. This approach is used in Chapter IV to understand the coupling between two NPs forming a nanodimer (ND).

1.3 Dielectric Functions

We now detour slightly from our discussion on the LSPR to discuss perhaps the most important parameters of (1.4): the dielectric functions ϵ and ϵ_{m}. The behavior

of these functions in different frequency regimes can be found in many textbooks and will not be repeated here (see, e.g., [5, 43, 44, 60, 61]). However, the features of the LSPR directly depend on the properties of these two functions. Therefore it is important to understand the physical significance of the dielectric function. The following section discusses the Lorentz-Drude model for the dielectric function and its relevance to understanding the optical properties of noble metals, in particular Au. The quasistatic approximation will then be used to understand how changing the real and imaginary parts of ϵ and ϵ_{m} affects the LSPR. Section 1.4.2 discusses the dielectric function of VO_2.

1.3.1 Lorentz-Drude Model

Charges in a material subjected to an applied external electric field experience a polarizing force. In isotropic materials and to first-order in E, the resulting average dipole moment per volume $\vec{P}$ can be expressed as $\vec{P} = \epsilon\vec{E}$, where ϵ determines the linear response of the material to the field. For an incident harmonic EM field, ϵ typically depends on the frequency $f = 2\pi\omega$ of the radiation.

Following reference [5], consider a system of free electrons within a solid material in which the scattering of the free charges off of other electrons and nuclei occurs at a collision rate of γ. Without loss of generality, we define a coordinate system such that the polarization of the driving field is along the x-axis. The equation of motion for the electron is $m\ddot{x} + m\gamma\dot{x} = -eE(t)$. Solving for x and calculating the polarization of the material $P = -nex$ allows one to deduce the dielectric function of the system

to be

$$\epsilon_{\mathrm{D}} = 1 - \frac{\omega_{\mathrm{p}}^2}{\omega^2 - i\gamma\omega}, \tag{1.14}$$

where $\omega_{\mathrm{p}}^2 = ne^2/\epsilon_0 m$ is the plasma frequency, n is the number density of the electrons, and m is the effective electron mass, which accounts for coupling to the ion cores.[43] This is known as the Drude model and describes the free-electron response of metals at frequencies below the onset of interband transitions.[44,61–63]

According to (1.14), for $\omega \gg \omega_{\mathrm{p}}$, ϵ_{D} approaches 1. However, for the noble metals, an extension of this model is needed due to residual polarization. That is, as $\omega \to \infty$, $\epsilon_{\mathrm{D}'} \to \epsilon_\infty$, where the D' is used to denote a modification from the Drude model and ϵ_∞ is a constant. Furthermore, the effects of bound electrons and interband transitions, in which electrons are excited to energy states higher than the Fermi level, also lead to a divergence from the Drude model. We can account for these by adding terms with resonance frequencies ω_j and damping frequency γ_j to the equation of motion: $m\ddot{x} + m\gamma_j\dot{x} + \omega_j^2 x = -eE(t)$. We account for all possible transitions in the solution as a sum of N oscillators, each with a strength A_j. The resulting Lorentz-Drude (LD) model of the dielectric function is given by

$$\epsilon_{\mathrm{LD}} = \epsilon_\infty - \frac{\omega_{\mathrm{p}}^2}{\omega^2 - i\gamma_{\mathrm{D}}\omega} + \sum_{j=1}^{N} \frac{\omega_{\mathrm{p}} A_j}{\omega_j^2 - \omega - i\gamma_j\omega}. \tag{1.15}$$

The LD model is sufficient to describe the features of the dielectric functions of Au and VO_2 between 600 and 1200 nm.[38,64,65]

Table 1.1: Properties of Select Metals. The data have been taken from [44] unless otherwise noted. Surface plasmon energies are for spherical particles in air; ϵ'' is the value of the imaginary part of the dielectric function where $\epsilon' = -2$, corresponding to the position of this LSPR. Except for ϵ'', all values are in units of electron-volts; ϵ'' is unitless.

Material	Bulk Plasmon	Surface Plasmon	ϵ''	Interband Threshold [43]
Cu	8.2 [65]	3.5	4.9	2.1
Ag	3.8	3.5	0.28	3.87
Au	7.9 [65]	2.5	5.0	2.42
Na	5.4	3.3	0.12	2
Al	15.1	8.8	0.2	1.5

1.3.2 Dielectric Function of Gold and Other Metals

At energies much smaller than the threshold of interband transitions, metals behave according to the Drude model. The threshold for interband transitions, however, can occur at VS or NIR energies, and losses due to interband transitions directly impact the plasmonic properties of the metal. Table 1.1 shows the bulk plasmon energy ω_{p}, the surface plasmon energy, ϵ'' where $\epsilon' = -2$ (the condition for LSPR of a sphere in air), and the threshold energy of the interband transitions for selected metals taken from [44], [43], and [65]. Free-electron metals are those with minimum losses from the interband transitions, such as the alkalis and aluminum, and all exhibit LSPR behavior in the ultraviolet and visible. However, the alkalis are highly reactive, and, therefore, difficult to study and not desirable for many applications.

The noble metals — Cu, Ag, Au — by contrast, are very stable, although self-limiting surface oxidation (tarnishing) can be a factor, especially in Ag.[43,66] These metals have full *d*-shells close to the Fermi level, with a single *s*-electron in the con-

duction band.[5,43] The effect of interband transitions and ion-core polarization is to redshift the plasma frequencies with respect to the free electron model. In free electron metals, the effect is negligible; however, in the noble metals the influence of interband transitions have to be taken into account as they effectively shift surface plasmon resonances from the UV to the visible and near-infrared. The resulting LSPR is more correctly described as a hybrid mode between free-electron oscillations and interband excitations than as a pure free-electron resonance.[43] For Au, the interband transitions begin at 2.42 eV ($\lambda = 512$ nm) and their contribution increases at higher energies. Figure 1.7 shows the real and imaginary parts of the dielectric function for Au measured by Johnson and Christy by reflection and transmission measurements on films with thicknesses between 18.5 and 50 nm.[64] The thickness of the film is important, as the dielectric function can vary with thin film thickness;[67] morphology difference associated with film growth are known to lead to variations in experimental measurements of the dielectric function.[64,65,68] The Johnson and Christy (JC) data are among the most commonly used by plamonic researchers for theoretical calculations in plasmonics.[68,69]

The LSPR of the noble metals in the optical and NIR makes them desirable for applications requiring absorption at those wavelengths. However, the resonances are also significantly damped by interband losses. With the exception of Ag, with $\epsilon'' = 0.28$ at the LSPR wavelength for spheres in air, both Au and Cu have $\epsilon'' \approx 5$ at their respective resonance wavelengths. This is reflected in optical spectra by a weak, broad resonance. For example, Au spheres in air have a smaller extinction resonance compared to Ag spheres by roughly a factor of 10. Copper has no appreciable resonant

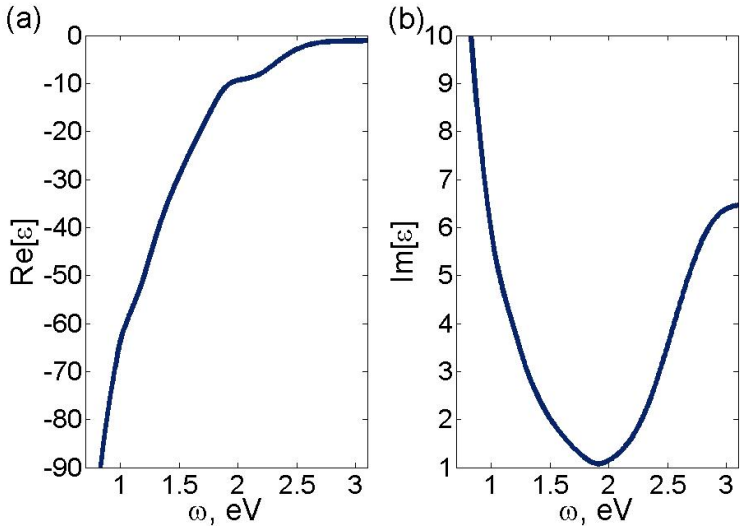

Figure 1.7: (a) Real and (b) imaginary parts of the dielectric function of Au from Johnson and Christy.[64]

extinction for small spherical particles ($2R = 10$ nm) in air. However, upon redshifting the LSPR by changing the particle shape or embedding medium, the plasmonic absorption of Cu and Au can become comparable to that of Ag in the same medium; Reference [43] provides many figures of experimental and modeled data demonstrating the effect. Figure 1.8 shows absorption efficiencies Q_{a} of $R = 25$ nm Au particles with varying ϵ_{m} calculated from (1.3) using MATLAB®. The highest energy that Au can support a LSPR mode occurs at $\epsilon_{\mathrm{m}} = 1$, but the resonance is highly damped. As ϵ_{m} increases, the resonance is redshifted to a region of the spectrum with lower losses, narrowing the resonance and increasing the efficiency. As ϵ_{m} continues to increase and redshift the LSPR, free-electron damping leads to higher losses, and the LSPR again broadens and decreases in amplitude. Free-electron damping is responsible for the increase in ϵ'' at lower energies (Figure 1.7). Although $\epsilon_{\mathrm{m}} = 30$ is over a factor

of three larger than VO_2 at the wavelength in which we are interested, the effect of moving from a spherical particle to an ellipsoid can shift the resonance just as drastically. For example, disk-shaped particles with $2R = 180$ nm and height 20 nm on an indium-tin-oxide (ITO) coated glass substrate have resonances near 800 nm with extinction efficiencies of 8. These same particles have resonances close to 1000 nm and extinction efficiencies close to 2 when coated with VO_2 in the semiconducting state.

1.4 Vanadium Dioxide

Transition metal oxides have a wide range of interesting electrical, magnetic, and optical properties due the outer d-electrons of their metal ions. These electrons cannot be characterized with purely a localized or collective description, but have an intermediate character that manifests itself as one or the other or both depending on the oxide.[25] This can lead to systems, such as VO_2, that exhibit strong electron correlation and solid-solid phase transitions.[25,70] Applied research with VO_2 tends to exploit its strong infrared absorption properties of the metallic state in devices such as bolometers, and optical limiters.[71–75] At visible wavelengths, the contrast in optical absorption due to the SMT is small relative to infrared and microwave wavelengths.[71–75] In this section, we will present a brief summary of the physics and research surrounding the VO_2 phase transition followed by a discussion of the dielectric functions of VO_2 in each state.

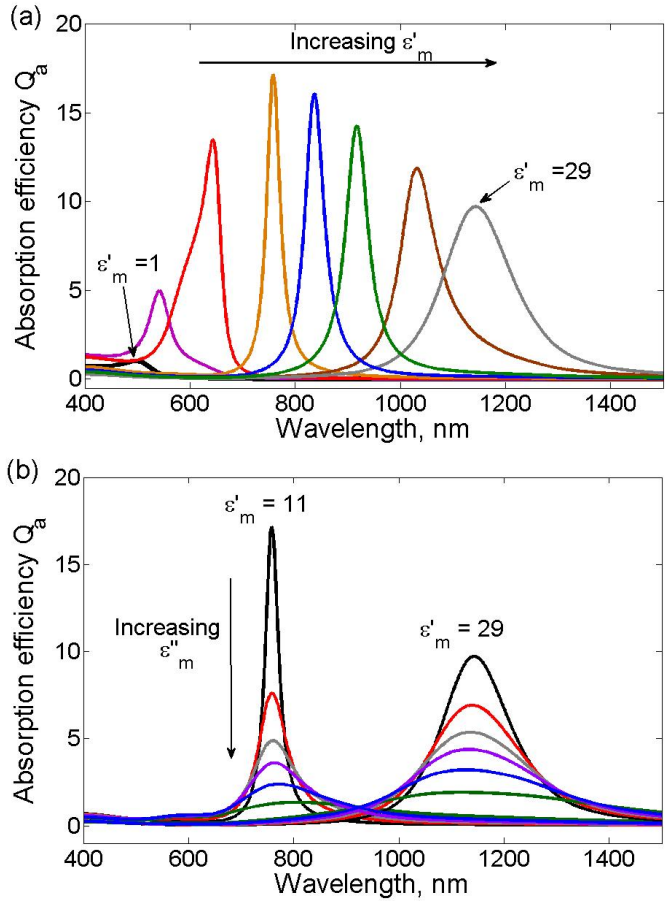

Figure 1.8: Calculated absorption efficiencies $Q_{\rm a}$ for spherical Au particles with $R = 25$ nm. (a) For a non-absorbing medium, as the real part of dielectric function of the embedding medium $\epsilon'_{\rm m}$ increases from 1 (black curve) to 29 (grey), the resonance increases and sharpens. The values of $\epsilon'_{\rm m}$ shown are, from left to right: 1, 3, 5, 11, 15, 19, 25, and 29. (b) For a constant $\epsilon'_{\rm m} = 11$ and $\epsilon'_{\rm m} = 29$, increasing the imaginary part of the dielectric function $\epsilon''_{\rm m}$ from 0 (black) to 10 (green) has little effect of on the position of the resonance, but greatly damps it, leading to a much smaller extinction efficiency and broader peak. The values of $\epsilon''_{\rm m}$ shown are, from tallest curve to shortest: 0, 1, 2, 3, 5, and 10.

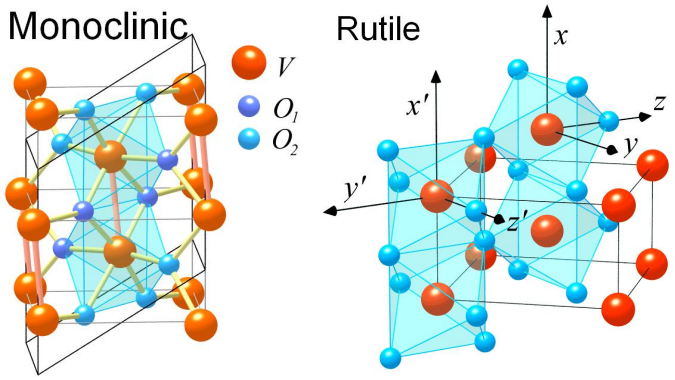

Figure 1.9: The crystal structure of VO_2 in the monoclinic, low-temperature semiconducting and tetragonal (rutile), high-temperature metallic states from [26].

1.4.1 Semiconductor-Metal Phase Transition

Since the discovery of the phase transition by Morin in 1959, understanding the mechanism of the SMT in VO_2 has been a challenge for many researchers.[26,76–83,83–86,86–89] As the electronic and crystal structure of the material undergoes the phase transition, there is an abrupt change in the dielectric function of the VO_2 at the transition temperature.[38] When induced optically, it has been shown that the SMT occurs on femtosecond time scales,[81,87,88,90–94] making it potentially desirable for many applications ranging from optical switches (e.g., [22]) to optical limiters for protecting sensors (e.g. [72, 73, 75]).

The crystal structure of VO_2 transitions from a semiconducting, monoclinic unit cell to a metallic, tetragonal (rutile) cell, as seen in Figure 1.9. The monoclinic phase is denoted M_1 since there are two other semiconducting states that can be manifested under certain conditions, such as chemical doping or application of pressure, and are characterized by another monoclinic structure (M_2) or a triclinic structure (T).[26]

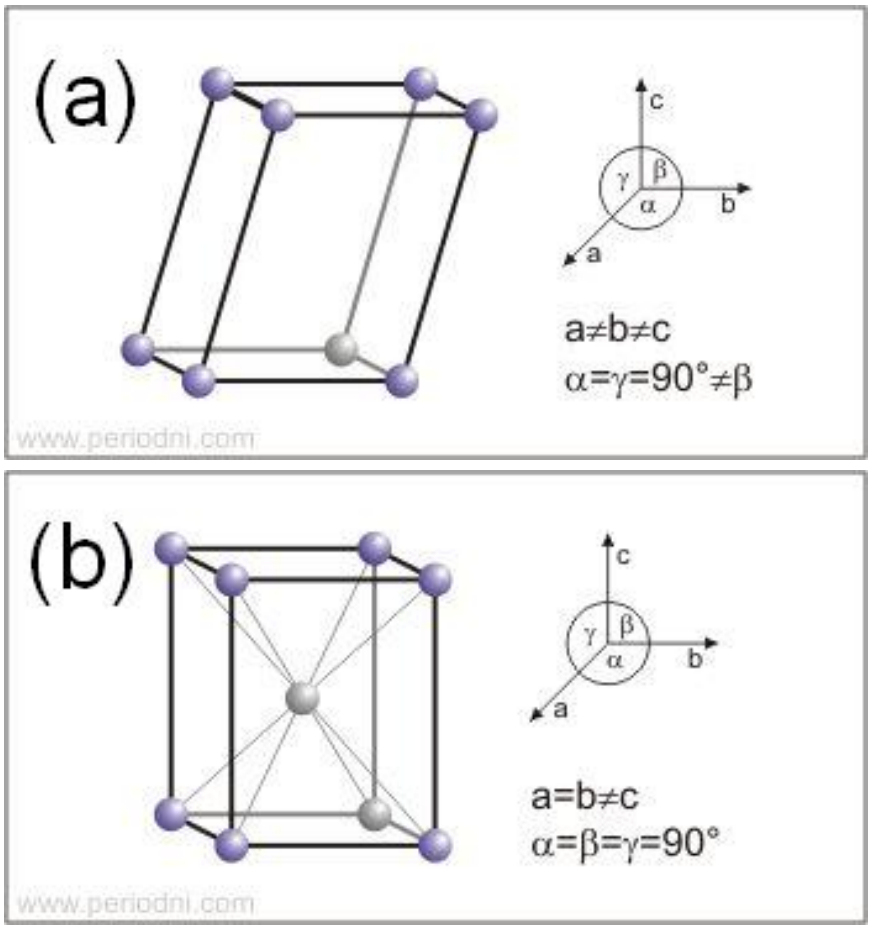

Figure 1.10: The definition of lattice constants a, b, c for (a) monoclinic and (b) tetragonal crystal structures. The schematics are from `http://www.periodni.com/`.

Neither of these states are manifested under the experimental conditions described in this work.

The lattice constants for the M_1 phase, as defined in the schematics of Figure 1.10a, are $a = 5.75$ Å, $b = 4.54$ Å, $c = 5.38$ Å with a monoclinic angle $\alpha = 122.6°$. The unit cell in the semiconducting state is roughly twice the length along the c-axis compared with the metallic state due to dimerization and tilting of adjacent V^{4+} atoms. In the metallic state, the tetragonal lattice constants, defined in Figure 1.10b, are $a = 4.55$ Å,

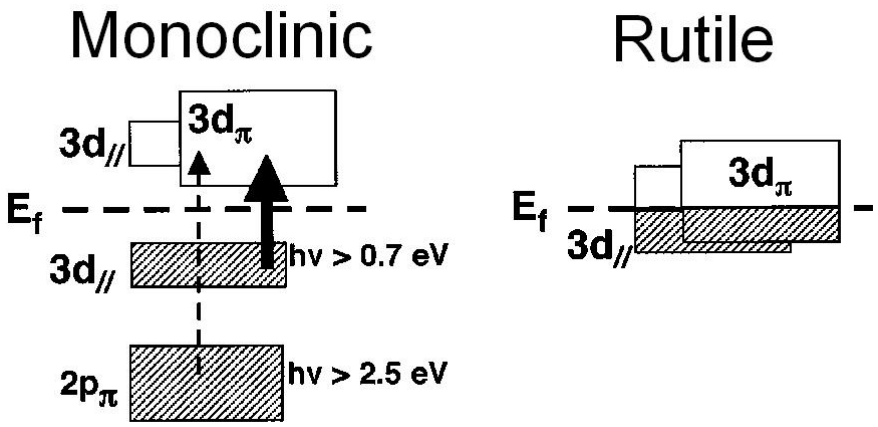

Figure 1.11: From [81], the band structure of VO_2 in the monoclinic, semiconducting state and tetragonal, metallic state.

$c = 2.85$ Å.[25,26,38] The band structure of VO_2 in each state is shown in Figure 1.11, from [81]. As the material makes the transition from semiconducting to metallic, the $3d_\pi$ band lowers, and the split $3d_{||}$ bands come together to form the conduction band of metallic VO_2. Although well studied over the past several decades, the mechanism behind the phase change in VO_2 is still a point of contention since it exhibits (and contradicts) aspects of both Peierls and Mott transitions.[81,82,92,93,95–97]

The Peierls mechanism results from lattice instability in a one-dimensional metal, such as rutile VO_2. According to this theory, the partially filled $3d_{||}$-band of the V^{4+} ions, each containing a single electron, leads to a lattice instability since adjacent electrons can pair up into a lower energy state. This results in dimerization of the V^{4+} ions within the crystal, and localization of the charge. In this scheme, the mobility of the carriers is reduced, and the material is as an insulator or semiconductor due strictly to the crystal structure. The change in the VO_2 crystal structure and the-

oretical calculations of the band structure support this mechanism.[26,60,77] Ultrafast measurements by Cavalleri *et al.* also support the view that the SMT is caused by a Peierls-like mechanism, with the dimerization resulting from the electrons forming spin-singlets.[81,92]

The Mott-Hubbard mechanism, proposed by Zylbersztejn and Mott in 1975, is associated with the strong correlation of the electrons.[78] In this scheme, the bandgap in the semiconducting state is due to the on-site Coulomb repulsion described by the Hubbard potential U. As the temperature increases, the hopping amplitude t also increases until U/t is below a critical value, allowing conduction to occur in the material. Reduction of U/t can also be achieved by increasing the carrier concentration above a critical value.[70] In VO_2, this critical value is on the order $10^{18} - 10^{19}/\text{cm}^3$.[15] Studies by Qazilbash *et al.*, have shown that an electronic transition occurs before the structural change, providing strong evidence that the SMT is driven by a Mott-Hubbard transition.[82]

A study on Au::VO_2 nanostructures consisting of a Au island-film (Figure 1.12) and VO_2 by Xu *et al.* reported that small nanojunctions of Au NPs and nanoparticulate VO_2 exhibit a reduced transition temperature T_c by as much as 30°C. They propose that the mechanism for this is electron injection into the VO_2 due to the higher Fermi level of Au relative to VO_2 (Figure 1.13, from [15]). The increased carrier density lowers the ratio U/t, thus lowering T_c, and supporting the Mott-Hubbard model.[15] However, as of the writing of this dissertation, work at Vanderbilt University has not been successful in reproducing these results.

On the other hand, several studies provide evidence that the SMT is a combination

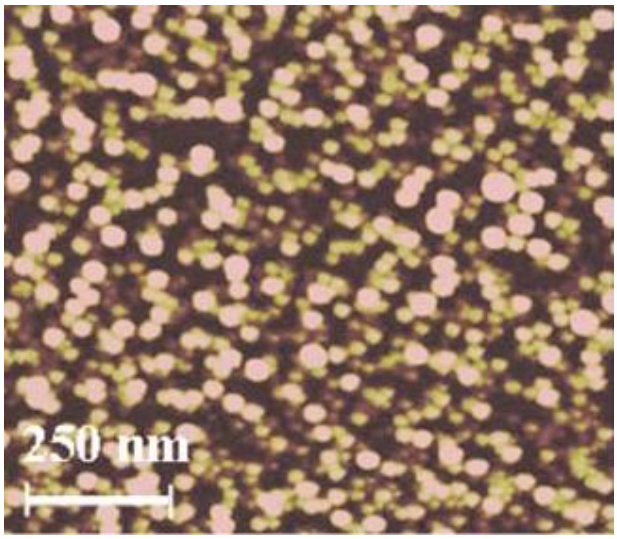

Figure 1.12: From [15], Au::VO_2 structure consisting of 2 nm Au island film and 25 nm VO_2 island film on c-cut sapphire which exhibited a lowering of T_c attributed to electron-injection from the AU to the VO_2.

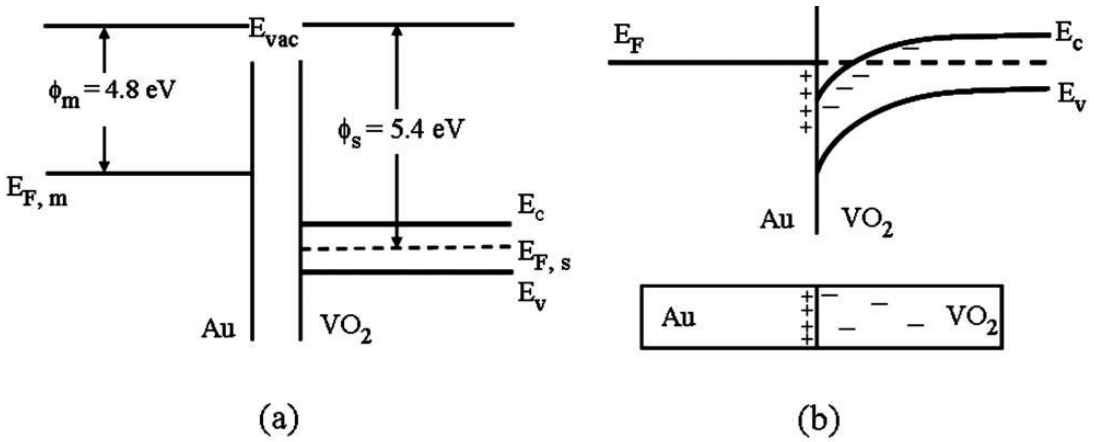

Figure 1.13: From [15], a the higher Fermi energy for (a) bulk Au relative to bulk VO_2 results in electron injection from the Au to VO_2 across nanojunctures until (b) the Fermi levels are equal. The end result is a lower T_c for the VO_2.

of Mott-Hubbard and Peierls mechanisms.[93,97,98] From band calculations, Biermann and Tomczak concluded that the strong, non-local correlation among electrons is responsible for opening the bandgap by reducing Coulomb repulsion within the $3d_{||}$ band and assisting the structural (Peierls-like) transition. Therefore, the strong correlations specifically lead to the Peierls-like transition, and the mechanism cannot be attributed to either Mott or Peierls mechanisms alone.[96] Haverkort *et al.* reached a similar conclusion through X-ray absorption studies on VO_2.[97]

Fortunately, the exact mechanism of the phase transition is not as important for the present work as understanding the changes to the dielectric function of VO_2 brought on by the phase change. In particular, it is important to note that percolation theory, which describes the changes in resistivity as individual VO_2 grains switch during the SMT, is not needed to model the transition when measured optically.[99] Resistivity changes must account for conduction pathways that form as the VO_2 domains switch to metallic, causing sudden drops in resistivity.[100] Instead, what matters for optical measurements is the effective dielectric function, which averages over the VO_2 domains and leads to a smooth transition from the semiconducting state to the metallic. At a given temperature T, the fraction of VO_2 domains in the metallic state f is given by the Boltzmann function

$$f(T) = 1 - \frac{1}{1 + \exp\left[(T - T_{\mathrm{c}})/T_{\mathrm{w}}\right]}, \tag{1.16}$$

where T_{c} is the switching temperature for either the heating ($T_{\mathrm{c}} = 72°\mathrm{C}$) or cooling ($T_{\mathrm{c}} = 64°\mathrm{C}$) and T_{w} is the width of the transition, typically less than 3°C. The

critical temperature the SMT is defined as the average of T_c or 68°C. The width of the hysteresis is defined as the difference in T_c for the heating and cooling curves, or 8°C for the 60 nm films used in this study. Figure 2.7 shows a typical VO_2 hysteresis; the measurement is described in Section 2.2.2.

Two different effective medium models are often used for VO_2 studies.[88] The Maxwell-Garnett (MG) effective medium assumes spherical, sparsely-spaced, metallic inclusions in a matrix. The resulting effective dielectric ϵ_{MG} is given by

$$\epsilon_{\mathrm{MG}} = \epsilon_{\mathrm{semi}} \frac{\epsilon_{\mathrm{met}}(1+2f) - \epsilon_{\mathrm{semi}}(2f-2)}{\epsilon_{\mathrm{semi}}(2+f) + \epsilon_{\mathrm{met}}(1-f)}, \tag{1.17}$$

where ϵ_{semi} and ϵ_{met} are the dielectric functions for VO_2 in the semiconducting and metallic states, respectively, and $f(T)$ is given by (1.16). On the other hand, the Bruggeman (BR) effective medium does not assume that the metallic inclusions are sparsely spaced. This model is known to more accurately describe the percolation in films of VO_2 where conduction pathways are important.[88,99] The BR effective dielectric function $\epsilon_{\mathrm{BR}}$is given by

$$\epsilon_{\mathrm{BR}} = \frac{1}{4}\left\{\epsilon_{\mathrm{semi}}(2-3f) + \epsilon_{\mathrm{met}}(3f-1) + \sqrt{\left[\epsilon_{\mathrm{semi}}(2-3f) + \epsilon_{\mathrm{met}}(3f-1)\right]^2 + 8\epsilon_{\mathrm{semi}}\epsilon_{\mathrm{met}}}\right\}. \tag{1.18}$$

The appropriate model depends on the experimental conditions. For example, when modeling low-T behavior, the MG model is often successful. However, due to the percolation effects during the transition, the BR often produces better results. In Chapter III, we will show that a simpler effective medium model given by an arith-

metic average over the semiconducting and metallic VO_2 domains surrounding Au NPs better describes our results than either BR or MG.

1.4.2 Dielectric Function of VO_2

Due to the sensitivity of the LSPR to the local dielectric function of the embedding medium, we need to understand the dielectric function of VO_2 and the changes that it undergoes as a result of the phase transition. Figure 1.14 shows the dielectric functions for VO_2 in both semiconducting and metallic states as determined by transmission and reflection measurements conducted by Verleur on a 100 nm film grown on sapphire by reactive sputtering.[38] For comparison, the dielectric function for Au from [64] is also shown. In the metallic state, the imaginary parts of the dielectric functions for VO_2 and Au are similar in structure in the region between 0.7 and 3 eV (413 to 1800 nm). At energies below 2 eV, free-electron dispersion and damping leads to an increase in ϵ_m'' in both Au and VO_2.

In their paper, Verleur *et al.* compared the dielectric functions for bulk VO_2 to the film and modeled the functions as Lorentz oscillators, (1.15), fitting the data with a sum of up to seven unique terms. In addition to a polarization-dependent anisotropy in the bulk samples, Verleur *et al.* found poor agreement between the thin-film and bulk measurements. Although the structural features and resonance energies were similar, the amplitudes of the oscillators varied greatly. This variation was attributed to surface defects.[38] Similarly, other studies of VO_2 thin-film dielectric functions reported similar structure as found in the Verleur work, but did not necessarily agree in the details.[101–103] In [101], for example, Kakiuchida *et al.* measured the temperature-

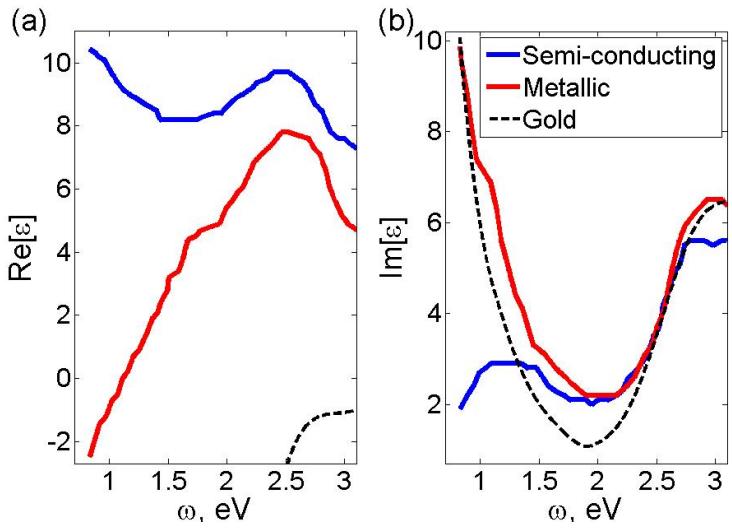

Figure 1.14: The (a) real and (b) imaginary parts of the dielectric function for VO_2 as reported in [38]. For comparison, the dielectric function for Au is also shown.[64]

dependent dielectric function of VO_2 on sputtered films by ellipsometry and modeled the results using a three-oscillator model, with the oscillator parameters similar to those of the Verleur fit. The data shown in Figure 1.14 should be taken as a guide to the structure of dielectric function, as the values tend to vary depending on the thickness of the VO_2 film and its growth method.[38,101,103] Indeed, our attempts at modeling with the Verleur data have produced LSPR modes greatly redshifted and highly damped compared to experiments. This will be discussed further in Chapter III.

The structure of the dielectric function for VO_2 can be attributed to physical excitations within the material, and the three-oscillator model of Kakiuchida *et al.* provides a good starting point.[101] Figure 1.15 shows the temperature dependent hysteresis of the Kakiuchida oscillators. The third oscillator in their model is essentially

zero in the semiconducting state and remains nearly zero in the metallic state. The resonance structure of oscillator 1, centered at 3.5 eV and clearly seen in Figure 1.14b, is due to the interband transitions from the filled oxygen O $2p$ band to the empty V $3d$ bands starting at 2.5 eV (Figure 1.11). During the phase transition, the V $3d$ band drops below the Fermi level, and hence lowers the oscillator energy. The resonance structure located around 1.4 eV in the semiconducting state, corresponding to oscillator 2 in Figure 1.15, can be associated with transitions of carriers trapped within the split V $3d$ bands; in particular, from the occupied $3d_{||}$ to the $3d_{\pi}$ band.[81,101] Upon transition, as the split bands come together, this oscillator generates the free-electron response of the VO_2. It is this oscillator which will contribute the most to the LSPR damping for NP arrays with resonances around 800 to 1000 nm. These two oscillators essentially describe the major features of the dielectric function of VO_2 relevant to the region between 600 nm and 1200 nm. For comparison, Table 1.2 compiles the values of the fit parameters from the Kakiuchida and Verleur VO_2 oscillators.

At wavelengths below 1700 nm (0.7 eV), the interband transitions of VO_2 dominate the optical response of the film.[25] Furthermore, the real part of the dielectric function remains positive above 1.1 eV ($\lambda \leq 1100$ nm), even in the metallic phase. Hence, in the optical region VO_2 does not behave like a metal. Transmission between 500 and 900 nm (Figure 6.1) increases in the metallic state compared to the semiconducting state, in agreement with work by Donev *et al.* and Qazilbash *et al.*; the latter authors reported an isosbestic point at 870±10 nm.[82,104] However, this isosbestic point is not seen in either the Verleur or the Kakiuchida experimental results or models.[38,101] Dicken *et al.* used ellipsometry to determine the dielectric function of their samples

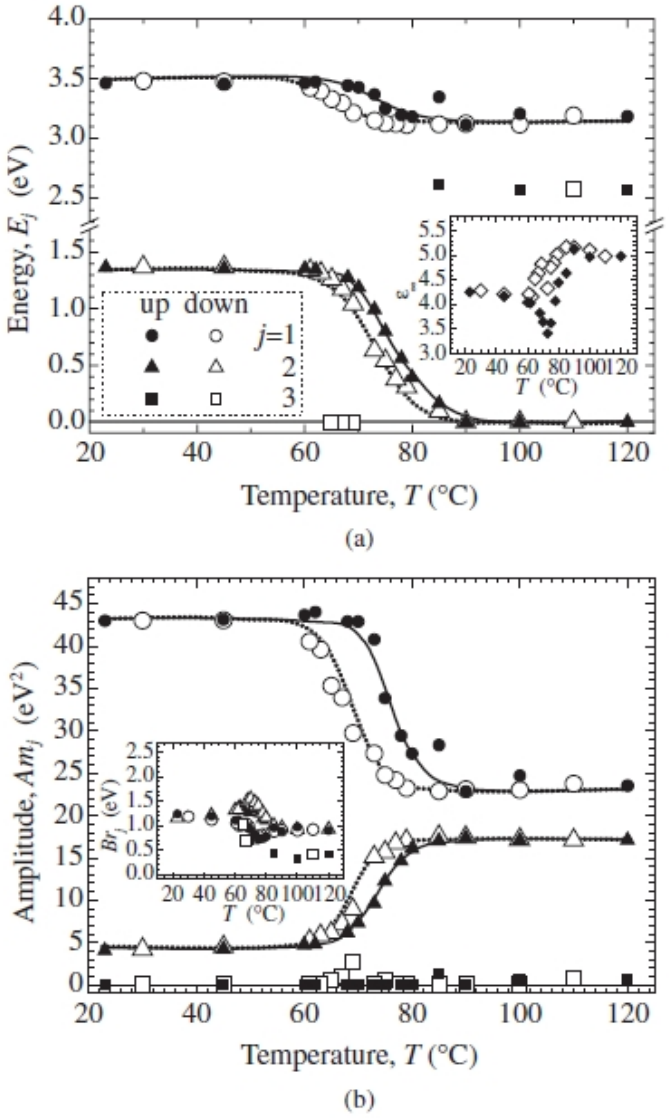

Figure 1.15: From [101], the hysteresis of the Lorentz oscillator parameters corresponding to energy (a) E_j and ϵ_∞ and (b) amplitude Am_j and broadening Br_j. The initial and final values for each parameter are described in Table 1.2. Kakiuchida *et al.* shows that two primary oscillators can describe the VO_2 dielectric function at VS and NIR energies.

for modeling purposes; they have not published their results.[21]

Finally, the relatively large losses due to interband transitions below 0.7 eV means that the effects of ϵ''_{m} must be included in our models. This is supported by the fact that the imaginary part of the VO_2 dielectric function is similar in magnitude and structure to that of Au, especially in the metallic state. The non-transparency of VO_2 leads to shifts and broadening of the LSPR not present when ϵ_{m} is taken to be real.

1.5 Structure of Dissertation

In this chapter, the essential background needed to understand the major results of this dissertation has been reviewed. Chapter II provides a detailed description of the fabrication and experimental techniques used, and Chapters III through V present the major experimental results. In each of the experimental chapters, a brief introduction is presented followed by the specific details of the samples studied, an analysis of the experimental results, and finally conclusions that can be drawn from the experiment. A abstract is provided as a summary at the beginning of each chapter. In Chapter VI, we summarize the results and the unanswered questions from this research. The appendix contains a representative MATLAB® script used in the analysis of data (Appendix A), a submitted *Applied Physics Letter* describing the results of Chapter V (Appendix B), and a second MATLAB® script used for calculating the temperature rise due to laser heating, also described in Chapter V (Appendix C).

Table 1.2: Parameters for Lorentz oscillators describing VO_2 dielectric function as reported by Verleur *et al.* and Kakiuchida *et al.*, organized by the oscillator energy E.[38,101] Note the difference in units for the oscillator broadening (Br.) and amplitude (Amp.) terms due to a difference in parameterization for each study; specifically, Verleur normalized the Amp. and Br. by the oscillator energy. Oscillator numbers correspond to the number assigned by the author of the study. The row marked "Drude" corresponds to the free-electron response of the metallic state.

Semiconducting							
Verleur				**Kakiuchida**			
Osc.	E (eV)	Br.	Amp.	Osc.	E (eV)	Br. (eV)	Amp. (ev^2)
1	1.02	0.55	0.79				
2	1.30	0.55	0.474	2	1.4	1.2	4
3	1.50	0.50	0.483				
4	2.75	0.22	0.536				
5	3.49	0.47	1.316	1	3.5	1.2	43
6	3.76	0.38	1.060				
7	5.1	0.385	0.99				
–				3	0	–	≈ 0
ϵ_∞	4.26			ϵ_∞	4.3		
Metallic							
Verleur				**Kakiuchida**			
Osc.	E (eV)	Br.	Amp.	Osc.	E (eV)	Br. (eV)	Amp. (ev^2)
1	0.86	0.95	1.816				
2	2.8	0.23	0.972	3	2.6	0.4	0.1
3	3.48	0.28	1.04	1	3.2	0.99	23
4	4.6	0.34	1.05				
Drude	–	0.66	3.33 eV	2	0	0.99	17
ϵ_∞	3.95			ϵ_∞	5.0		

CHAPTER II

EXPERIMENTAL METHODS

In this chapter, we will present a summary of the methodology used to fabricate and analyze the gold::vanadium dioxide nanocomposites (Au::VO_2) samples studied. First, the arrays must be lithographically prepared using standard electron-beam lithography (EBL) techniques, as described in Section 2.1.2. Following the EBL process, the arrays are characterized by scanning-electron microscopy (SEM) and optical measurements (Sections 2.2.1 and 2.2.2) before depositing a 60-nm film of VO_2 using pulsed-laser deposition (PLD), as described in Section 2.1.4. The now coated arrays are again characterized by SEM and optical measurements. Finally, simulations are performed using finite-difference time-domain (FDTD) and finite-element (FE) computer programs. An overview of these programs and methods is presented in Section 2.4.

2.1 Sample Fabrication

As shown in Figure 2.1, the nanolithography process employed for this work consists of (1) spin-coating and annealing the electron-beam resist poly(methyl methacrylate) (PMMA) onto a cleaned, indium-tin-oxide (ITO)-coated substrate, (2) exposing the resist to an electron-beam of suitable energy, (3) chemically developing the resist to create the nano-sized pattern, (4) depositing gold on top of the resist by electron-beam (thermal) evaporation, and (5) chemically removing the resist to leave behind

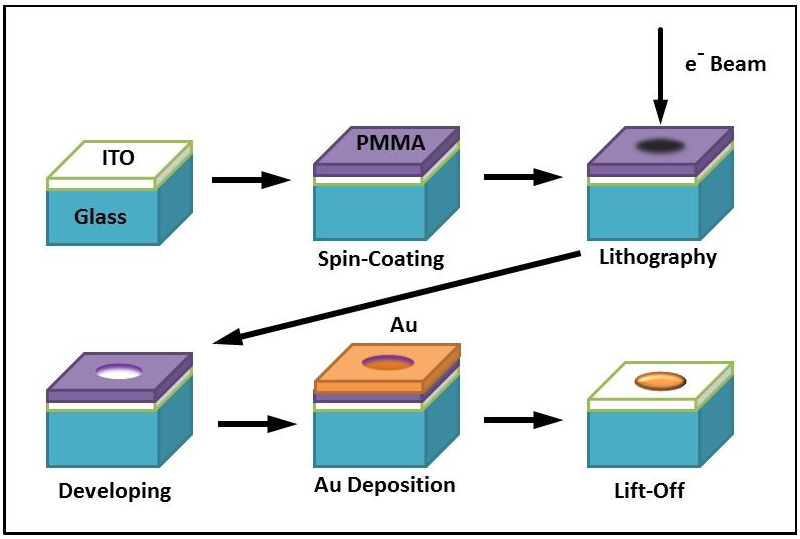

Figure 2.1: The EBL procedure: (1) spin-coating and annealing poly(methyl methacrylate) (PMMA), an electron-beam resist, on to a cleaned, ITO-coated substrate, (2) exposing the resist to an electron-beam of suitable energy, (3) chemically developing the resist to create the nano-sized pattern, (4) depositing gold (or other material) on top of the resist by electron-beam (thermal) evaporation, and (5) chemically removing the resist to leave behind the desired pattern of nanostructures.

the desired pattern of nanostructures. In the following sections we will discuss each step of this process in detail, starting with preparation of the substrate and followed by the lithography process.

2.1.1 Substrate Preparation

Samples were produced on transparent, ITO-coated, Corning 1737 glass substrates purchased from Delta Technologies (product number CB-90IN) with dimensions $5 \times 5 \times 0.5$ mm. The primary purpose of the ITO is to conduct electrons from the surface during EB lithography or microscopy to prevent their accumulation, which results in charging of surface. Secondly, the ITO provides for more stable adhesion of Au NPs

to the substrate.[105] The nominal thickness of the ITO is quoted by Delta Technologies as 15 to 30 nm, with a nominal transmittance of the ITO-coated substrate of 88% at optical wavelength (`http://www.delta-technologies.com/products.asp?C=1`). The sheet resistance is quoted to be 70 to 125 Ω for these thicknesses. The nominal complex index of refraction for ITO quoted by Delta is $n = 1.775 + 0.012i$; this value strongly depends on the fabrication technique.[106,107]

Substrates were cleaned using a standard protocol consisting of dipping and agitating the substrate for up to a minute in beakers of room-temperature acetone, methanol, and deionized water (DI) in sequence. A cotton swab or a clamped chemical wipe was also used to remove large particles of contaminant from the surface in before and during the acetone dip. The substrate was inspected visually and the process repeated if necessary. The samples were then dried using filtered air.

Immediately following the cleaning procedure, the EBL resist, a 2% solution of PMMA in anisol with a molecular weight of 950,000 (MicroChem product designation 950PMMA A2 resist), was spin-coated on to the substrate to a thickness of approximately 60 nm. This is approximately three times that of the intended thickness of the Au; this "rule of thumb" is chosen to decrease the likelihood of poor lift-off results after Au deposition.[108] Spin coating was done at 4000 rpm for 45 s, according to the spin-curves provided by MicroChem to achieve the desired thickness for the molecular weight and concentration of the solution used.[108] The thickness was confirmed by single-wavelength ellipsometry measurements. Following spin-coating, the substrate and resist are annealed at 180°C, well above the glass-transition temperature for PMMA (between 95 and 106°C), for 60 s.[108]

The properties of the PMMA resist directly determine the resolution that can be achieved by EBL. The PMMA with molecular weight of 950,000 allows the highest contrast between the developed and undeveloped portions of the film compared to PMMA with smaller weights, thus increasing the resolution of the lithography. The 2% solution of PMMA in Anisol was chosen because it could be spin-coated to the smallest thickness compared to higher concentrations.[108]

2.1.2 Electron Beam Lithography

Electron-beam lithography (EBL) has been used since the 1960s and PMMA has been used as a resist since later in that decade. The technique has become essential for many industrial and research efforts, as it allows for precise and accurate positioning of nanostructures.[109] The EBL system used in this work is the Raith e-Line, shown in Figure 2.2. Raith claims resolutions down to reproducible 5 nm lines, consistent with reported resolution limits in the literature of sub-10 nm reproducible features.[109,110] The precise resolution limits depend on many factors, including the resist, accelerating voltage, and the lift-off protocol used.[110]

For the samples in this study, the accelerating voltage used was 10 kV at a working distance of 10 mm. A higher accelerating voltage V_{a} could have been used to increase resolution by decreasing the number of scattered primary and secondary electrons interacting with the resist;[109] however, this was not necessary for the size requirements of the arrays produced. The increased scattering in the resist at lower V_{a} also means that a smaller dose of electrons is needed to expose the pattern to be written. Mild overexposure would increase the desired particle diameters, and thus redshift the

Figure 2.2: The Raith e-Line EBL system at Vanderbilt University.

LSPR. Major overexposure, which is more common for large-area exposures compared to arrays of NPs, hardens the PMMA to the chemical developer used to dissolve the damaged PMMA (Section 2.1.3). The 7.5 μm aperture of the EBL was used in order to limit the beam current to less than 15 pA, and typical dosages ranged from 80–100 μC/cm^2.

For spectroscopic studies, arrays were generally the size of the write field, or the region of the substrate to be exposed without moving the translation stage, with lateral dimensions of 100 μm. However, for transient absorption measurements, the apparatus made it difficult for optical alignment with arrays of that size. Therefore, significantly larger arrays were created, with lateral dimensions of 250 μm, 500 μm, and 1 mm. Although microsecond dwell times were required to get the necessary dose, the stage-settling time was on the order of milliseconds per particle. For a

100 μm array with a grating constant (distance between particles) of 450 nm, there are 49,000 particles. For a sample with multiple arrays (or several large arrays), write times ranged from 24–72 hours. The produced NP sizes ranged from radii R between 40 and 100 nm, NP thickness of 20 nm, and the array grating constants were typically between 350 to 500 nm. Exact details of each geometry is presented at the beginning of Chapters III through V.

2.1.3 Development, Deposition of Au, and Lift-off

Following EBL, development of the sample was done using a 1:3 solution of methyl isobutyl ketone (MIBK) and isopropanol. The low concentration allows for slower development, but higher resolution. The sample was immersed and agitated in the the developer for 60 s followed by 30 s of pipette rinsing with the developer. The developed sample was then dried with filtered, pressurized air and annealed on a hot plate at 100°C for 90 s to evaporate any residual developer or water.[108] Gold was then thermally deposited via electron-beam evaporation to a thickness of 20 nm as measured *in situ* by a quartz crystal thickness monitor.

Following gold deposition, the procedure for removing the remainder of the resist, known as "lift-off," was performed using MicroChem's Remover PG™, a proprietary N-Methyl-2-pyrrolidone (NMP)-based solvent, in a procedure consistent with that outlined by MicroChem.[108] Specifically, three 100 mL beakers were filled with 40 mL of Remover PG and set in the middle of a hot plate. Two of these beakers were used to rinse the samples, while an analog thermometer was placed in the third and held in the middle of the liquid volume with a test tube clamp. The plate temperature

was set to 100°C. Once the temperature in the solvent reaches approximately 52°C, the temperature of the hotplate was lowered to 80°C and constantly adjusted so that the solvent temperature leveled out at 62°C. Empirical evidence suggests that this is an optimum temperature for our samples. The sample was then agitated in the first beaker for several minutes and sprayed with a pipette using the solvent in the second beaker. This process was repeated until as much of the visible gold film was removed from the sample as possible, and then continued for an additional minute to ensure that any residual PMMA/gold film was removed. Following this procedure, the sample was rinsed in acetone, followed by DI water, and finally dried with pressurized, filtered air.

To minimize particle reshaping during PLD, samples were then annealed for 2 min at 180°C on a hot plate. The reshaped particles had diameters 5 to 10 nm smaller and slightly more hemispherical shapes; further discussion of particle reshaping can be found in [54]. The particle diameters quoted in this dissertation refer to the reshaped ("final") particle.

2.1.4 Pulsed-Laser Deposition of VO_2

Pulsed-laser deposition (PLD) is a technique that has been used in the thin-film community since the 1960s.[111,112] The physics of the ablation process is complex, requiring knowledge of thermodynamics, hydrodynamics, and optics.[111] Laser energy is absorbed through excitation of free carriers in a concentrated volume near the surface of the metal.[111] The high energy density results in breaking of chemical bonds and explosive vaporization occurs. In addition to interactions with electrons

and the crystal lattice, absorption by the ablation plume can also play a role in the deposition kinetics. The ablation plume, shown in the right panel of Figure 2.3, is an energetic plasma that contains photoelectrons, ions, ground state and excited atoms, atomic clusters, and particulates as large as micrometers in size.[111,113] For thin film deposition, it is necessary to reduce the number of large particulates to ensure a smooth film. This is accomplished by limiting the transfer of kinetic energy to large particulates by operating at near ablation-threshold fluences and increasing the time between laser pulses. The versatility of PLD allows deposition to be done in vacuum or, as is the case for VO_2 deposition, a background gas.

The PLD apparatus for our experiments can be divided into two systems. The first is the PLD chamber and vacuum system (PVD Products, Epion 3000). The chamber was designed to hold vacuum down to $\sim 10^{-7}$ Torr using a turbomolecular pump system (Varian, Model 969-9048). The laser and beam steering optics comprise the second part of the PLD system and are shown schematically in the left panel of Figure 2.3. The laser was a pulsed KrF excimer (Lambda Physik, Compex 205) with wavelength 248 nm and nominal pulse duration 20 ns.

The two-step recipe used at Vanderbilt University for producing VO_2 through PLD is well established.[114] In our experiments, a vanadium metal target was ablated in a 10 mTorr O_2 atmosphere at a pulse repetition rate of 25 Hz and average pulse energy of 380 mJ. The spot-size of the laser on the target, as estimated from burn-paper measurements, has an approximate elliptical area of 0.32 cm^2, giving a fluence of 1.2 J/cm^2. During ablation, the vanadium target was rotating while the laser spot rastered across the surface so that the entire surface of the target was ablated

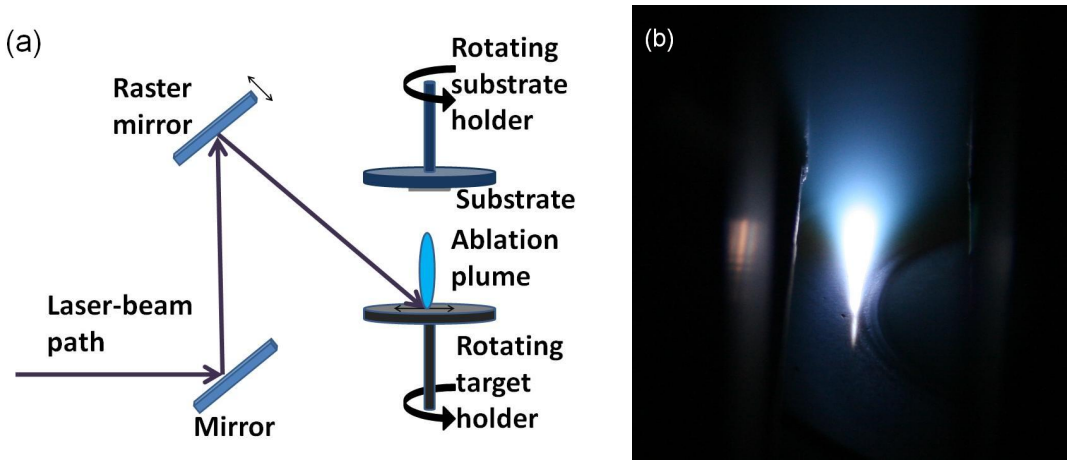

Figure 2.3: (a) Schematic representation of the PLD optics and (b) an image of the PLD plume during ablation of a vanadium target. Image used from personal collection.

smoothly; this was done to prevent grooves in the surface that can lead to non-uniform film deposition. The substrate holder, positioned at a height of approximately 7 cm above the target, also rotated to ensure different regions of the substrate sample different parts of the plume to ensure uniform deposition. This step, done at room temperature, produced films of VO_x, $x \approx 1.7$.[114] Following deposition, the films were annealed at 450°C for 40–45 min in 250 mTorr of O_2 to produce stoichiometric VO_2. Too high an anneal temperature or annealing for too long leads to a stoichiometry of V_2O_5. A typical VO_2 film contains a small amount of V_2O_5.[114] The film and substrates were left to cool in the O_2 background gas before being removed from the chamber and characterized.[113,114]

2.2 Sample Characterization

Following fabrication, the samples were imaged using scanning electron microscopy (SEM) before transmission and extinction measurements were performed. The following sections will discuss these techniques. A detailed analysis of extinction will be given in Section 2.3.2.

2.2.1 Scanning Electron Microscopy

The samples were characterized by imaging the array both before and after VO_2 deposition with scanning electron microscopy (SEM). This was done on the previously mentioned Raith e-Line system at an accelerating voltage of 10 kV and working distance of 10 mm. This was identical to the settings used for writing the array patterns and described in Section 2.1.2. However, instead of using the 7.5 μm aperture, as in the case for pattern writing, we imaged with a 30 μm aperture. The larger aperture increases the signal-to-noise ratio by increasing the beam current (i.e., the number of electron scattering events).

Imaging was done using a detector located directly above the sample near the electron-steering optics. At this angle, most of the electrons collected are due to back-scattering from the sample surface, as opposed to secondary electrons, which are typically emitted at a higher angle relative to the normal. To image individual Au NPs, the magnification was between 30–40 kX, allowing for imaging at less than 10 nm resolution, but still capturing several NPs in the image. Figure 2.4 shows SEM images of the array structure with and without VO_2. Although the Raith e-Line

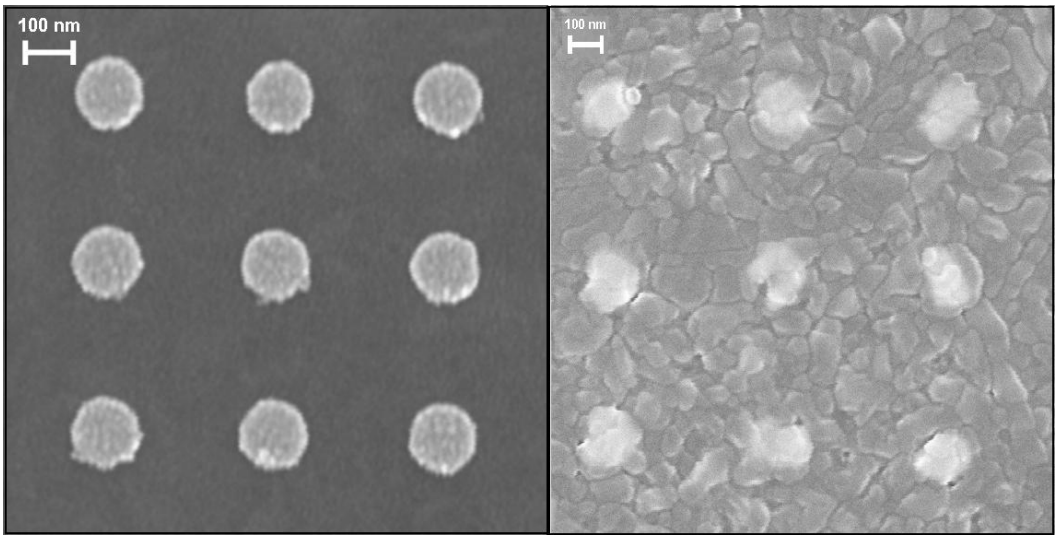

Figure 2.4: SEM images of Au NP arrays (left) before and (right) after VO_2 deposition. Images are not of the same arrays. The granular nature of the VO_2 film is clearly seen.

is capable of higher magnification, imaging above approximately 200 kX is difficult due to building vibration (Figure 2.5). This vibration does not affect patterning of the arrays since the write time for a single particle is microseconds compared to millisecond vibrations.

2.2.2 Transmission Hysteresis and Spectroscopy

After imaging, optical transmission and spectroscopy measurements are used to further characterize the sample. A diagram of the apparatus is shown in Figure 2.6. A fiber-coupled Spectral Products tungsten lamp (ASBN-W-L) with a near-blackbody spectrum at a color temperature of 3000 K was used as a white-light source. Broadband VS-to-NIR fibers supplied by Thorlabs (BFL37-400, pure silica core, hard poly-

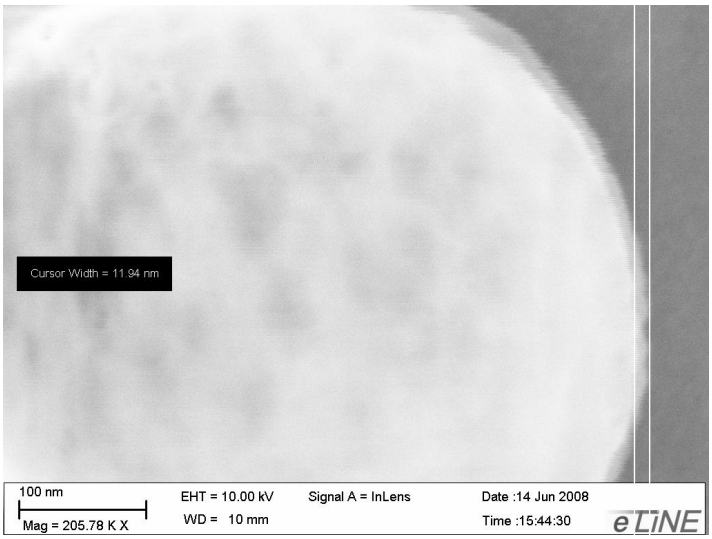

Figure 2.5: SEM image of a carbon nanostructure that forms on the surface when the EB dwell in a single spot for a 3 to 15 seconds. The cursor measurement shown by the vertical lines on the right is of the amplitude of building vibrations (11.94 nm) that adversely affect resolution. This has been alleviated somewhat since the image was taken (June 14, 2008) due to additional stabilization of the air-table on which the EBL system is mounted, but can still affect imaging. Below the image are details on EBL settings when the image was made.

mer cladding) were used to transmit light into the transmission apparatus. The light was passed through a cage-mounted 50:50 beam-splitter (Thorlabs, CM1-BS1) so that light reflected from the sample and optics behind the sample was then transmitted into a black and white camera (Watec, 902B). The light transmitted through the beam-splitter was focused by a 5X microscope objective with numerical aperture (N.A.) 0.12 to a spot roughly the size of a 100 μm/side array, as estimated by the image made on the camera. The spot size is only an estimate, as the autogain "feature" of the camera can make the spot appear somewhat larger or smaller than its actual size. Light transmitted through the sample was then collected by another 5X

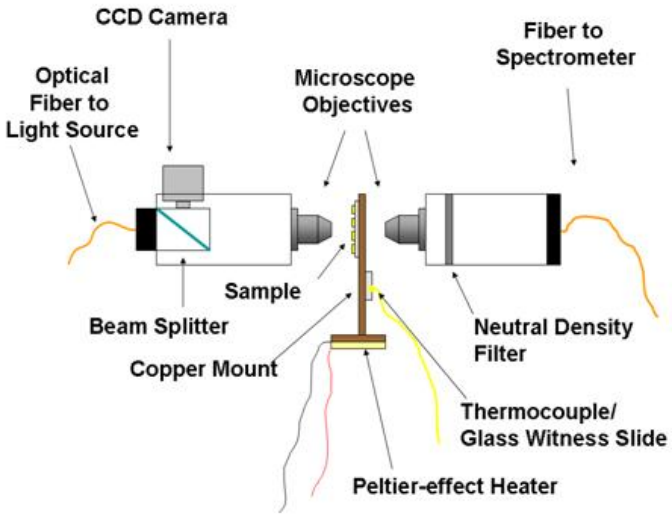

Figure 2.6: Schematic representation of the optical transmission apparatus used for transmission hysteresis measurements and spectroscopy.

objective (N.A. 0.20) with, depending on the measurement, either an Indium gallium arsenide (InGaAs) detector (Thorlabs, DET10C or PDA400) or a fiber (Thorlabs, BFL37-400) connected to the spectrometer placed at the focal point of the objective.

As VO_2 undergoes its first-order phase transition from a semiconductor to a metal, there is a change in overall transmission. The ratio between metallic state transmission to semiconducting state transmission, or contrast, is greatest at wavelengths above 1000 nm. At these wavelengths, the transmission decreases and reflectivity increases as the VO_2 grains become metallic. For this reason, we used an InGaAs detector, which is most sensitive in the NIR, for measuring the optical transmission hysteresis of the film. Two different InGaAs detectors have been used for this study at various times. One was an amplified detector (Thorlabs, PDA400) with variable gain, which has been discontinued by Thorlabs, and the second was a biased detector

(Thorlabs, DET10C) with a 10 ns rise time. Both had a wavelength sensitivity from 700 to 1800 nm. For comparison purposes, Thorlabs biased-Si detectors are sensitive up to 1100 nm, where the Si becomes transparent. The detector was connected to a lock-in amplifier (Stanford Research Systems, SR510) to increase signal-to-noise and data were recorded using a LabView program specifically created for hysteresis measurements. The program recorded the signal (light intensity) from the detector/lock-in amplifier while simultaneously recording the sample temperature as a function of time. The temperature was measured using a K-type surface-mounted thermocouple (temperature range $-200°$C to $1250°$C, limits of error: $\pm 2.2°$C or 0.75%) purchased from OMEGA (CO3-K). The thermocouple was clamped onto a 0.5 mm, glass witness substrate with thermal paste (OMEGATHERM® 201), also provided by Omega, to ensure a reliable thermal connection. From the measurement, a plot of intensity I versus temperature T plot was constructed, showing the hysteretic behavior of VO_2 and Au::VO_2 nanocomposites(Figure 2.7).

A transmission hysteresis measurement is one of the most efficient methods for determining the quality of the VO_2 deposition since the phase transition is highly sensitive to the VO_x stoichiometry. A poor quality film with incorrect stoichiometry can exhibit a shifted transition temperature, an increased width, or a reduction in contrast.[25,114] The width and overall shape of the hysteresis also depends on the quality of the film, as a non-continuous film will significantly widen the hysteresis.[113,114] These same characteristics appear in hysteresis measurements of film resistance. Figure 2.7 shows a typical transmission hysteresis measurement. The transition temperature T_{tr} is defined as the average temperature between the mid-points on the heating and

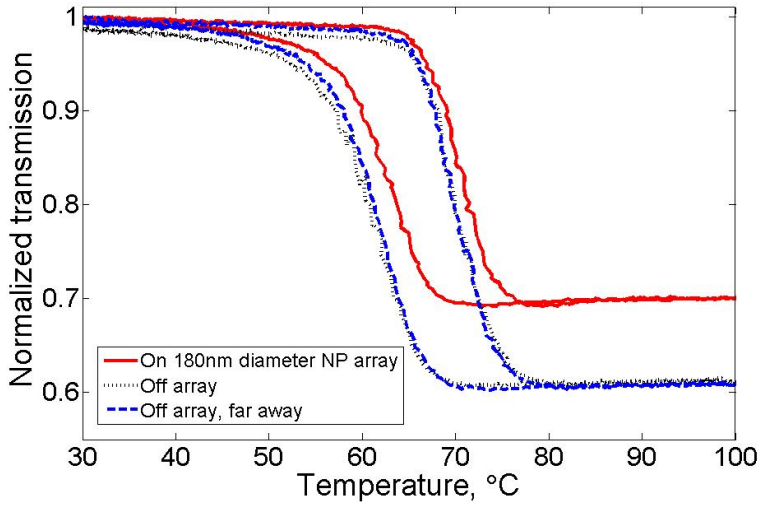

Figure 2.7: The hysteresis, a characteristic of first-order phase transitions, is reproducible and consistent from one location to another for a continuous film. As VO_2 switches between its semiconducting and metallic states, there is a hysteresis in its optical transmission. The plot shows measurements at three locations on an Au::VO_2 sample: on 180 nm particle array with a grating constant of 450 nm, off of the array but a few hundred microns aways, and far from the array (approximately 1 mm).

cooling curves during the transition, typically at 68°C. To determine this, the heating and cooling curves were each fitted with a four-parameter, generalized sigmoidal function of the form

$$I(T) = I_{\min} - \frac{I_{\max} - I_{\min}}{1 + \exp\left[-\left(T - T_c\right)/T_w\right]}, \tag{2.1}$$

where $I_{\min}$ and $I_{\max}$ are the minimum and maximum intensities measured, respectively, T_w is a parameter determining the width of the transition, and T_c is the midpoint temperature of the heating and cooling curves. Using an "H" or a "C" to distinguish between heating and cooling curve parameters, $T_{tr} \equiv \left(T_{cH} - T_{cC}\right)/2$.

Note that (2.1) is directly related to (1.16). The parameter T_{w} depends on how efficient the film grains switch.

Extinction was measured using an Acton SpectraPro 300i spectrometer by Princeton Instruments using a turret-based, 150 grooves/mm, high-resolution diffraction grating optimized for a center wavelength of 500 nm. Figure 2.8 shows the efficiency curve for the grating, indicating a significant decrease in efficiency as we move into the NIR. The CCD camera used for measuring the spectrum is made by Roper Scientific (Model number 7344-0001) and Peltier-cooled to $-45°$C. Being a Si-based CCD, the sensitivity drops off sharply at wavelengths in the NIR. The reduction in efficiency is evident in spectroscopic measurements as a decrease in the signal-to-noise ratio. To compensate for the noise, the data are smoothed over intervals of 101 of the 1340 wavelength data points using the standard Savitzky-Golay (SG) filter that comes with MATLAB® and described in [115]. Figure 2.12 shows the raw transmission spectrum (points) and the smoothed curve (solid line).

2.3 Experimental Techniques

In the following sections we discuss the two major experimental techniques used in this dissertion. Transient absorption measurements (Section 2.3.1) were of primary interest for studying the thermal interactions of the Au::VO_2 nanocomposites. In Section 2.3.2, a thorough discussion on extinction in absorbing media will be presented.

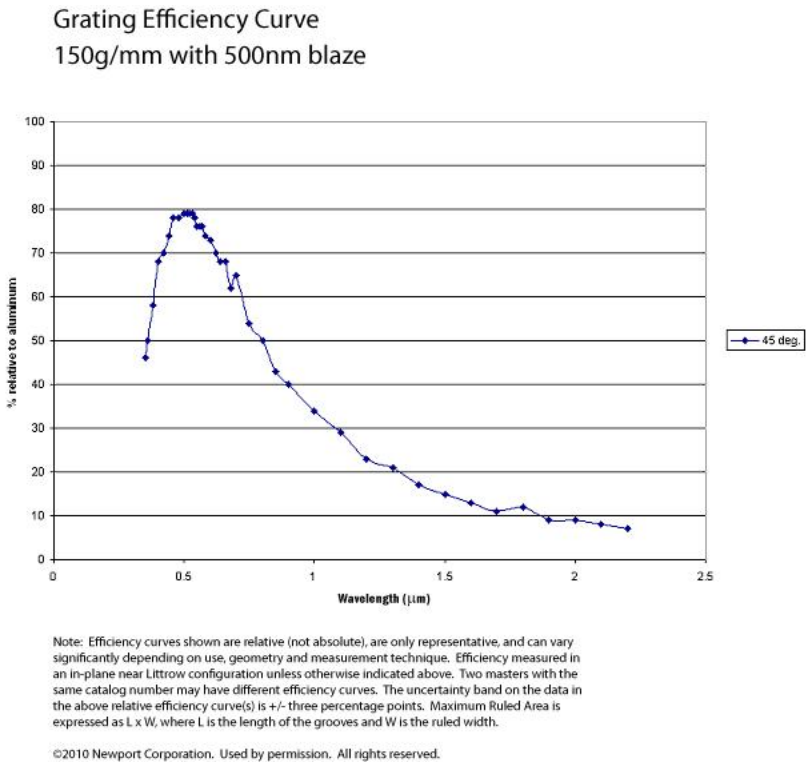

Figure 2.8: The efficiency of the Acton diffraction grating used for spectroscopic measurements. Figure provided by Newport Corporation.

2.3.1 Transient Absorption Apparatus

In Chapter V we explore the dynamics of low-power laser heating of the VO_2 and Au::VO_2 samples by transient absorption measurements. Figure 2.9 shows a schematic of the apparatus. A CW 785 nm, 100 mW diode laser (Meshtel, IS785-100, actual output 90 mW) serves as the pump source, while a 6 mW, CW 1550 nm laser diode (Thorlabs, ML925B45F) continuously probes the change in transmission through the sample. Illumination by the pump was controlled by a mechanical shutter; samples were irradiated for 5 s followed by an indefinite period of time for recovery. The pump and probe beams were partially collimated before passing through a 76 mm

diameter, 85 mm focal length lens, diverting both parallel laser beams to cross at the sample, which was placed at the focal spot. The spot size of the 785 nm beam was measured by a knife-edge experiment to be approximately 242 μm in diameter at the position of the sample; the probe beam was measured to be approximately 206 μm. Both measurements are shown in Figure 2.10. The diverging beams were made to pass through 50 mm lenses (not shown in Figure 2.9), focusing them onto separate biased detectors. A Si-detector (Thorlabs, DET10A) was used to measure the 785 nm laser and an InGaAs (Thorlabs, DET10C) was used for the 1550 nm laser. Finally, a Semrock 830 nm long-wave pass filter is placed in front of the InGaAs detector to minimize the amount of scattered 785 nm light entering the detector. Data were recorded using a USB-based oscilloscope (Crag Technologies, PicoScope PS3424, discontinued) and the included software. The PicoScope has a sampling rate of 20 MHz, well above what was needed for our experiments, which dealt with changes in transmission over a few milliseconds.

To ensure that the pump and probe beams overlapped, the two beams were first aligned on an infrared viewing card using a CCD camera and lens assembly. This was done by placing the card at the focal spot of the 76 mm lens and fine tuning the position using the alignment mirrors. Once the two beams were centered, the position of the card was noted, and the card was removed. The sample was then repositioned such that the front side of the sample was approximately in the same position as the card. To check the alignment, the shutter was opened, and the beams were scanned across the sample by moving the sample holder. To check the alignment, the sample was heated to approximately 35°C to increase the contrast achieved by

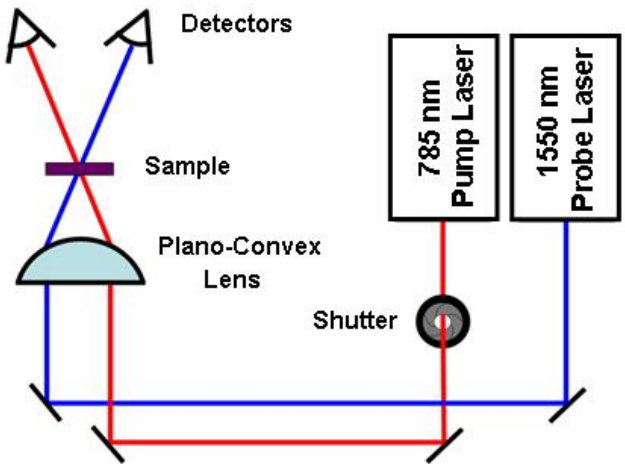

Figure 2.9: Schematic representation of the apparatus for transient absorption measurements.

opening the shutter. The shutter was then opened, and the probe was adjusted to achieve maximum contrast. The shutter was then closed to ensure that the signal was still maximized on the detector. To align the beam on the NP array, the pump was left shuttered, and the probe signal was measured as the array was moved under the beam until the probe signal was minimized.

2.3.2 Extinction

The transmission measurements conducted with the previously described apparatus, both integrated and spectrally resolved, quantify the loss of light intensity that reaches the detector due to the presence of either particles or a film. Consider a plane-wave source and detector configuration, in vacuum, where the source is emitting with a certain intensity and wavelength λ. The detector, located in the far-field

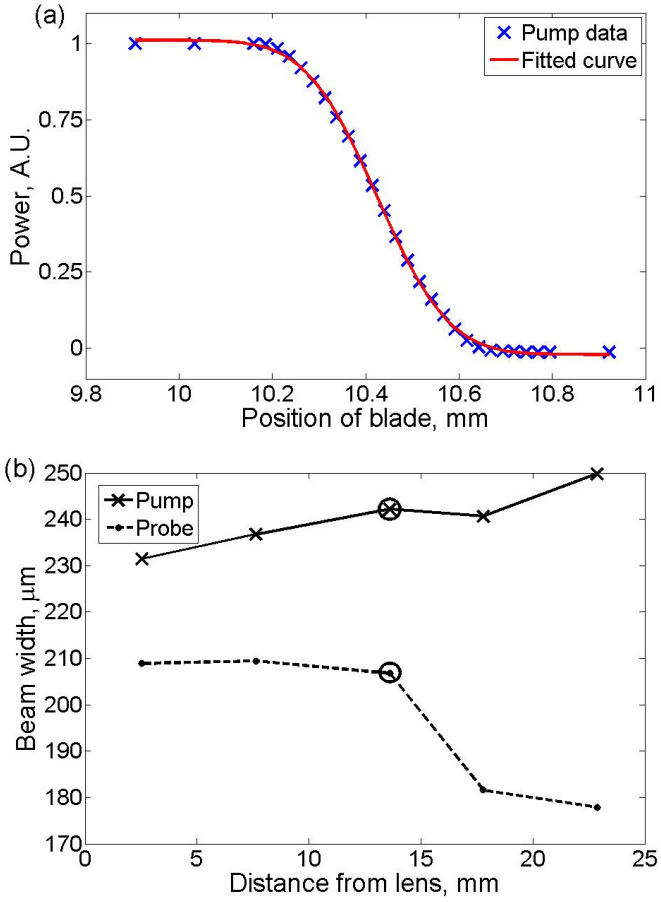

Figure 2.10: (a) The data and fit for the knife-edge measurement of the spot size for the 785 nm pump beam. (b) The width of the pump and probe beams as a function of distance from the lens. The sample was placed the position of the circled data point, coinciding to the intersection of the pump and probe.

and normal to the direction of wave propagation, receives an incident power $P_0 = I_0 A$, where I_0 is the incident intensity after losses due to reflection, and A is the area of the detector. If an absorbing medium, such as a thin-film of VO_2, of thickness z and complex index of refraction $n = n' + in''$ is placed between source and detector, then

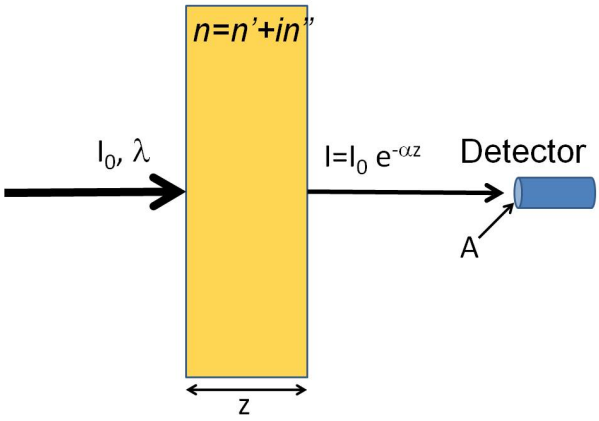

Figure 2.11: A schematic describing the geometry discussed in Section 2.3.2.

the incident intensity is diminished according to Beer's Law,[5,44]

$$I = I_0 e^{-\alpha z}, \tag{2.2}$$

where $\alpha = 4\pi n''/\lambda$ is the attenuation coefficient.

If instead of a continuous medium, we placed a slab of particles between the source and detector, the overall physics is the same. Each particle diminishes the intensity by either absorbing or scattering (reflecting) photons according to its extinction cross section C_{e}. Assuming that the particles are identical in shape, size, and spatial dispersion, we can define an effective attenuation coefficient due to this extinction as $\alpha_{\mathrm{e}} = \rho_{\mathrm{N}} C_{\mathrm{e}}$, where ρ_{N} is the number density of the particles.

2.3.2.1 Extinction in Absorbing Media

The Au::VO_2 samples consist of particles embedded in an absorbing medium. The typical definition of extinction cross section given in most textbooks is derived and discussed based on particles embedded in a non-absorbing medium. This is partly because the interpretation of experimental results and derivations becomes more complicated in the former case. Bohren and Huffman address this in their text, referencing a paper by Bohren and Gilra;[44,116] however, their result is not without controversy since their mathematical definition of extinction relies on an arbitrarily defined surface of integration far from the particle.[55,117] Due to the relatively small optical path length of light within an absorbing medium, this definition is impractical from an experimental point of view. It fails when measuring NPs embedded in a thin film, as the detector is not located within the absorbing medium.

Lebedev *et al.* improve on the definition of extinction in absorbing media by integrating over just the volume of the particle.[55] However, according to Videen and Sun, this definition does not properly account for the additional absorption within the medium due to the scattering by the particles. Instead, they resort to the optical theorem to arrive at a definition and derivation that takes this additional absorption into account.[117] This solution relies on the interpretation that extinction is the effective reduction of detector area due to the presence of a particle.[44,55]

To understand this, we consider the implications of the optical theorem. For a system of particles in non-absorbing medium, the power incident on the detector P

is given by

$$P = P_0 - P_e + P_s = I_0 \left[A - C_e + C_\Omega \left(\Omega_D \right) \right], \tag{2.3}$$

where P_e is the power extinguished by the particles, P_s is the additional power scattered into the detector due to the finite solid angle Ω_D that it subtends, i.e., due to the numerical aperture of the collection objective. Here, C_Ω is the effective scattering cross section into this solid angle. If our detector is far enough away that C_Ω is small and only forward scattered light is detected. The two remaining terms suggest that extinction cross section is well-defined as the effective change in area of a detector due to the presence of the particles.

For an absorbing medium, I_0 is additionally attenuated by a factor of $\exp\left(-2k''z\right)$, where k'' is the imaginary part of the wavenumber in the medium ($\alpha = 2k''$). As discussed in the next section, this additional factor drops out of the definition for cross section, but must be accounted for when determining the energy absorbed into the film. Furthermore, light rays scattered from the particles have a longer path length in the absorbing medium, and thus is further attenuated. This definition of extinction accounts for the additional scattering since it is the presence of the particles that lead to this loss of intensity. Finally, before describing the measurements it is worth considering what is being measured. In particular, it is important to distinguish between measuring the macroscopic optical properties of both the absorbing medium and NPs and measuring specifically the extinction due to the particles. The definition of extinction cross-section discussed above is referring specifically to that of the NPs present in the medium and not the system as a whole. This allows the LSPR response

of the array of NPs to be distinguished from the high absorption in the medium.

2.3.2.2 Extinction Measurements

The definition of particle extinction is reflected in the measurement of the particle LSPR. Figure 2.12 shows a comparison of the raw data to the processed data. First, the light source was blocked and a measurement of the background light was made. This "background" spectrum was subtracted from all subsequent measurements. Then a reference spectrum or "flat field" (FF) was acquired, measuring the intensity of light passing through plain VO_2 film $I_{\mathrm{FF}}(\lambda)$ in a region of the sample close to the arrays. This spectrum depends not only on the physical properties of the VO_2, but also on the substrate, the efficiency of the optics and fibers, the spectrum of the source I_0, and the efficiencies of the diffraction grating and CCD detector array. We represent the instrumental efficiencies as $\eta_{\mathrm{I}}(\lambda)$. The attenuation due to the substrate $\eta_{\mathrm{s}} = \exp\left[-\alpha_{\mathrm{s}}(\lambda) z_{\mathrm{s}}\right]$ (Beer's Law), where α_{S} and z_{s} represent the attenuation coefficient and thickness of the substrate, is less than 7% at visible and NIR wavelengths according to the material data sheet provided by Delta Technologies. Therefore, I_{FF} is given by

$$I_{\mathrm{FF}} = \eta_{\mathrm{I}} \eta_{\mathrm{S}} I_0 e^{-\alpha_{\mathrm{m}}(\lambda) z}, \tag{2.4}$$

where α_{m} is the attenuation (of the medium) due to the VO_2 film. Without knowing η_{I}, this measurement by itself does not provide much information. We are more concerned, however, with the extinction of the Au NPs.

To determine the extinction of the particles, we then measured the intensity of

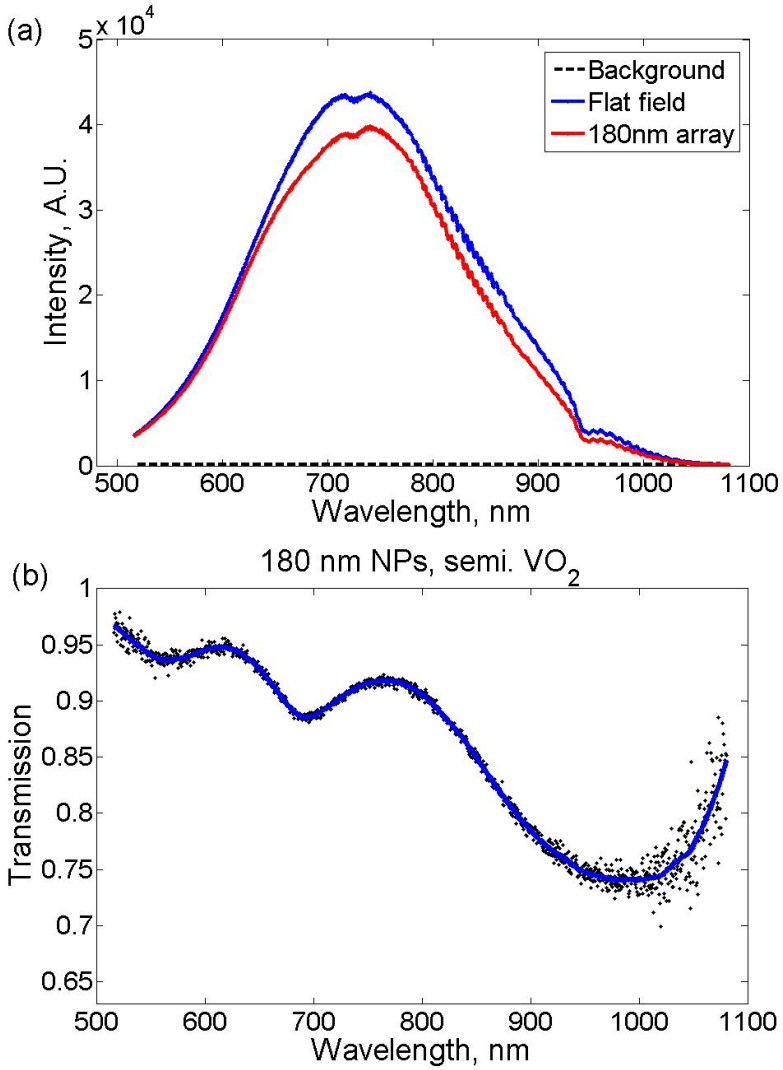

Figure 2.12: A comparison of the (a) unprocessed data from the spectrometer and (b) the same, raw data after referencing the sample spectrum to the FF (black data points) and then smoothed (solid blue curve) using the SG filter. The spectrum is referenced to the plain VO_2 film, as described in Section 2.3.1. The array consisted of the 180 nm diameter particles with a 450 nm grating constant used in Chapter III.

light I_{NP} reaching the detector after passing through the Au::VO_2 sample. This gives an extra term in the exponential of (2.4) equal to $-\alpha_{\mathrm{e}} z = -\rho_{\mathrm{N}} C_{\mathrm{e}} z$, and leads to

$$I_{\mathrm{NP}} = I_{\mathrm{FF}} e^{-\rho_{\mathrm{N}} C_{\mathrm{e}} z}. \tag{2.5}$$

The transmission spectrum is defined as the ratio of the intensity through a sample to that of the intensity without the sample. Therefore, the transmission through the array T_{NP}, referenced to the FF, is

$$T_{\mathrm{NP}} = \frac{I_{\mathrm{NP}}}{I_{\mathrm{FF}}} = e^{-\rho_{\mathrm{N}} C_{\mathrm{e}} z}, \tag{2.6}$$

and shown in Figure 2.12(b). The smoothed curve is taken to be the transmission spectrum and shown in all figures containing spectroscopic data. With some manipulation, we can use this measurement to calculate the extinction efficiency Q_{e} of the particles as embedded in the VO_2:

$$Q_{\mathrm{NP}} = -\frac{\ln T_{\mathrm{NP}}}{f_{\mathrm{A}}}, \tag{2.7}$$

where f_{A} is the areal packing fraction.

2.3.3 Errors in Extinction Measurements

There are several sources of error that can be significant in extinction measurements. For one, the derivation of extinction derived in Section 2.3.2.1 assumed a plane-wave source. Because we are interested in the extinction due to an finite size

array of NPs, we must focus the light source to a spot of approximately the same size as the array. If the spot is larger than the array, the measured extinction cross section will have a decreased magnitude because of an effective reduction to the particle density $\rho_{\mathrm{N,eff}} = \rho_{\mathrm{N}}\xi_{\mathrm{A}}$, where $\xi_{\mathrm{A}} = A_{\mathrm{array}}/A_{\mathrm{spot}}$, with A_{array} and A_{spot} being the area of the array and illumination spot, respectively.

The finite numerical aperture (N.A.) of the collection optics allows additional photons to scatter into the detector. This reduces the measured extinction cross-section as shown by the third term in (2.3). The effective extinction cross section $C_{\mathrm{e,eff}}$ is therefore $C_{\mathrm{e,eff}} = C_{\mathrm{e}} - C_{\Omega}(\Omega_{\mathrm{D}})$. Quantifying C_{Ω} requires measuring the scattering efficiency in the forward direction, which, for large NPs can be a significant contribution. For our N.A. of 0.20 the solid angle Ω over which radiation is collected is $\Omega = 2\pi(1 - \cos\arcsin 0.20) = 0.13$. For a detector that is far from the sample, C_{Ω} is proportional to Ω. As an upper limit to the error, consider $C_{\mathrm{e}} = C_{\mathrm{s}}$ — the case in which all of the extinction is due to scattering. Then $C_{\mathrm{e,eff}} = C_{\mathrm{e}}(1-\Omega) = 0.87C_{\mathrm{e}}$, and the absolute error that we can expect for the extinction cross section as a result of a N.A.$= 0.20$ is $\lesssim 13\%$ at each wavelength. We generalize this by defining the reduction in cross section due to the N.A. of the collection optics as ξ_{Ω}, so that $C_{\mathrm{e,eff}} = \xi_{\Omega}C_{\mathrm{e}}$.

Variations in VO_2 thickness across the sample can also lead to errors in the extinction because the VO_2 FF was taken under different conditions than the array. The variation in transmission has been mapped over the samples used for the low-power switching measurements described in Chapter V, and the results are shown in Figure 2.13. For this sample, each array is 500 μm on a side; the axes are in arbitrary units of relative position. The numbers printed on each contour are the transmission

referenced to an arbitrarily defined origin, and the contours are extrapolated through the arrays, which were not measured since the extinction of the NPs could not be excluded. The results show that the transmission varies from that of the FF varies over a range of no more than $\pm 0.03\%$ in the region of the arrays. This result is consistent from one sample to the next. Changes in the transmission may be due either to variations in (1) the thickness of the film, (2) small variations in granularity over large ($\sim$ 100 μm diameter) regions of VO_2, and (3) variations in absorption of the VO_2 effective medium. To account for variations in thickness, we define an effective VO_2 thickness $z' = z + \delta z$. Changes in absorption constant may also be a source of relative error since the granular nature of VO_2 film leads to statistical variations in the effective medium of the film. However, due to the logarithmic relation between transmission and absorption, errors in absorption coeffiecient would neglible based on the $\pm 0.03\%$ variations of transmission shown in Figure 2.13.

Other errors can come from the light source drifting over time. These errors are minimized by taking multiple reference spectra during the course of characterizing a sample and carefully monitoring the flat field for changes. For the dimer study conducted in Chapter IV, the sample mount was designed to rotate in such a way as to allow alignment of the dimer axis with the polarization axis. The structure of this particular mount increased the likelihood of reducing the illumination passing through the sample and into the detector because of its increased thickness over previous designs. This could result in errors with the flat field intensities from one position to the next. We can account for both of these sources of error by defining an effective incident intensity $I_0' = \xi_I I_0$, where ξ_I is the factor by which the intensity

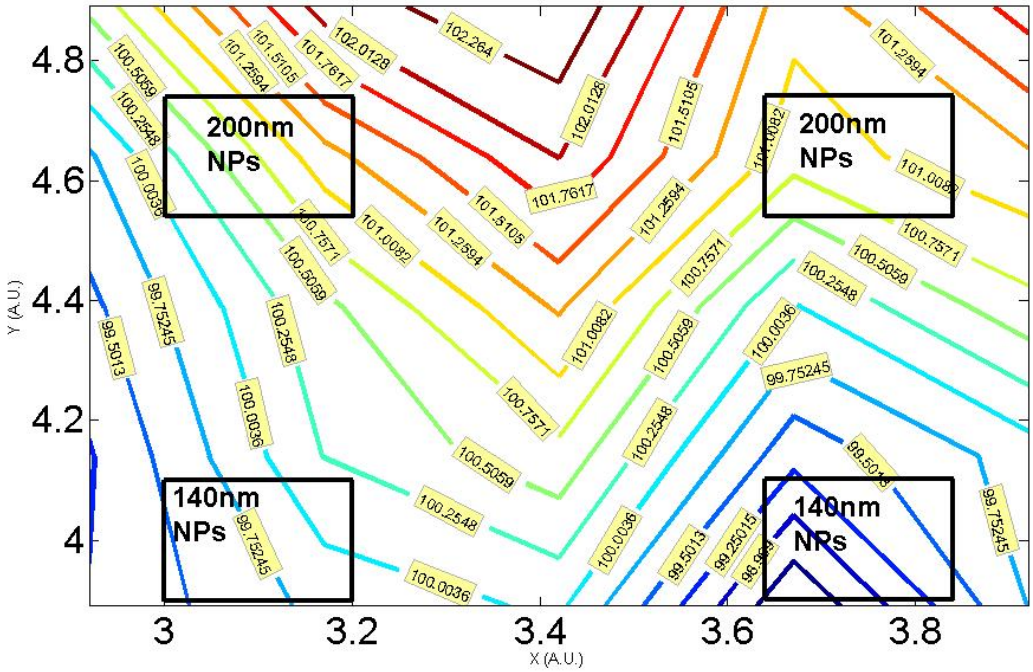

Figure 2.13: Variation in transmission normalized to the transmission at the origin and mapped in the region of interest for a sample with 500 μm arrays and particles of diameter 140 nm and 200 nm. The X and Y axes are arbitrarily defined; regions covered by an array, contained in the black boxes above, were not measured. The curves in these regions are extrapolated.

of the source has changed.

Without loss of generality, we take the FF measurement to be that given by (2.4) and introduce the terms with error into (2.5). Simplifying and rearranging the terms, we find that the measured transmission through the array T'_{NP} is

$$T'_{\mathrm{NP}} = \xi_{\mathrm{I}} \exp\left[-\left(\delta\alpha\, \delta z + \alpha_{\mathrm{m}} \delta z + \delta\alpha z\right)\right] \exp\left[-\rho_{\mathrm{N}} C_{\mathrm{e}} \xi_{\mathrm{A}} \xi_{\Omega}\left(z + \delta z\right)\right]. \tag{2.8}$$

We define $\Xi_{\mathrm{ext}} \equiv \xi_{\mathrm{I}} \exp\left[-\left(\delta\alpha \quad \delta z + \alpha_{\mathrm{m}}\, \delta z + z\, \delta\alpha\right)\right]$ as "external" error since the

terms can be separated from the extinction coefficient. Using $\rho_{\mathrm{N}} = 1/V_{\mathrm{cell}}$, where $V_{\mathrm{cell}} = A_{\mathrm{cell}}(z + \delta z)$ is the volume of the array unit cell, we can write (2.8) in terms of extinction efficiency and Ξ_{ext} as

$$T'_{\mathrm{NP}} = \Xi_{\mathrm{ext}} \exp\left(-f_{\mathrm{A}} Q_{\mathrm{e}} \xi_{\mathrm{A}\Omega}\right), \tag{2.9}$$

where f_{A} is the areal packing fraction and $\xi_{\mathrm{A}\Omega} = \xi_{\mathrm{A}}\xi_{\Omega}$. Finally, solving for Q_{e}, we get

$$Q_{\mathrm{e}} = \left(f_{\mathrm{A}}\xi_{\mathrm{A}\Omega}\right)^{-1}\left(\ln \Xi_{\mathrm{ext}} - \ln T'_{\mathrm{NP}}\right). \tag{2.10}$$

The impact of "external" errors is to vertically shift the entire extinction curve by $\ln \Xi_{\mathrm{ext}}$; "internal" errors lead to a factor $\left(f_{\mathrm{A}}\xi_{\mathrm{A}\Omega}\right)^{-1}$ multiplying the extinction spectrum. In contrast, for the transmission spectrum both sources of error lead to a factor that multiplies the transmission spectrum. The results in Figure 2.13 indicate that $\Xi_{\mathrm{ext}} < 5\%$ since the only sources of error in the definition are with the film. The spot size of the sample appears slightly smaller than the array when compared by camera and we can limit this error to just a few degrees. This suggests that the largest source of error in regards to the extinction magnitude is most likely the reduction of C_{e} due to the finite N.A., represented by ξ_{Ω}. Because of these considerations we estimate that the upper limit on the error in extinction magnitude is 15%. A summary of the sources of error for extinction measurements is found in Table 2.1.

Table 2.1: A summary of sources of error and estimates of the magnitude.

Source	Symbol	Estimate of Size
Spot size larger than array	ξ_{A}	≈ 1 (negligible)
Finite numerical aperture (N.A.)	ξ_{Ω}	$\lesssim 13\%$
Variation of film properties	$\delta z,\, \delta\alpha \approx 0$	Error in $T \lesssim 3\%$
Instrumental error	ξ_{I}	See text for mitigation techniques.

2.4 Calculations and Simulations

Modeling of the relevant physics was done using three methods. MATLAB® (version 7.10.0) was used for calculations of quasistatic extinction spectra and resonances using Equations (1.1) through (1.9). The MATLAB® software was also used for data analysis, as it is specifically designed to handle large arrays of data efficiently. Appendix A contains a representative script used for the data analysis and modeling.

To calculate the temporal and spatial electromagnetic field distributions, finite difference time domain (FDTD) modeling is a method for solving the differential form of Maxwell's equations using an algorithm developed by Yee in 1966.[118] Lumerical FDTD Solutions® software and Optiwave FDTD® were used for FDTD simulations. The FDTD algorithm was designed strictly to model propagating EM waves. Another technique used for modeling experimental results is a more generalized numerical algorithm called the finite-element (FE) method. This method can be used to solve many second-order differential equations. The FE software, COMSOL Multiphysics®, is designed to allow for coupling between different sets of physics equations. The FE method is especially suited for modeling complex geometries; however, it is not as efficient as FDTD at modeling propagating EM waves. In both cases, the solution

domain and boundaries are discretized into a fine mesh. Errors in the model scale with the mesh size, thus requiring care that the mesh is small enough for a solution to converge. The relationship between convergence and mesh size depends on the algorithm.

2.4.1 Finite Difference Time Domain Method

As the name suggests, the FDTD method is designed to model EM interactions within the time-domain, as opposed to the frequency domain. Fourier analysis is then used to calculate the frequency-dependent response of the geometry. The algorithm interweaves the electric and magnetic components of the differential form of Maxwell's curl equations using a central-difference approximation accurate to second order, then alternates solving the magnetic components and electric components on each half time-step. This provides a self-sufficient and direct way of approximating the solution.[119] Frequency-domain information is done by a Fourier analysis of the solution. White-light extinction calculations can be accomplished by sending a broadband pulse of only a few femtoseconds through the geometry.

To understand the algorithm, we start with Maxwell's curl equations written in component form. The six coupled equations are:

$$\frac{\partial E_{\mathrm{x}}}{\partial t} = \frac{1}{\epsilon}\left(\frac{\partial H_{\mathrm{z}}}{\partial y} - \frac{\partial H_{\mathrm{y}}}{\partial z} - \sigma E_{\mathrm{x}}\right). \tag{2.11}$$

$$\frac{\partial E_{\mathrm{y}}}{\partial t} = \frac{1}{\epsilon}\left(\frac{\partial H_{\mathrm{x}}}{\partial z} - \frac{\partial H_{\mathrm{z}}}{\partial x} - \sigma E_{\mathrm{y}}\right). \tag{2.12}$$

$$\frac{\partial E_{\mathrm{z}}}{\partial t} = \frac{1}{\epsilon}\left(\frac{\partial H_{\mathrm{y}}}{\partial x} - \frac{\partial H_{\mathrm{x}}}{\partial y} - \sigma E_{\mathrm{z}}\right). \tag{2.13}$$

$$\frac{\partial H_{\mathrm{x}}}{\partial t} = \frac{1}{\mu}\left(\frac{\partial E_{\mathrm{y}}}{\partial z} - \frac{\partial E_{\mathrm{z}}}{\partial y} - \rho_{\mathrm{m}} H_{\mathrm{x}}\right), \tag{2.14}$$

$$\frac{\partial H_{\mathrm{y}}}{\partial t} = \frac{1}{\mu}\left(\frac{\partial E_{\mathrm{z}}}{\partial x} - \frac{\partial E_{\mathrm{x}}}{\partial z} - \rho_{\mathrm{m}} H_{\mathrm{y}}\right), \tag{2.15}$$

$$\frac{\partial H_{\mathrm{z}}}{\partial t} = \frac{1}{\mu}\left(\frac{\partial E_{\mathrm{x}}}{\partial y} - \frac{\partial E_{\mathrm{y}}}{\partial x} - \rho_{\mathrm{m}} H_{\mathrm{z}}\right), \tag{2.16}$$

Here, H and E are the magnetic and electric fields, respectively, μ and ϵ are the permeability and permittivities of their respective fields, and σ is the electric conductivity in accordance to Ohm's law. For symmetry and to allow for magnetic losses, a term containing magnetic resistivity ρ_{m} is added to the equations.[119]

Discretizing the modeled volume so that each spacial point (i, j, k) on a lattice corresponds to a physical point $(i\Delta x, j\Delta y, k\Delta z)$, a time dependent function $f(x, y, z, t)$ can now be represented as $f^n = f(i\Delta x, j\Delta y, k\Delta z, n\Delta t)$. Figure 2.14 shows a schematic of the Yee lattice. The magnetic field components are on the faces of the cube, and the electric field components are at each corner. Using this formulation and the resulting centered finite-difference expressions for the derivatives, (2.11) can be written

$$\begin{aligned} E_{\mathrm{z}}^{n+1}\left(i, j, k+\frac{1}{2}\right) = & \\ & = \frac{1 - \frac{\sigma\left(i,j,k+\frac{1}{2}\right)\Delta t}{2\epsilon\left(i,j,k+\frac{1}{2}\right)}}{1 + \frac{\sigma\left(i,j,k+\frac{1}{2}\right)\Delta t}{2\epsilon\left(i,j,k+\frac{1}{2}\right)}} E_{\mathrm{z}}^{n}\left(i, j, k+\frac{1}{2}\right) \\ & + \frac{\Delta t}{\epsilon\left(i, j, k+\frac{1}{2}\right)}\left[1 + \frac{\sigma\left(i, j, k+\frac{1}{2}\right)\Delta t}{2\epsilon\left(i, j, k+\frac{1}{2}\right)}\right]^{-1} F_{\mathrm{H}}, \end{aligned} \tag{2.17}$$

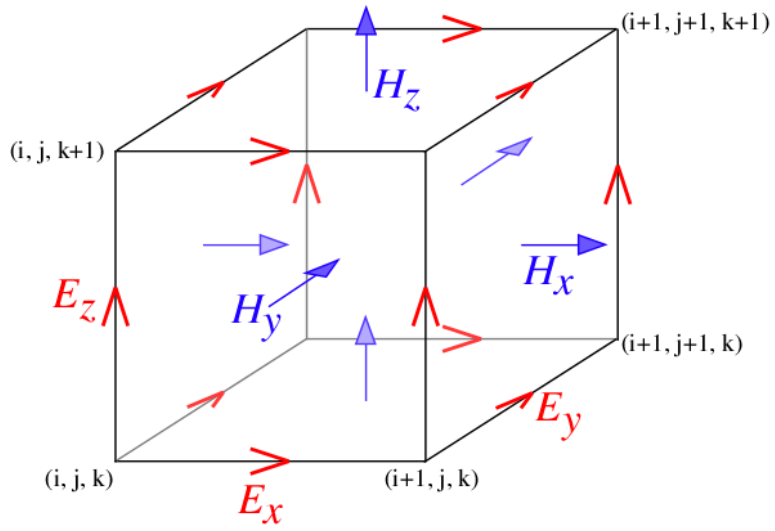

Figure 2.14: The Yee lattice consists of interwoven electric and magnetic field points. The electric field components originate at each corner and point along an edge of the cube. The magnetic field originates from the center of each face. Image used from `http://ab-initio.mit.edu/wiki/index.php/Image:Yee-cube.png`.

where

$$F_{\mathrm{H}} = \frac{H_{\mathrm{y}}^{n+1/2}\left(i+\frac{1}{2},j,k+\frac{1}{2}\right) - H_{\mathrm{y}}^{n+1/2}\left(i-\frac{1}{2},j,k+\frac{1}{2}\right)}{\Delta x} + \frac{H_{\mathrm{x}}^{n+1/2}\left(i,j-\frac{1}{2},k+\frac{1}{2}\right) - H_{\mathrm{x}}^{n+1/2}\left(i,j+\frac{1}{2},k+\frac{1}{2}\right)}{\Delta y}.$$

These and similar expressions for (2.12) through (2.16) are known as the Yee equations.[118,119] In this way, Faraday's and Ampere's laws are solved so that the EM wave propagates throughout the geometry.

The numerical stability of the algorithm is highly dependent on the size of the time-step Δt compared to the mesh-size. This is crucial enough that both Lumerical and Optiwave FDTD solvers set the time-step internally by default to be 99% of the

theoretical value, given by the inequality[119]

$$c_{\max}\Delta t \leq \left(\frac{1}{\Delta x^2} + \frac{1}{\Delta y^2} + \frac{1}{\Delta z^2}\right)^{-1/2}, \tag{2.18}$$

where $c_{\max}$ is maximum EM wave phase velocity in the simulation region.

The mesh size, $(\Delta x, \Delta y, \Delta z)$, is determined by the geometry of interest and the wavelength. For cylindrical NPs, the meshing has to be small enough to resolve the shape; typically,a 2 nm mesh in each direction around the particle is used for the NPs studied in this work. A mesh this size in the whole simulation domain, typically the size of half a wavelength to a full wavelength, would require extensive use of computer resources. However, Lumerical FDTD Solutions® has the ability to select the size of the mesh to be smaller in regions around the particle and larger where the geometry is more uniform. The standard procedure for meshing is to start with a fairly large mesh, run a simulation, and repeat with a smaller mesh. When there are no changes with the decreasing mesh size, then the appropriate size for the model has been found. In practice, with appropriate boundary conditions, one can expect solutions to be highly accurate, within 1 or 2% of analytic theory. Often, experimental uncertainties in the dielectric function data used in the simulation limit the accuracy of the calculation.[120] Figure 2.15 shows a comparison of Mie theory for the absorption and scattering to Lumerical FDTD Solutions® calculations of the same geometry. The figure shows excellent agreement between the exact theory and the numerical calculation.

An inherent source of error in FDTD simulations is a natural dispersion due to the anisotropy of the discretized mesh: Waves traveling along the coordinate axis

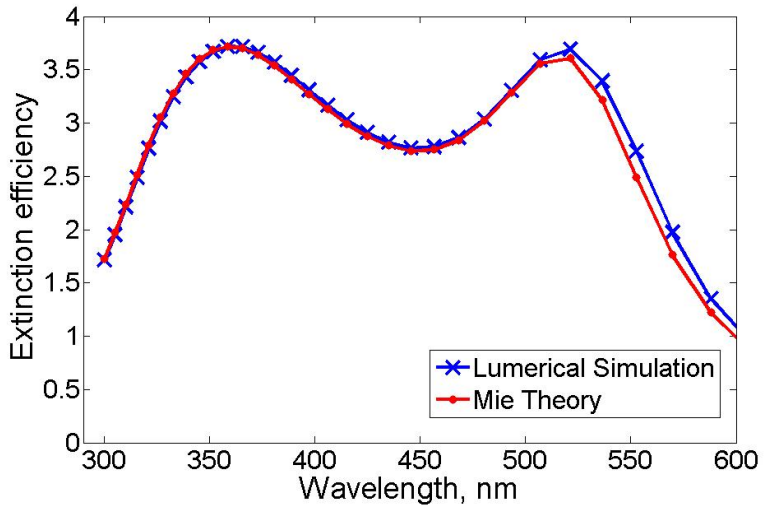

Figure 2.15: A comparison between Lumerical FDTD simulations and Mie theory for a spherical Au NP in air.

(e.g., in the $+x$-direction) travel a shorter distance than waves traveling in an off-angle direction. This highlights the need for using small meshes and performing mesh studies.[119,120] Although Lumerical FDTD Solutions® strictly uses a rectangular mesh, it is possible to implement the algorithm using other coordinate systems in order to reduce this dispersion.[121]

Finally, we discuss boundary conditions (BCs). Lumerical FDTD Solutions® allows for a variety of BCs, such as perfectly conducting, and periodic. Symmetry planes can also be used to reduce the simulation region further. Probably the most complex BCs to use and understand are the perfectly matched layers (PML), designed to absorb the EM wave and minimize reflections from the boundary. The PML BC is used to simulate an infinite space beyond the simulation domain. For this reason, they must be thick enough to absorb all of the incident radiation. In Lumerical, any

medium that is in contact with the PML boundary must go all the way through the PML layers. Otherwise, reflections are increased at the interface.[120]

Figure 2.16 shows extinction calculations and measurements normalized to the maximum for 140 nm diameter Au NPs on an ITO-coated substrate in air, 20 nm in height, and a grating constant of 500 μm. The quasistatic dipole approximation without size effects, (1.4), predicts the peak wavelength the best; however, the predicted width of the resonance is more narrow than experiment. Including size effects in the dipole model, (1.11), leads to a predicted LSPR that is redshifted by tens of nanometers and much wider than experiment. The full electrodynamical FDTD simulations produced by Lumerical FDTD Solutions® was blueshifted and much more narrow than the experiment. Overall, the peak position of the LSPR as calculated by each method is within 50 nm of the experiment.

2.4.2 Finite Element Method

The finite element (FE) method can be used to solve a variety of partial differential (PDE) and integral equations.[122] The method can be summarized into two steps. First, the PDE is transformed into its weak, or variational, form that can be shown to have an equivalent and unique solution to the strong form of the problem. The weak form is an integral equation. Second, the infinite set of functions that satisfy the boundary conditions (BC) for both the weak and strong forms are approximated by a finite set of functions. How these functions are chosen and by which numerical technique the solution is found is the subject of many textbooks and courses.[122] COMSOL Multiphysics® offers only limited documentation concerning the details of

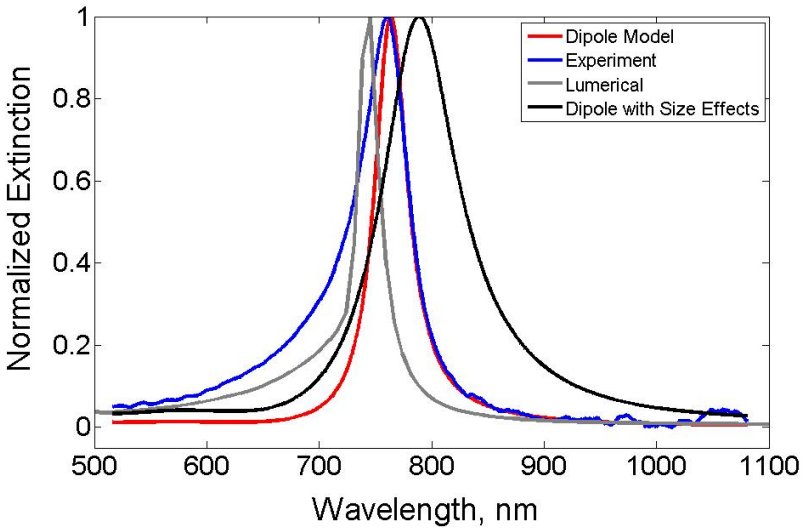

Figure 2.16: A comparison between Lumerical FDTD simulations and MATLAB quasistatic dipole calculations to experiment for 140 nm NPs on ITO-coated glass in air with a grating constant of 500 μm.

its solvers. In this section, a detailed description of the simulations of the experiment described in Chapter V is presented. The focus is on relevant modeling settings and physics assumptions used in the program and not on the FE technique itself.

For the analysis of Chapter V results, the temperature distribution of the film is important in understanding the thermodynamics of laser heating. To calculate this, COMSOL's Heat Transfer Module was used to solve the 2D axisymmetric heat equation in cylindrical coordinates,

$$\frac{\partial T(r,z,t)}{\partial t} - \alpha \nabla^2 T(r,z,t) = Q(r,z,t), \tag{2.19}$$

where T is the temperature, $\alpha = \kappa / C_p \rho$ is the thermal diffusivity, κ is the thermal conductivity, C_p is the specific heat capacity at constant pressure, ρ is the mass

density, and Q is the heat generated per unit volume per unit time (W/m^3).[122,123]

The simulation region was defined by the boundaries $r = (0, 2.0)$ mm and $z = (-0.55, 60 \times 10^{-6})$ mm. A thin film of VO_2 was simulated at $0 < z < 60 \times 10^{-6}$ mm. Glass was used for $z < 0$. Laser irradiation was modeled as heat generated in the region of the VO_2 approximately coinciding with the dimensions of the beam spot; a Gaussian intensity profile was used. No heat is generated in the glass. The triangular meshing was 20 nm in side-length in the VO_2 and expanded in the glass as z decreased. Figure 2.17 shows the simulation geometry and mesh. The $z = -55$ mm boundary is set to a constant temperature of $T = 55°C$ since that is the temperature of the Cu mount in the experiment. The $r = 0$ boundary is axially symmetric. The remaining two boundaries are insulating with zero heat flux crossing the boundary ($\nabla T = 0$). Simulations performed using radiative or convective heat loss at the boundary showed no change in temperature from the insulating case. The physical parameters used in the simulation are listed in Table 5.2. The solver used was the default MUltifrontal Massively Parallel sparse direct Solver (MUMPS). Mesh studies performed in conjunction with this model show that the a "very fine" mesh was not necessary. The mesh shown in Figure 2.18 produced results identical to those produced with the mesh shown in Figure fig:FEmesh(b) within 0.2%.

Further details and the results of the FE simulations will be presented in Chapter V.

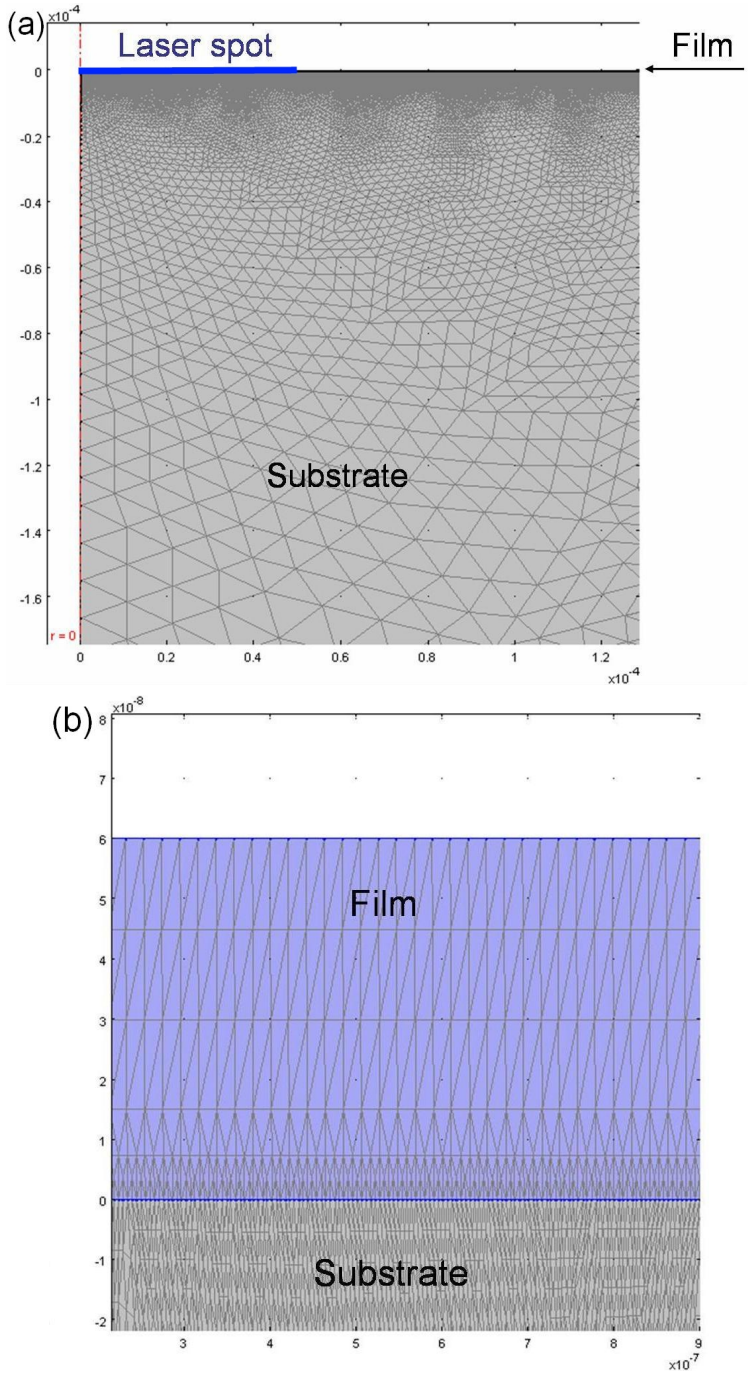

Figure 2.17: (a) The geometry simulated using COMSOL Multiphysics® for the laser heating experiments reported in Chapter V. The mesh starts at 20 nm in the VO_2 film and expands as z decreases. The blue line corresponds to a laser spot of 50 nm in radius. (b) An enlarged view showing the mesh in the film. The axes are in meters.

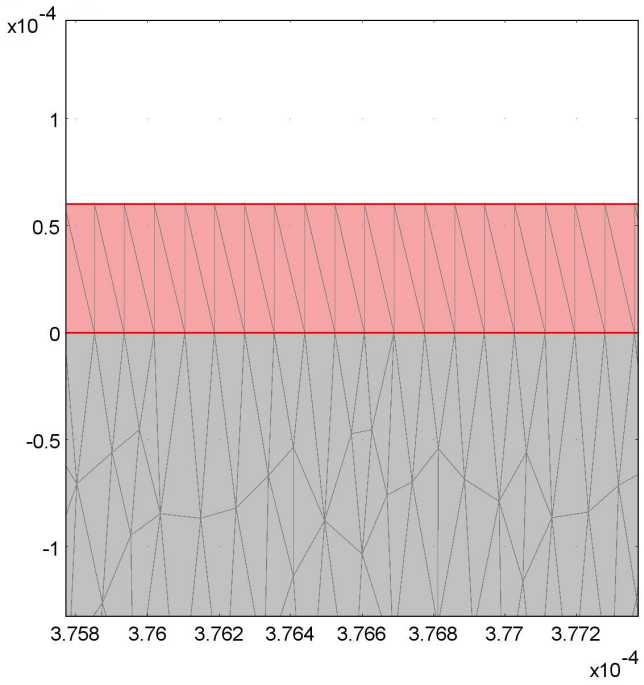

Figure 2.18: An enlarged view showing the mesh in the film showing a less refined mesh than Figure 2.17. The axes are in meters. Figure courtesy of Evan R. MacQuarrie.

CHAPTER III

NANOANTENNAS: PROBING THE PHASE TRANSITION

Abstract

The localized surface-plasmon resonance (LSPR) frequency of metal nanoparticle (NP) arrays depends on the local dielectric response of the surrounding material. The semiconductor-to-metal phase transition (SMT) in VO_2 shifts the LSPR in arrays of gold NPs. Previous studies have focused on the modulation of the LSPR and potential applications, such as optical switches. In this study, we used lithographically prepared arrays of 100- and 180-nm diameter NPs to study the interaction between the particle and film during the phase transition. We show that the particles act as nanoantennas, providing information about the changing VO_2 dielectric function through a shift in LSPR and changes to the width of the resonance at energies above the 0.7 eV bandgap of semiconducting VO_2. The LSPR dephasing time for the 180 nm NPs decreased by 30% as a result of increase damping due to the split $d_{||}$ bands coming together during the phase transition to form the conduction band of the metallic VO_2.

3.1 Introduction

The improvement of fabrication techniques makes it possible to create metal nanostructures with high precision on sub-100 nm scales. These structures demonstrate a high level of optical tunability by manipulation of their shape and surrounding medium; however, the geometry is typically static once fabricated. This limits the ability to implement real-time optical tunability and switching. The localized surface-plasmon resonance (LSPR) frequency of metal nanoparticle (NP) arrays depends on the local dielectric response of the surrounding material. We can therefore modulate the LSPR if the metal nanostructure is embedded in a material that exhibits strong

changes to its dielectric function when exposed to a particular stimulus, such as heat, irradiation, stress, or an electric field. The semiconductor-to-metal phase transition (SMT) in VO_2 provides such an ability to shift the LSPR in arrays of gold NPs.[17]

As discussed in Section 1.1, most experimental studies of Au::VO_2 geometries have focused on demonstrating the tunability of the composite structure by shifting the LSPR using the SMT. Studies at optical wavelengths have not taken advantage of ordered arrays of Au NPs; rather they have used mostly Au island films (Figure 1.12) and other non-ordered geometries.[12–16] The major advantage of lithographically prepared arrays of NPs is the precise control over the NP shape, size, and position relative to other particles. The well-characterized geometry also reduces the complexity of modeling the LSPR.

In this study, the array geometry was used to isolate the plasmonic response of the Au NPs and monitor the LSPR as the VO_2 undergoes the SMT. Plasmonic extinction (Figure 3.2) and hysteresis (Figure 3.3) measurements of the Au::VO_2 structure were conducted at increments of approximately 1°C during the transition. The plasmonic hysteresis, characterized by a change in LSPR wavelength and width as a function of temperature, provides a novel means of probing the VO_2 phase transition in the region of interband absorption. Since the Au NPs are on the order of the VO_2 grain size (Figure 2.4), they are sensitive *nanoantennas* to the changes in the VO_2 effective medium. We investigate the sensitivity of these nanoantennas to changes in the VO_2 dielectric function and the damping of the Au plasmon for particle diameters of 100 nm and 180 nm. The results show that the LSPR wavelength varies linearly with the metallic fraction f of the VO_2 domains. The dephasing time for the 180 nm NPs

decreases by 30% during the phase transition due to the sensitivity of the LSPR to the interband transitions of the VO_2. The implications of these findings for applications are discussed.

3.2 Experimental Details

On a single substrate, arrays of 180 nm and 100 nm diameter particles, each 20 nm in height, were fabricated by electron beam lithography (EBL). One array of each particle diameter measured 500 μm in length on a side with a grating constant of 450 nm. This array size provided large areas to take hysteresis measurements. A series of 100 μm by 100 μm arrays, with grating constants varying from 300 nm to 450 nm for each particle diameter was also fabricated to measure grating constant effects on the LSPR shift caused by the SMT. A 60 nm film of VO_2 was deposited on the arrays. The thickness of the VO_2 was calibrated by profilometric measurements on a witness substrate prior to the deposition. Scanning electron microscopy (SEM) images of the sample are shown in Figures 2.4 and 3.1.

Optical transmission hysteresis measurements were made on and off the arrays to test the effect of the Au NPs on the switching behavior of VO_2 and the consistency of the film (Figure 2.7). From these measurements, we conclude that the presence of the Au did not affect the properties of the SMT in the hybrid structure. The contrast between the semiconducting and metallic states, defined as the temperature-dependent transmission normalized to the initial transmission, and shown in Figure 2.7, is 10% less on the array than the contrast off the the array because of a reduction in the overall transmission due to NP extinction.

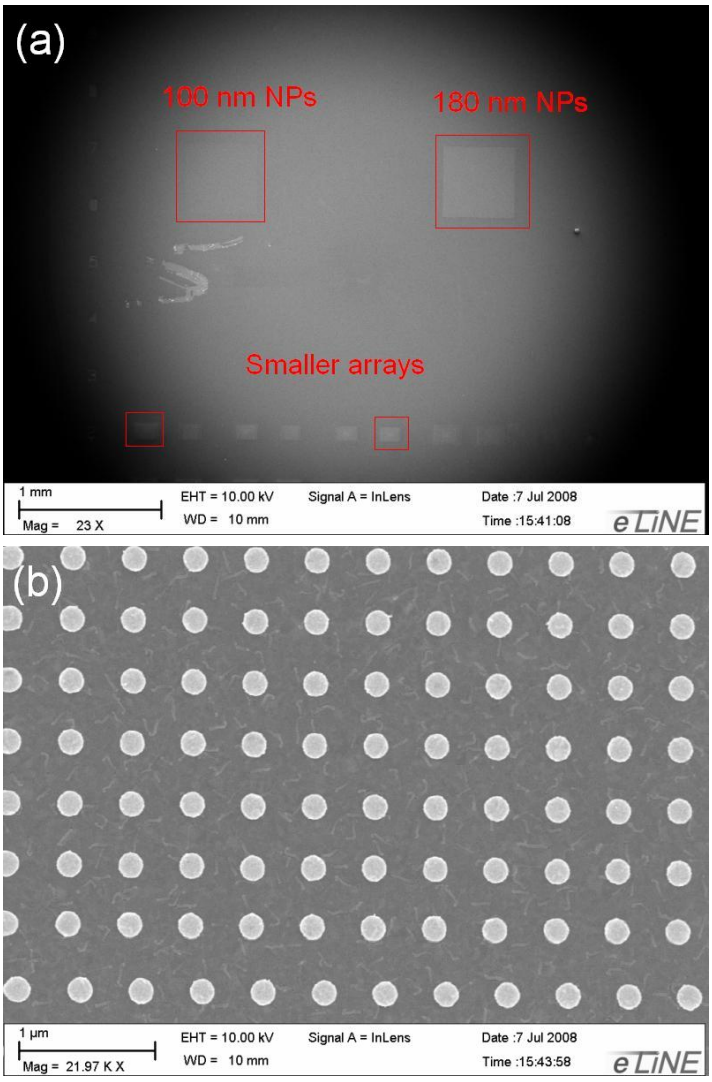

Figure 3.1: SEM images of arrays used in nanoantenna study, including (a) a plan view and (b) a magnified image of the 180 nm array with 450 nm grating constant.

Extinction measurements, shown in Figure 3.2, were performed as discussed in Sections 2.2.2 and 2.3.2. For the plasmonic hysteresis measurements, the temperature T of the sample was slowly increased and a flat-field (reference) spectrum (Figure 2.12) was taken off the array on plain VO_2 film. An extinction spectrum was then immediately taken on the array to minimize variation in temperature. For each spectrum taken, both flat-field and extinction temperatures were averaged in the analysis to the tenth of the degree. As noted in Section 2.2.2, the limits of error for the thermocouple used in the measurement were $\pm 2.2^{\circ}$C or 0.75%.

3.3 Results and Discussion

Figure 3.2 shows selected temperature-dependent spectra of the 500 μm arrays taken during the phase transition. As the film switches to the higher temperature state and returns to the cooler state, the LSPR position and width are nearly identical at the same position of the sigmoid curve when the offset in temperature is taken into account. During the phase transition there is a noticeable widening of the LSPR for the 180 nm particles. The 100 nm particles, shown in Figure 3.6, do not undergo the same increase in LSPR width. Section 3.3.1.2 discusses the significance of this phenomenon and Section 3.4 includes a discussion of the structure of these spectra.

The blueshift of the LSPR in the metallic state relative to the semiconducting state is easily explained by considering Equations (1.4) and (1.6). Using the Drude

model and working at frequencies far below ω_p, we can write

$$\begin{aligned}\epsilon' &= 1 - \frac{\omega_p^2 \tau^2}{1 + \omega^2 \tau^2} \\ &\approx 1 - \frac{\omega_p^2}{\omega^2} \\ &= 1 - \frac{\lambda^2}{\lambda_p^2},\end{aligned} \tag{3.1}$$

where the prime ($'$) denotes the real component of the complex number, $\gamma = 1/\tau$ is the collision frequency, and λ_{p} is the plasma wavelength. Therefore, the LSPR wavelength λ_{LSPR} is approximately given by

$$\lambda_{\mathrm{LSPR}} = \lambda_{\mathrm{p}} \sqrt{1 + (1 - \frac{1}{L})\epsilon'_{\mathrm{m}}}. \tag{3.2}$$

From Figure 1.14, we can see that ϵ'_{m} for the metallic state of VO_2 is less than that of the semiconducting state for all frequencies in the visible part of the spectrum. Therefore, upon switching, according to (3.2), we expect a blueshift of λ_{LSPR}.

3.3.1 Plasmonic Hysteresis

We now discuss the way in which the Au NPs probe the changes in ϵ_{m} as the VO_2 undergoes the SMT. To our knowledge, this is the first use of Au NPs as a probe to monitor the phase transition. It will be shown (Figure 3.4) that the wavelength of the LSPR is linearly dependent on the metallic fraction $f(T)$ of VO_2 switched; indeed, the linear model produces better fits than either the Bruggemann or Maxwell-Garnett effective medium theories. Furthermore, the changes in the width of the resonance

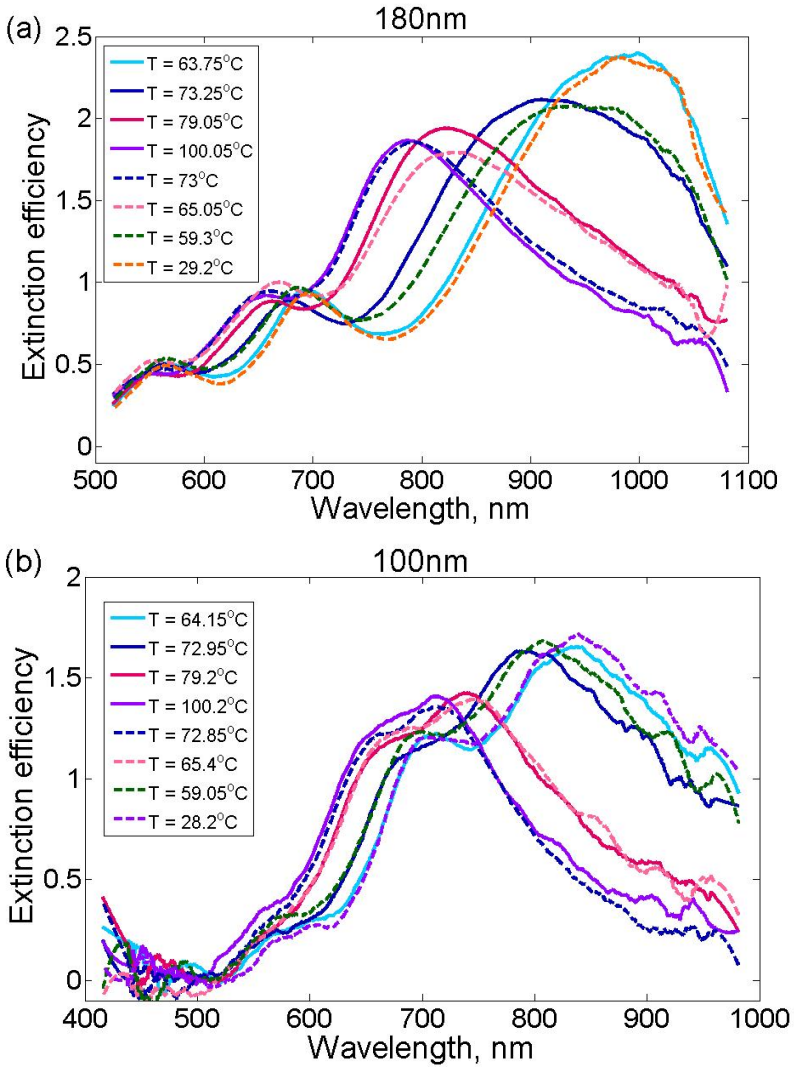

Figure 3.2: Selected extinction efficiency spectra for the (a) 180 nm and (b) 100 nm diameter particles during the VO_2 SMT for the 500 μm square array with grating constant 450 nm. Note that the x-axes each have different scales to roughly center each LSPR peak.

can be associated with particular changes in the band-structure of VO_2.

3.3.1.1 Temperature Dependence of the LSPR Wavelength

Figure 3.3 shows the LSPR wavelength as a function of temperature for both the 180 nm and 100 nm particle arrays. As expected, there is a hysteresis in the curve indicative of the first-order phase transition centered around a transition temperature of 68°C. Following standard practice, the hysteresis is fitted with a four-parameter sigmoid given by

$$\lambda_{\mathrm{LSPR}}(T) = \lambda_{\mathrm{LSPR}}^{\mathrm{semi}} - \frac{\lambda_{\mathrm{LSPR}}^{\mathrm{semi}} - \lambda_{\mathrm{LSPR}}^{\mathrm{met}}}{1 + e^{-\frac{T - T_{\mathrm{c}}}{T_{\mathrm{w}}}}}, \tag{3.3}$$

where $\lambda_{\mathrm{LSPR}}^{\mathrm{semi}}$ and $\lambda_{\mathrm{LSPR}}^{\mathrm{met}}$ are the LSPR wavelengths for VO_2 in the semiconducting and metallic states, respectively, and T_{c} and T_{w} are the critical temperature (72°C and 64°C, respectively) and a transition width (2.75°C) for the cooling or heating curves. These fit parameters are nearly identical to the transmission hysteresis corresponding to Figure 2.7. The error bars in Figure 3.3 represent the standard deviation of the LSPR measurements below 45°C (±10.6 nm); the same method is used for all other error bars in this chapter.

Since the LSPR is sensitive to the *local* dielectric of the embedding medium, the plasmonic hysteresis can offer distinct information about the VO_2 domains in the near vicinity of the Au NPs. The fact that the plasmonic hysteresis fit parameters are the same as the transmission hysteresis is significant, as it suggests that the change in switching temperature found by Xu *et al.* for Au::VO_2 structures consisting of island films is not present in our structures.[15] This is not a surprising result, as Xu *et al.*

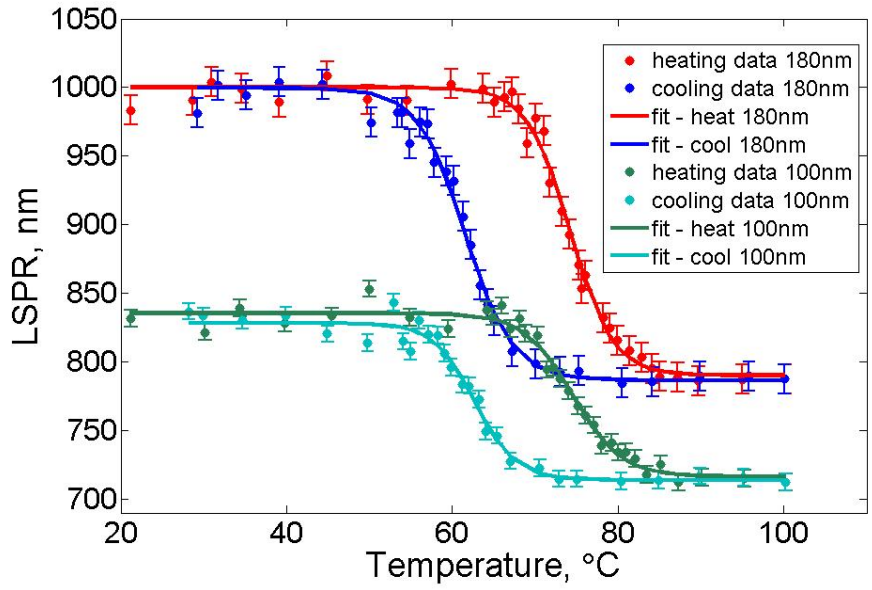

Figure 3.3: The hysteresis of the LSPR as VO_2 undergoes its phase transition from semiconducting to metallic states for both the large 180 nm and 100 nm particle arrays fitted by Equation 3.3.

measured the change in Au::VO_2 nanojunctions. That is, both the Au and VO_2 were discontinuous island films. For the Au::VO_2 structures studied here, the volumetric fraction of Au to VO_2 for the 180 nm particles was approximately 4.2% and would not lead to significant increase the carrier concentration in the film. If electron injection affected only the VO_2 grains around the Au NPs, a change in switching temperature might not have been detectable in the optical transmission measurements; however, the plasmonic hysteresis rules out a local effect as well. This result also excludes electron injection as a mechanism for the reduced critical laser power necessary for switching the Au::VO_2 structures described in Chapter V.

The change in ϵ'_m is the primary mechanism for blueshifting the LSPR by 140 nm

to nearly 260 nm depending on the NP size and grating constant (Figure 3.12c). Therefore, the change in LSPR provides a way to monitor the change in ϵ'_{m}. Using (1.6), the dielectric function for Au reported in [64], and assuming that the effective medium is an average between the dielectric function of ITO ($\epsilon_{\mathrm{ITO}} = 3.2$) and VO_2, the values of the real part of the dielectric function of VO_2 can be estimated. The factor $\kappa \equiv 1 - L^{-1}$ from (1.6) is -12.4 and -7.02 for the 180 nm and 100 nm diameter particles, respectively. Physically, κ determines the shift in LSPR wavelength due to changes in particle shape. In the semiconducting state, $\epsilon'_{\mathrm{semi}} \approx 4.1$, where we have averaged the estimated values at wavelengths 1000 and 840 nm, which are the values of the LSPR in the semiconducting state for the 180 and 100 nm particles, respectively. This is less than half the value of $\epsilon'_{\mathrm{semi}} = 8.6$ at $\lambda = 920$ nm as measured by Verleur, and shown in Figure 1.14.[38] For the metallic state, by the same method, $\epsilon'_{\mathrm{met}} \approx 1.1$, compared to the $\epsilon'_{\mathrm{semi}} = 4.2$ value as measured by Verleur at 750 nm. Our VO_2 samples exhibit a reduced dielectric function compared to the Verleur samples. The reasons for this reduction are still not completely understood, but are consistent with preliminary results from ellipsometry measurements (Figure 6.2) performed on semiconducting VO_2.

As is done in [88], the metallic fraction f can be calculated using the fit parameters T_{c} and T_{w} from

$$f(T) = 1 - \frac{1}{1 + \exp\left[\frac{T - T_{\mathrm{c}}}{T_{\mathrm{w}}}\right]}. \tag{3.4}$$

Figure 3.4 shows that the position of the LSPR wavelength changes linearly with f. Fitting the data gives slopes M of -208 and -119 for the 180 and 100 nm particles.

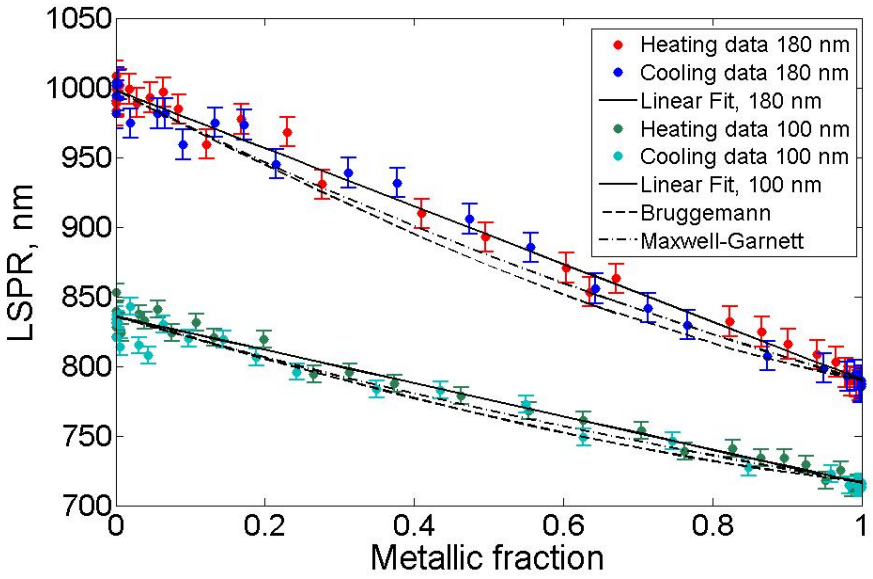

Figure 3.4: Plotting the LSPR versus metallic fraction using the fit parameters of the hysteresis and (2.1) to calculate f shows a linear relationship.

The ratio of the two slopes $\gamma = -208/-119 = 1.74$, corresponding well to the ratio of κ values $-12.4/-7.02 = 1.76$. This correspondence shows that the sensitivity of the LSPR to changes in the VO_2 effective medium can be increased proportionally to κ. The ratio M/κ of each curve is a common factor of approximately 16.9. This can be used to estimate the shift in resonance for particles of different shapes. For example, spherical particles have $\kappa = -2$ with a predicted shift in resonance of approximately 34 nm. For oblate spheroidal NPs with a height of 20 nm, increasing the diameter increases κ linearly, and thus increases the shift in resonance. For 200 nm particles, we expect $\kappa = -13.4$ and a shift in resonance of 226 nm, assuming the multiplicative factor of 16.9 holds. Figure 3.5 shows the predicted shift in LSPR as a function of geometrical factor L.

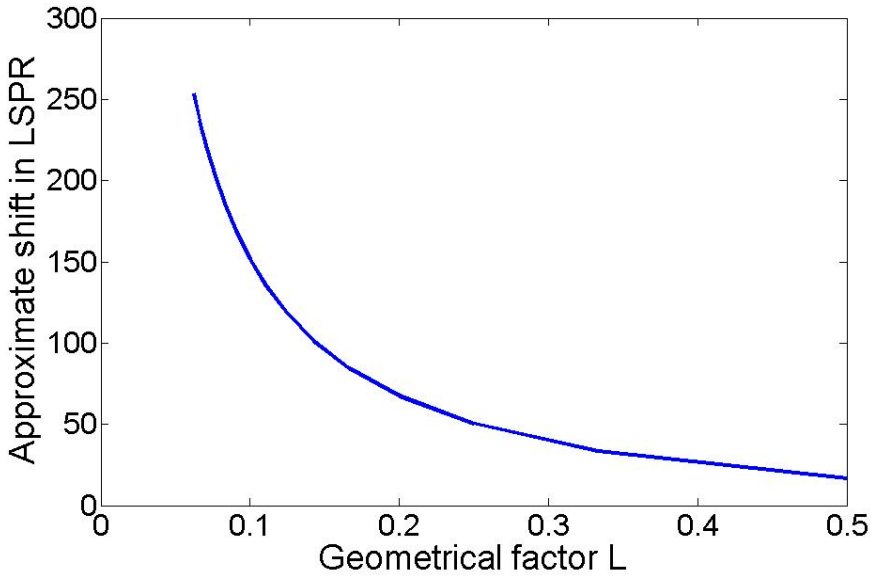

Figure 3.5: Using the linear relationship between LSPR and κ, the approximate shift in LSPR as a function of geometrical factor L is shown.

Typically in VO_2 studies, such as in [88], the medium is modeled using either Bruggeman (BR) or Maxwell-Garnett (MG) effective medium theories, both of which have a non-linear dependence on f. To compare effective medium theories, the predicted effective dielectric constant as a function of f is plotted in Figure 3.4. The linear fit was performed in two ways with identical results. In the first, the entire data set was fitted to a line. Secondly, only the semiconducting and metallic LSPR wavelengths were used to define the line. This was done because the error in the static, or fixed temperature, spectra is at a minimum compared to the spectra taken during the phase transition. To compare the linear case to the BR and MG models, this latter method of fitting the endpoints was employed. From this fit, it appears that the BR and MG models consistently underestimate the LSPR wavelength during the

transition. This suggests that for NP plasmon modeling, the linear model should be used for probing changes in the effective dielectric function for VO_2. Furthermore, the relative agreement between the linear, BR, and MG effective medium models suggests that the Au LSPR wavelength is not sensitive to the specific arrangement of metallic inclusions of VO_2 as the film transitions, but only in the average dielectric response of the film.[44] In other words, the VO_2 can be treated as a homogeneous medium for purposes of modeling plasmonic behavior, and the shift in LSPR wavelength is not sensitive to the percolative nature of the phase transition.

3.3.1.2 Temperature Dependence of the LSPR Width

In addition to the LSPR wavelength, we can also measure the width of the resonance during the phase transition, as shown in Figure 3.6a and b. We have measured the full width at 90% of the maximum (FW90M) Γ_{90} instead of the typical full width at half max (FWHM) Γ_{50} because of the multiple resonances present in the spectra and the complex shape of the large dipolar resonance. Both arrays showed a decrease in width in the final metallic state relative to the semiconducting state. The 100 nm particles underwent this decrease in a gradual manner; however, the 180 nm particles exhibited a spike in width approximately 1°C below T_c on both the heating and cooling curves before decreasing in width as the VO_2 shifts more fully into the metallic state.

In general, the width of the LSPR is due to a combination of inhomogeneous (extrinsic) and homogeneous (intrinsic) broadening. That is, $\Gamma_{50} = \Gamma + \Gamma_I$, where Γ and Γ_I are the homogeneous and inhomogeneous contributions to the LSPR width.

The inhomogeneous width is due to variations in the resonance of the ensemble of particles within a geometry. These variations can be caused by differences in particle size, shape (κ), and nearest neighbor distances.[5,44,124] We can also expect inhomogeneous broadening if the particles are embedded in a medium that exhibits variations in its dielectric function over the area of the array. Since the phase transition of VO_2 occurs through percolation,[99] and the grain size of the VO_2 is of the same order as the NPs (approximately 50 to 120 nm), as seen in Figure 2.4, it is reasonable to ask whether there is any evidence of additional inhomogeneous broadening during the phase transition. We would expect this additional broadening to be greatest at T_c, when the film is expected to have maximum fluctuations in the VO_2 state. Although the LSPR width for the 180 nm particles can be seen as evidence of inhomogeneous broadening, the absence of a spike in the 100 nm particles strongly suggests that the broadening seen in the 180 nm array is homogeneous in nature. However, the 100 nm resonances are already broad and the spectra complex in shape. This leads to noisy variations in the FW90M of the 100 nm particles making it difficult to draw conclusions about changes in the LSPR width for these particles.

The homogeneous width Γ, is related to the *plasmon dephasing time* τ_2 by $\Gamma = 2\hbar/\tau_2$ and is a measure of the damping mechanisms where the electronic excitation is dissipated into thermal energy.[125] For particles small compared to the wavelength, non-radiative damping of the plasmon oscillation occurs predominantly through inelastic scattering between the excited free-electrons and the Au lattice, other electrons, and the interface. This scattering result in the decay of the plasmon to the ground state over a period of time τ_1. The plasmon dephasing time and the pop-

ulation decay time are related by $\tau_2 = 2\tau_1$. The imaginary part of the dielectric function phenomenologically quantifies the damping due to the material.[44] For larger particles, radiative damping $\tau_{2,\mathrm{rad}}^{-1}$ can also occur and depends

$$\tau_{2,\mathrm{rad}}^{-1} \sim \frac{(\epsilon_{\mathrm{m}}')^{3/2} V}{\lambda_0^3}, \tag{3.5}$$

where λ_0 is the vacuum wavelength. For the 180 nm NPs, this ratio is on the order of 10^{-3}. On the other hand, the imaginary parts of ϵ and ϵ_{m} are both greater than 1, indicating that non-radiative damping is the primary dephasing mechanism in this case. We will therefore focus our analysis on the homogeneous width and dephasing time.

Physically, near the LSPR wavelength, $\Gamma_{50}(T)$ depends on the imaginary part of the denominator of the polarizability. Since the real part of the dielectric function of Au ϵ is approximately a factor of 10 larger than the imaginary parts of ϵ or ϵ_{m} and changes rapidly in the NIR, the width of the nearly Lorentzian resonance (Figure 3.6c) has an approximately linear dependence on the imaginary dielectric functions of Au and VO_2, ϵ'' and ϵ_{m}''. From (1.4),

$$\Gamma_{50} \propto \epsilon_{\mathrm{m}}'' + L\left(\epsilon'' - \epsilon_{\mathrm{m}}''\right). \tag{3.6}$$

For the NPs in this study, L is 0.07 and 0.12 for the 180 nm and 100 nm NPs; we therefore ignore the relatively small second term in (3.6). Accounting for the effective

medium and SMT, Γ_{50} can be modeled as

$$\Gamma_{50}\left(\lambda_{\mathrm{LSPR}}, T\right) = a_1\left[1 - f\left(T\right)\right]\epsilon''_{\mathrm{semi}}\left(\lambda_{\mathrm{LSPR}}\right) + a_2 f\left(T\right)\epsilon''_{\mathrm{met}}\left(\lambda_{\mathrm{LSPR}}\right), \tag{3.7}$$

where the LSPR wavelength λ_{LSPR} is a functional of $f(T)$, and the subscripts "semi" and "met" indicate the VO_2 state. Simplifying, (3.7) can be written as

$$\Gamma_{50} = a_1\epsilon''_{\mathrm{semi}} - \frac{a_2\epsilon''_{rmmet} - a_1\epsilon''_{rmsemi}}{1 + exp\left(\frac{T - T_{\mathrm{c}}}{T_{\mathrm{w}}}\right)}, \tag{3.8}$$

similar to the sigmoid of (3.3).

The sigmoidal shape of (3.8) is made more complicated by $\epsilon''_{\mathrm{semi}}$ and $\epsilon''_{\mathrm{met}}$ both being functionals of $\lambda_{\mathrm{LSPR}}(T)$. During the SMT and on the time scale of the Au plasma excitations, the effective dielectric function of the medium slowly changes from semiconducting to metallic. As described in Section 1.4.2, the Lorentzian oscillator with energy of 1.4 eV begins redshifting in resonance and increasing in amplitude. Simultaneously, the LSPR of the Au NPs begins blueshifting. We can therefore expect a maximum or minimum in $\Gamma_{50}(T)$. Since the structure of the dielectric function can be modeled as Lorentzians, we model this critical point as such. The changes in Γ_{90} were fitted with a sigmoid function plus a Lorentzian, given by

$$\Gamma_{90} = \Gamma_{\mathrm{max}} - \frac{\Gamma_{\mathrm{min}} - \Gamma_{\mathrm{min}}}{1 + e^{-\frac{T - T_0}{b}}} + \frac{A}{\left(T - T_1\right)^2 + \left(\frac{c}{2}\right)^2}, \tag{3.9}$$

where Γ_{max}, Γ_{min}, and T_0 are the previously described sigmoid fit parameters, A is the amplitude of the Lorentzian, T_1 is the position of its peak, and c is the FWHM

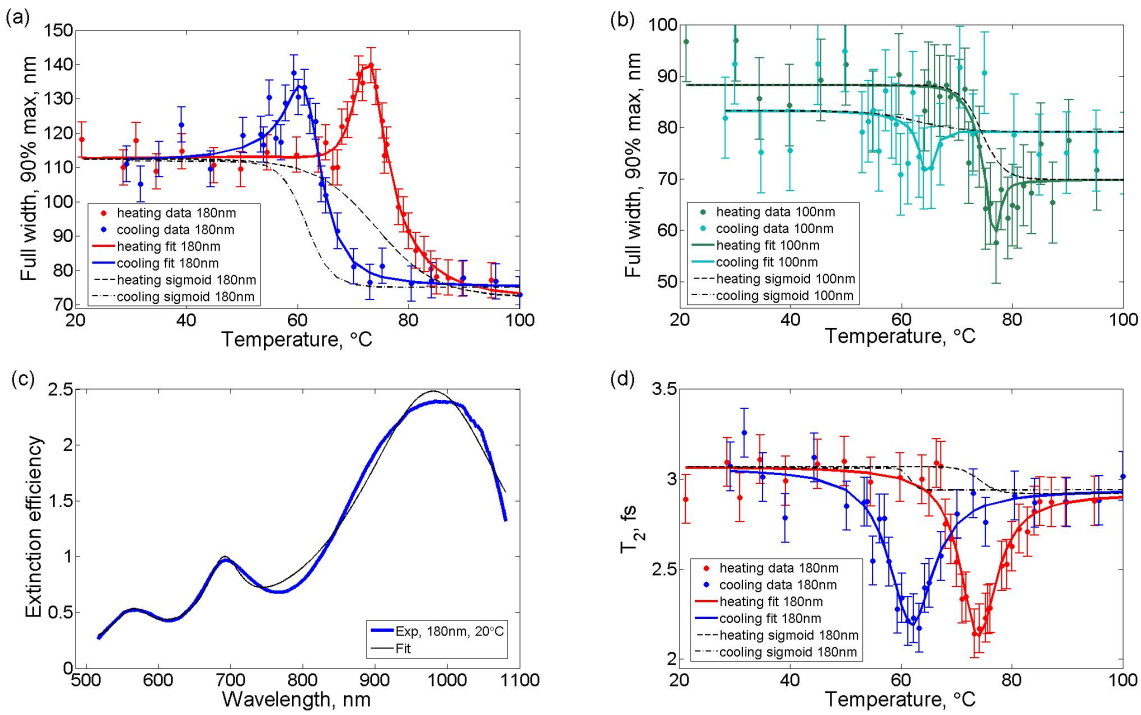

Figure 3.6: The hysteresis of the LSPR width measured from extinction spectra as VO_2 undergoes phase transition from semiconducting to metallic states for the (a) 180 nm and (b) 100 nm particle arrays fitted with a sigmoid plus a Lorentzian. (c) The LSPR for room temperature 180 nm arrays fitted with a sum of three Lorentzian functions. (d) The LSP dephasing time calculated from the resonance width and fitted with Lorentzian functions.

of the Lorentzian contribution. The value of T_0 was determined by LSPR wavelength hysteresis and not used as a fit parameter. The value of the fit parameters are recorded in Table 3.1.

Assuming the resonances are Lorentzian (Figure 3.6c), then $\Gamma = 3\Gamma_{90}$, and τ_2 can be calculated from the data. Figure 3.6d shows the thermal hysteresis of τ_2 fitted using (3.9). In the semiconducting state, $\tau_2 \approx 3 \pm 0.14$ fs. The average FWHM of the two Lorentzian functions characterizing the decrease in dephasing time is 8.8°C with the minimum dephasing time of approximately 2.15 fs occurring at 61.5°C and

Table 3.1: The values of the fit as described by (3.9) corresponding to the data in Figure 3.6 for Γ_{90} and τ_2; T_0 was determined from the LSPR wavelength hysteresis and not used as a fit parameter.

	T_0	$\Gamma_{\max}$	$\Gamma_{\min}$	b	A	T_1	c
Heating							
180 nm, Γ_{90}	74.2	113	72.3	5.4	567	72.8	7.0
100 nm, Γ_{90}	74.5	88.3	69.9	1.9	-30	76.6	2.7
180 nm, τ_2	74.2	3.1	2.9	1.6	-13.7	73.8	7.9
Cooling							
180 nm, Γ_{90}	61.6	112	75.2	2.3	600	61.4	7.9
100 nm, Γ_{90}	62.7	83.3	79.2	4	-20.1	64.6	2.7
180 nm, τ_2	61.6	2.9	3.1	-0.68	-18.6	61.5	9.6

74.8°C for the cooling and heating curves respectively. These temperatures are slightly below T_c for each curve, corresponding to the temperature and interband transition energies associated with the lowering of the split $3d_{||}$ bands. Modeling described in Section 3.3.2 shows that the increase in LSPR width (and thus the decrease in τ_2) can be attributed to the increase in ϵ''_m that occurs as a result of free-electron scattering in the conduction band of metallic VO_2.

The LSPR of the 100 nm particles switches from approximately 830 nm (1.5 eV) in the low temperature state to 715 nm (1.7 eV) in the high temperature state. The LSPR of the 180 nm particles shift from 1000 nm (1.2 eV) to 788 nm (1.6 eV). Therefore, there is some overlap in the wavelengths involved in the transition. Figure 3.7 shows the FW90M plotted versus LSPR wavelength during the transition; the minimum LSPR width occurs at approximately 750 nm, or 1.65 eV. This corresponds to the "valley" between the 1.4 eV and 3.5 eV oscillators used to describe semiconducting VO_2 in Figure 1.14 and Table 1.2 and the increase on either side of this minimum

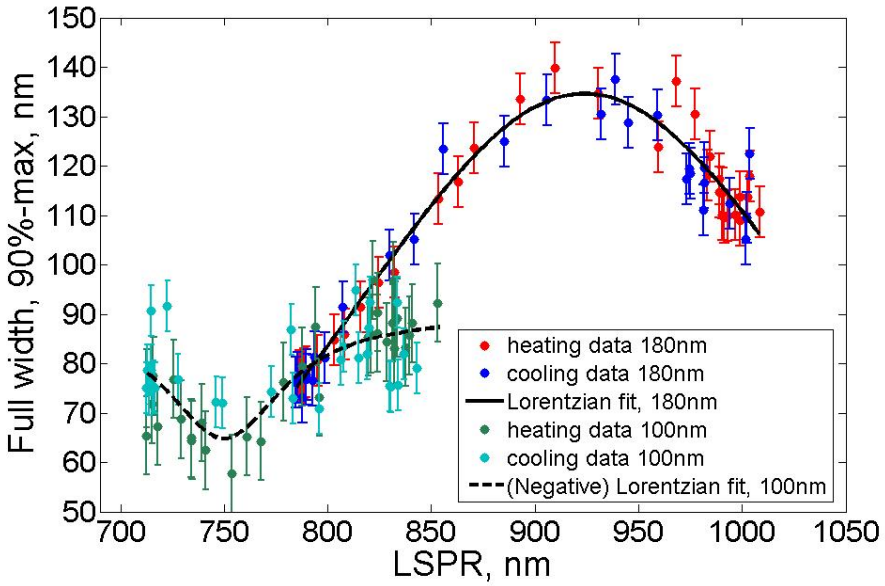

Figure 3.7: The LSPR width for both the 100 nm and 180 nm arrays plotted as a function of LSPR wavelength and fitted with Gaussian functions.

is correlated with the oscillators decribing the interband transitions. Note that we do not expect perfect overlap in the 100 nm and 180 nm widths versus LSPR wavelength since (3.6) is only a rough approximation. The width also depends on L and $\epsilon(\lambda)$.

Correlating these data to the electronic excitations of the VO_2 explains the features seen in Figures 3.6 and 3.7. The initial LSPR for the 100 nm particles is located at 1.5 eV corresponding to the region of transitions within the $3d_{||}$ bands. As the VO_2 undergoes the transition, the split upper V $3d_{||}$ and $3d_{\pi}$ bands move toward the Fermi level and the lower V $3d_{||}$ band. These bands come together and form the metallic conduction band. This increases the imaginary component of the dielectric function of VO_2 as energy is now lost due to free-electron scattering in the metallic VO_2. Kakiuchida *et al.* modeled change in $3d_{||}$ band energy as a redshifting Lorentz

oscillator in [101], as discussed in Section 1.4.2. As the LSPR blueshifts towards 1.7 eV ($\lambda = 729$ nm), the 1.4 eV-oscillator energy redshifts, approaching zero in resonance energy. In other words, the restoring force of the Lorentz oscillator approaches zero, and the oscillator then describes the Drude free-electron gas. The LSPR is then resonant at energies between the two peaks of interband transitions located at 3 eV and 1.4 eV. During this transition, as the LSPR shifts to higher energies below 2.5 eV, there is decreased variation between the dielectric functions of the VO_2 in each state, as can be seen in Figure 1.14.

The overall change in LSPR width is approximately 16% for the 100 nm particles and 21% for the 180 nm particles. For the 180 nm particles, the initial LSPR energy is 1.2 eV at the edge of the 1.4 eV transitions, and the LSPR shifts to 1.6 eV as the real part of the dielectric function of VO_2 decreases. Simultaneously, the imaginary part of the VO_2 dielectric increases as more states within the V $3d_{||}$ bands become accessible to the electrons in the VO_2, which are excited by the plasmon decaying into electron-hole pairs. As a result, we see a spike in the width of the LSPR before it can shift out of this region of the spectrum and a 30% decrease in dephasing time (Figure 3.6). In the next section, we will show that changes in ϵ_m can account for and reproduce the essential features of Figures 3.3 and 3.6 using the quasistatic electric dipole approximation with the Verleur dielectric function for VO_2 scaled to fit the plasmomic hysteresis data.

3.3.2 Modeling

Although several tools are available to model arrays of Au NPs coated with VO_2, the most straightforward is to calculate the dipole resonance using the quasistatic, electric dipole approximation (EDA) formalism described in Section 1.2.1. However, accurately modeling the Au::VO_2 structure described in this study requires a detailed understanding of the dielectric functions of VO_2 in both the semiconducting and metallic states, Au, and the ITO/substrate. Unfortunately, the Verleur dielectric data used in Figure 1.14 do not accurately describe the optical properties of our VO_2 films at energies above the bandgap. Modeling with the Verleur dielectric data generally results in broader LSPRs that are significantly redshifted relative to experiment, as seen in Figures 3.8 and 3.9, suggesting that our film has a reduced dielectric function relative to the Verleur samples. Furthermore, this discrepancy cannot be explained by a common scaling factor, as the predicted experimental shifts in LSPR upon phase transition are of different magnitudes than the Verleur dielectric functions. Fortunately, by using different scale factors for the 180 nm and 100 nm particle data, the essential features of Figures 3.3 and 3.6 can be reproduced. The VO_2 in its semiconducting state was scaled by defining $\epsilon_{\text{semi}} = C_1\epsilon'_{\text{semi}} + iC_2\epsilon''_{\text{semi}}$, where C_1 and C_2 are manually tuned fit parameters. This was similarly done for the metallic state. This method of fitting the plasmonic hysteresis corrects for array effects and should only be used as a rough estimate for the dielectric function for VO_2. The scaling constants used are given in Table 3.2.

As mentioned, the complex index of refraction given by Delta Technologies to

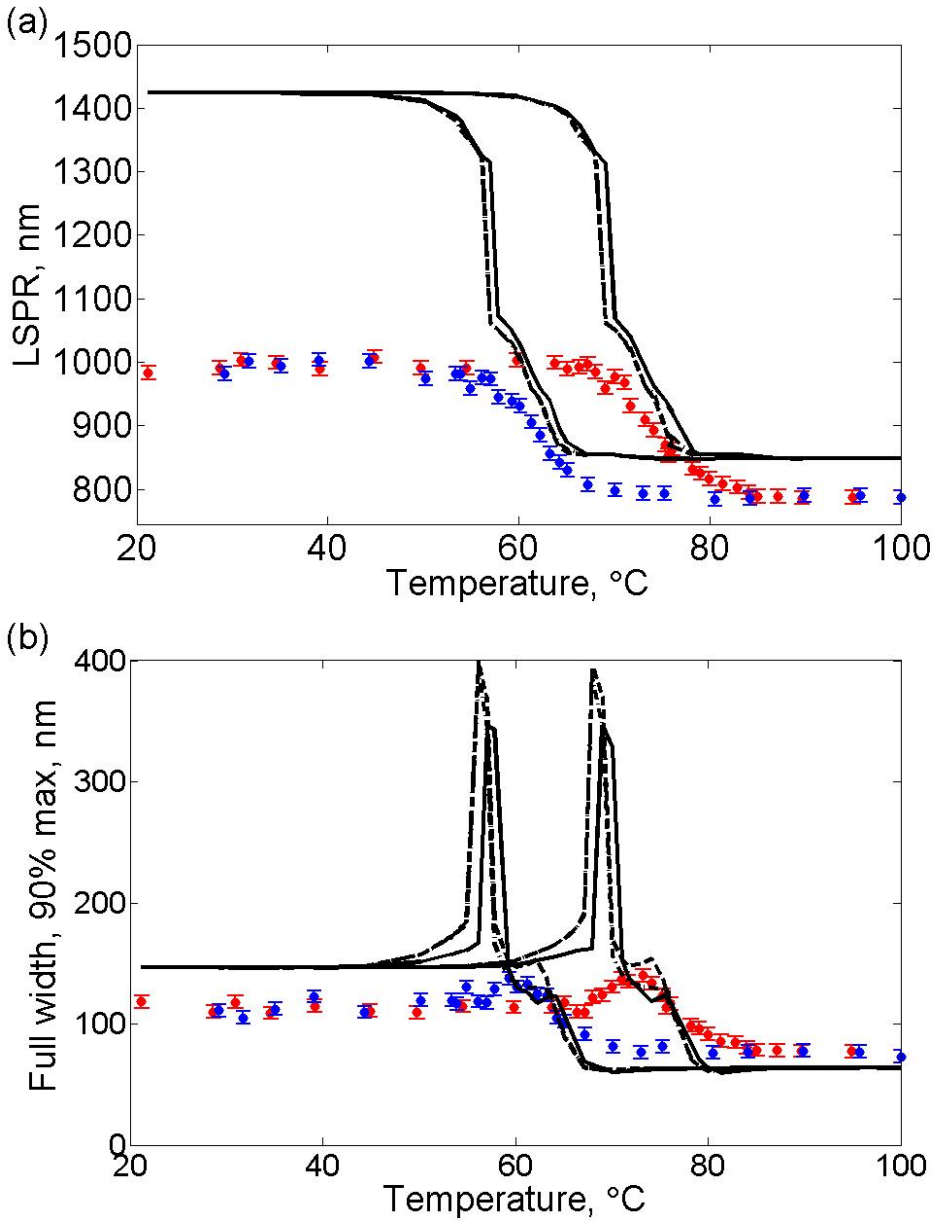

Figure 3.8: Plasmonic hysteresis (a) and width (b) and quasistatic model for the 180 nm particles, calculated using the Verleur dielectric function and using the linear (solid black), BR (dashed black), and MG (dashed-dotted black) effective medium models. The heating data (red) and cooling data (blue) are also shown.

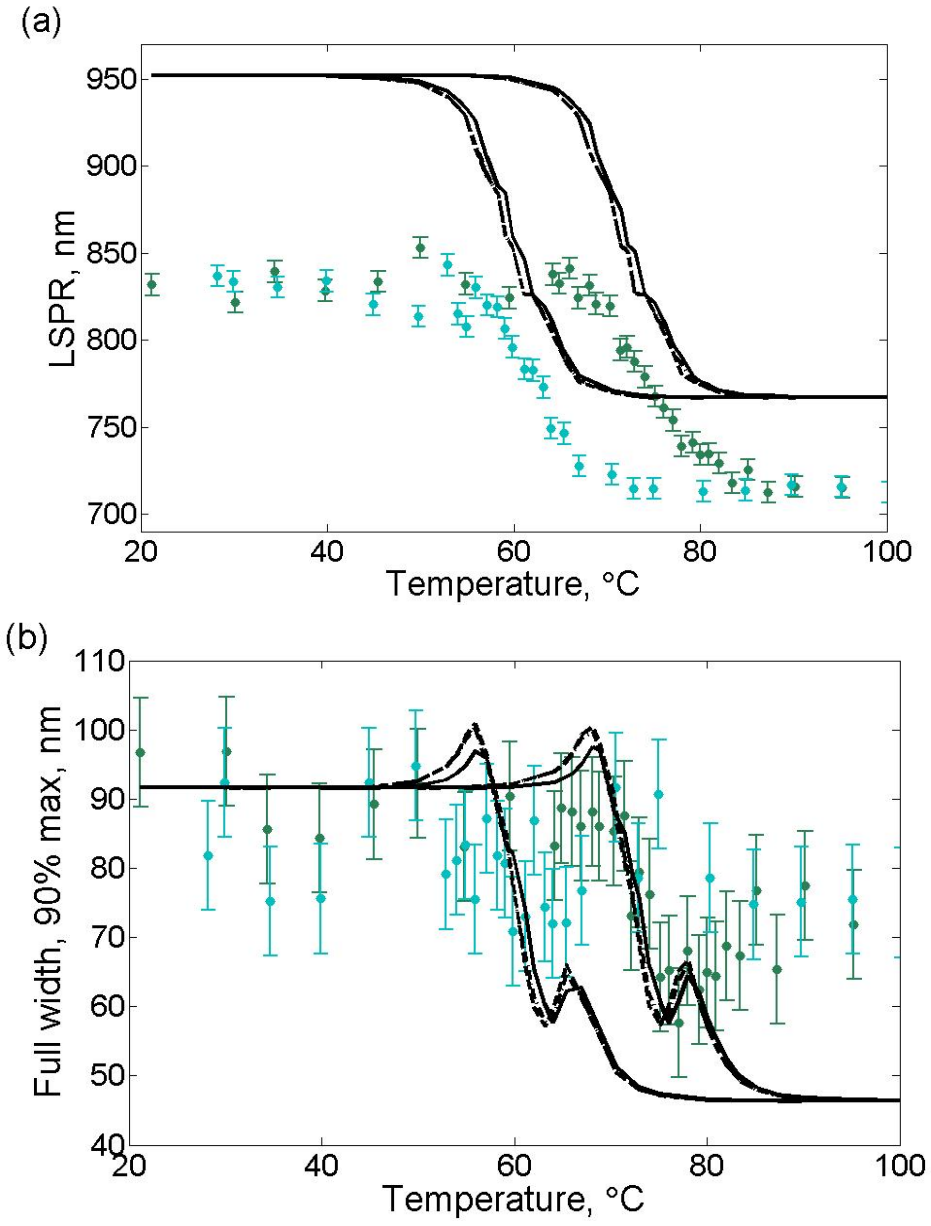

Figure 3.9: Plasmonic hysteresis (a) and width (b) and quasistatic model for the 100 nm particles, calculated using the Verleur dielectric function and using the linear (solid black), BR (dashed black), and MG (dashed-dotted black) effective medium models. The heating data (green) and cooling data (teal) are also shown.

Table 3.2: The scale factors used in order to compensate for discrepancies in VO_2 dielectric function for the experimental samples relative to the Verleur data.[38]

180 nm	C_1	C_2
VO_2^{semi}	0.53	0.33
VO_2^{met}	0.75	0.69

100 nm	C_1	C_2
VO_2^{semi}	0.67	0.25
VO_2^{met}	0.80	1.4

model the ITO, is $n_{\mathrm{ITO}} = 1.775 + 0.012i$, and effective medium theory will be used to model the dielectric function of the embedding medium. We define the effective medium as a weighted average of semiconducting and metallic dielectric functions. The linear model is given as[43]

$$\epsilon_{\mathrm{VO_2,eff}}(\lambda, T) = (1 - f)\epsilon_{\mathrm{semi}}(\lambda) + f\epsilon_{\mathrm{metal}}(\lambda). \tag{3.10}$$

The expression is an average weighted by the metallic fraction. This model was used to model the effective dielectric function of VO_2 instead of the BR or MG effective medium theories, as is typically done with the material, since the linear fit between λ_{LSPR} and f seen in Figure 3.4 better describes the LSPR hysteresis results. Finally, the average of the dielectric function of VO_2 and the ITO is taken to arrive at the effective medium $\epsilon_{\mathrm{m,eff}}$. Additionally, BR and MG effective medium models were also incorporated in the calculation. The expressions are given by Equations (1.17) and (1.18). Figures 3.8 through 3.11 show model calculations each effective medium model. Using the reduced Veleur dielectric functions described in Table 3.2, the BR

and MG effective medium theories do not produce a better fit of the LSPR hysteresis data than the linear model. However, the hysteresis of the LSPR width for the 180 nm NPs is actually modeled better using BR effective medium. This suggests that the width of the LSPR is more sensitive to the effective medium than the LSPR wavelength. Also, Figures 3.10b and 3.11b are not as accurate in modeling the data as Figures 3.10a and 3.11a; this is likely due to the model not accounting for LSPR broadening effects such as the array structure. The models in Figure 3.11b also suggest that the "noise" of the LSPR width present in the 100 nm NP data may actually result from dielectric changes in the film.

In each of the models, the spike in LSPR width is present. This supports the previously described hypothesis that the spikes are homogeneous in nature and are due to coupling of the Au plasmon to the VO_2 interband transitions. The models shown are for single NPs and do not account take into account radiation damping or inhomogeneous plasmon broadening. The effects of strong correlation are manifested in the changing of the VO_2 dielectric function. Whether or not a more accurate dielectric function can account for the decrease in τ_2 is still an unanswered question.

3.4 Effect of Changing Grating Constant

Figure 3.12 shows the LSPR extinction efficiency for 100 μm square arrays with varying grating constants. The shifts of less than 100 nm in the peak position of the LSPR as a result of variation in grating constant is due to far-field (diffractive) coupling within the array.[49,50,126] Figure 3.13, from [50], shows this effect for NP arrays in air. As can be seen from both our data and the data from [50], this cou-

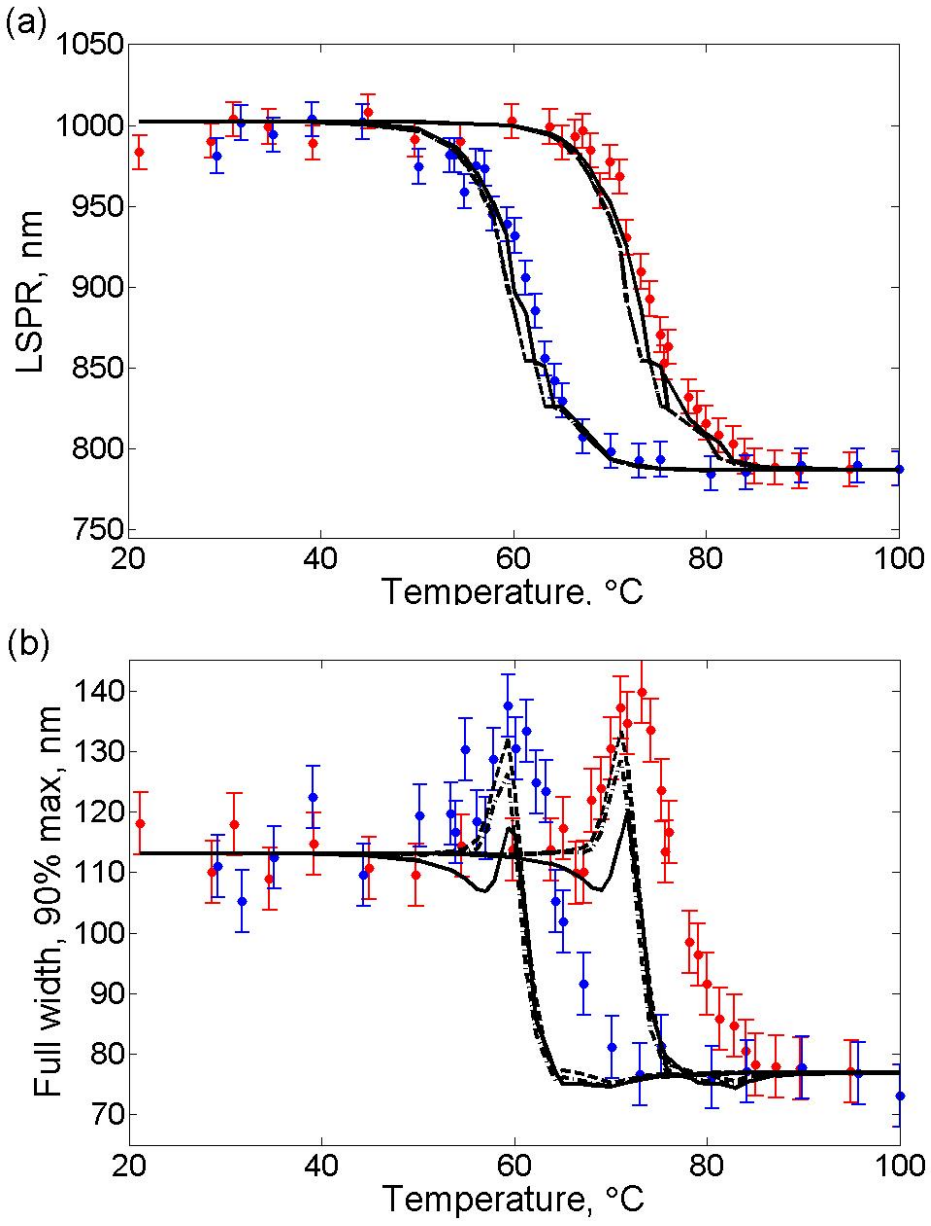

Figure 3.10: Plasmonic hysteresis (a) and width (b) and quasistatic model for the 180 nm particles, calculated using the reduced Verleur dielectric function and using the linear (solid black), BR (dashed black), and MG (dashed-dotted black) effective medium models. The heating data (red) and cooling data (blue) are also shown.

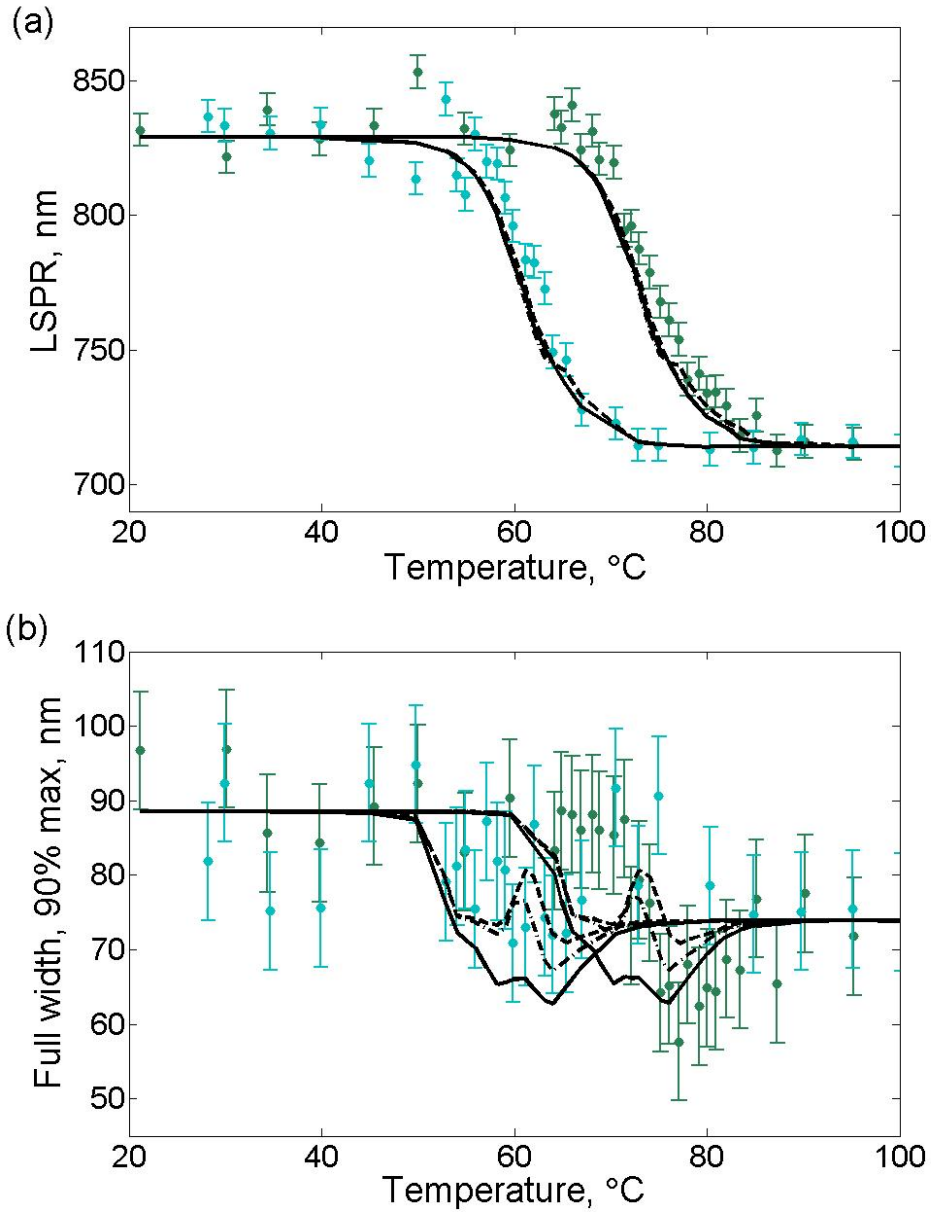

Figure 3.11: Plasmonic hysteresis (a) and width (b) and quasistatic model for the 100 nm particles, calculated using the reduced Verleur dielectric function and using the linear (solid black), BR (dashed black), and MG (dashed-dotted black) effective medium models. The heating data (green) and cooling data (teal) are also shown.

pling can have a significant effect on the width and position of the LSPR in the array geometry. Changes in the coupling strength between particles are due to the predominantly dipolar fields changing from evanescent to radiative as the spacing moves from one diffraction order to the next as the grating constant increases. This leads to an oscillation in coupling strength as the grating constant continues to increase, with particularly strong coupling occurring when the grating constant equals the resonance wavelength in the embedding medium. Likewise, changes in the width and asymmetry of the resonance associated with varying the grating constant can also be attributed to this mechanism.[50]

As the grating constant increases, a second resonant mode appears around 700 nm in the semiconducting state for both the 100 and 180 nm arrays. Data on arrays with 500 nm grating constant (Figure 5.1b) also have this pronounced second mode, which is likely a quadrupole resonance.[127,128] As ϵ_m increases, higher order modes redshift away from the interband transitions and become less damped.[43] The index of refraction for VO_2 is approximately 2.0 at 800 nm according to the reduced Verleur dielectric function used for the modeling, and the index of refraction for ITO is approximately 1.775. The effective index of refraction is therefore close to 1.89, and the wavelength of 700 nm light is approximately 370 nm in the film. This suggests that this mode should be strongly coupled to the grating constant. For the 300 nm and 350 nm case, the mode appears below 600 nm and redshifts as the grating constant increases.

Comparing the shift in resonance as a function of grating constant, Figure 3.12, we can see that the difference in coupling strength due to changing diffractive order

manifests itself by changing the sensitivity of the LSPR to changes in ϵ_{m}. Although the fractional magnitude of the shift versus grating constant is approximately the same for each array, the relationship has opposite sign. The 180 nm diameter particle array loses sensitivity to the change in ϵ_{m} with increasing grating constant, while the 100 nm array gains sensitivity. The structure of ϵ_{m}, which has less contrast between semiconducting and metallic states with blueshifting wavelength (Figure 1.14) does not account for this changing sensitivity. This suggests that the mechanism is related to the far-field coupling within the array, which is dependent on the wavelength in the medium.

These results, when compared to the 500 μm square arrays used in the plasmonic hysteresis study, show that the 180 nm particles are consistent in the magnitude of the shift: a 209 nm shift for the 500 μm array and 217 nm shift for the 100 μm arrays with grating constant 450 nm. However, the data for the 100 nm particles show shifts of 117 nm and 170 nm for the small and large arrays with the same grating constant. The standard deviation for the 100 nm particle LSPR in the plasmonic hysteresis data for semiconducting VO_2 before the onset of the phase transition is approximately 6 nm, suggesting that this discrepancy is well outside the margin of error for the 100 nm particles. Since the 100 μm array is 2 orders of magnitude larger than the LSPR wavelength, it is not likely that the size of the array has an impact on the shift in LSPR; however, the origin of the discrepancy is still unknown.

Assuming that λ_{LSPR} versus f remains linear for different grating constants, array effects can be characterized by the ratio M/κ. Figure 3.14a shows that this ratio for the 180 nm and 100 nm particles fits with quadratic functions of the form ax^2+bx+c

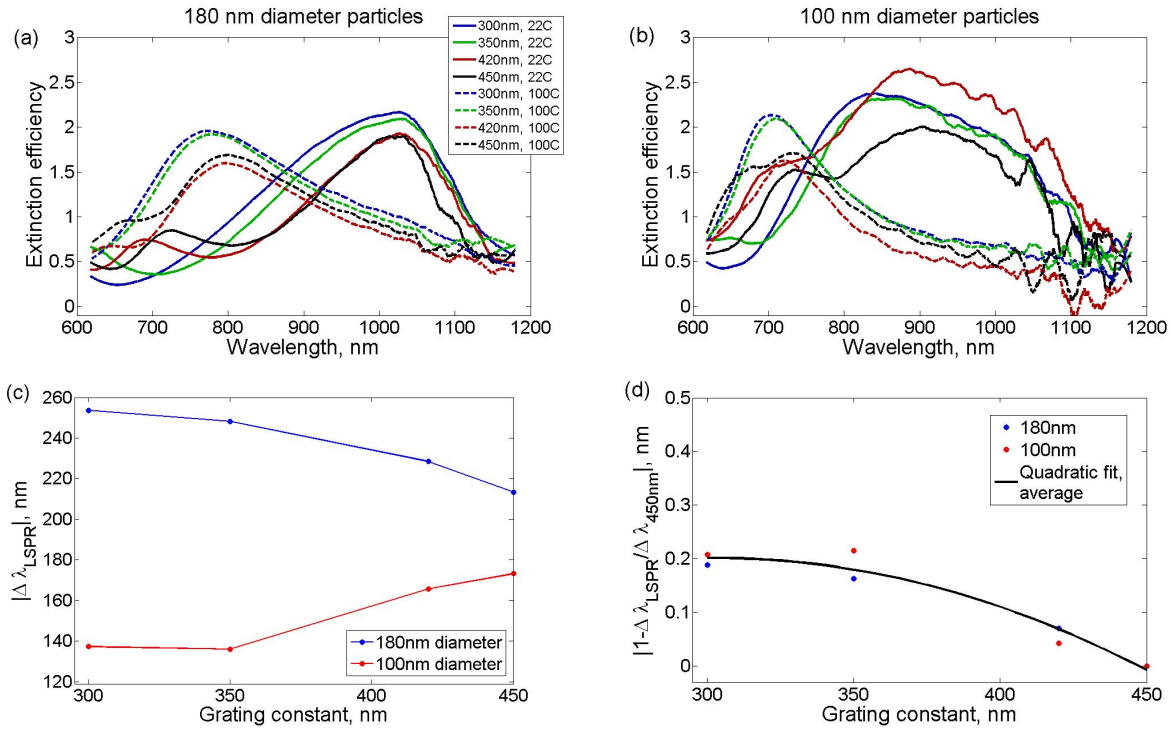

Figure 3.12: Extinction efficiency spectra for varying grating constant for the (a) 180 nm and (b) 100 nm diameter particles arrays. The legend shown in (a) also applies to (b). Bottom figures shows magnitudes of the (c) change in resonance upon phase transition as a function of grating constant and the fractional change (d) of LSPR normalized to the array with 450 nm grating constant.

with coefficients $(a,\ b,\ c)$ of $(-1.35\times10^{-4},\ 0.08,\ 8.47)$ and $(2.79\times10^{-4},\ -0.17,\ 45.6)$ for the 180 nm and 100 nm particles respectively. The change in M/κ is smooth over this range and levels out for the 180 nm particles as the grating constant decreases. This suggests a maximum sensitivity can be achieved, at least for far-field coupling between NPs. In contrast, the 100 nm particles, show an increase in sensitivity at 450 nm. However, it is difficult to make conclusions from this trend due to the noise in the data, especially since the 500 μm array has an M/κ ratio of 16.9 at 450 nm compared to the approximately 24.7 ratio for the 100 μm array.

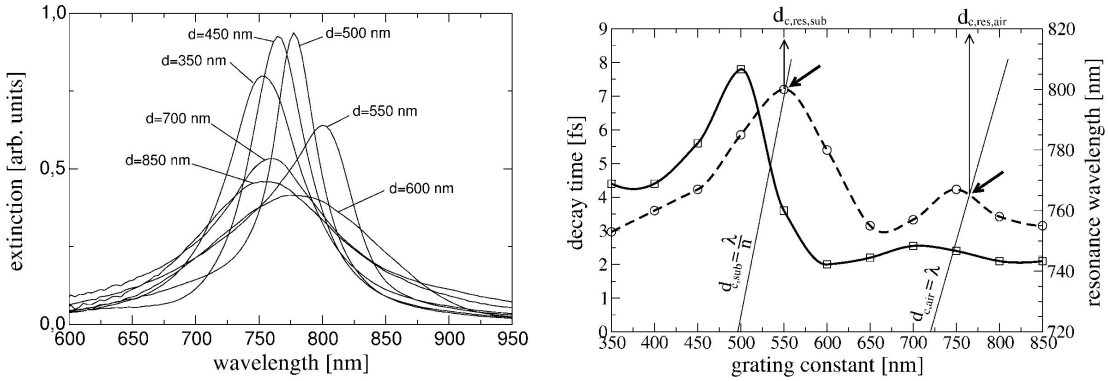

Figure 3.13: From [50], (left) the LSPR for 150 nm diameter, 14 nm thick Au particles with various grating constants (right) and the wavelength (dashed line) and decay times (solid line) for the LSPR as a function of grating constant. A maximum occurs when the wavelength in air λ and the substrate λ/n is equal to the grating constant d, where n is the index of refraction for the substrate.

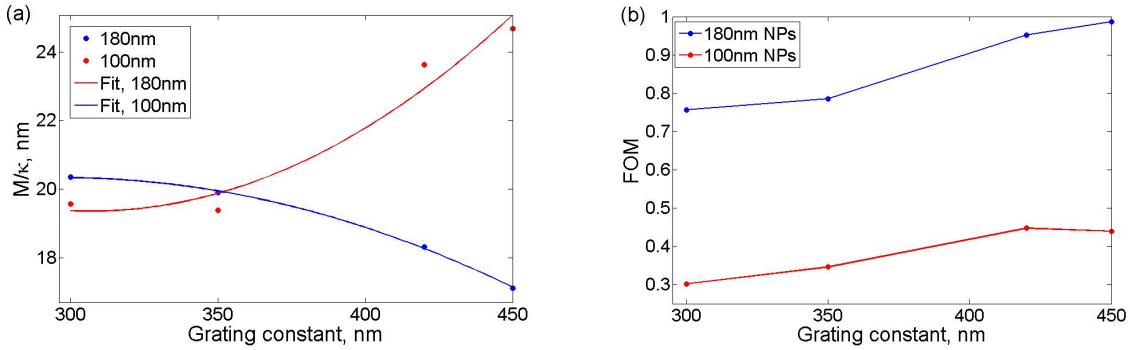

Figure 3.14: (a) The M/κ ratio fit to a quadratic and (b) the FOM, characterizing the sensitivity of the Au::VO_2 structure to changes in ϵ_m, as a function of grating constant.

For systematic comparisons between different geometries, Dicken *et al.* introduces a figure of merit (FOM) defined as the magnitude of the ratio between the shift in resonance wavelength and the resonance width in the semiconducting state of VO_2;[21] that is,

$$FOM = \left| \frac{\Delta\lambda_{\mathrm{LSPR}}}{\Gamma_{\mathrm{semi}}} \right|. \tag{3.11}$$

Although the sensitivity of the LSPR to changes in ϵ_{m} increases with decreasing grating constant for the 180 nm particles, both the 100 nm and 180 nm particles show a decrease in the FOM with decreasing grating constant as a result of a widening of the resonance (Figure 3.14b). This suggests that only a limited increase in ΔQ is possible for single particle arrays, even upon optimization.

3.5 Conclusions

In this study we used Au NP arrays as nanoantennas to observe the thermally induced phase transition of the VO_2. We showed that the shift in LSPR due to the SMT is linear in its dependence on the metallic fraction and that the change in effective medium due to the SMT can be described as an average over metallic and semiconducting dielectric functions at each temperature. This implies that the BR and MG effective medium theories are not necessary to model the plasmonic hysteresis. Whereas the shift in LSPR wavelength is primarily driven by the change in ϵ'_{m}, the change in LSPR width is related to the change in ϵ''_{m}. In regions of the spectrum where ϵ''_{m} is dominated by interband transitions, there is significant broadening of the LSPR. During the transition, the LSPR line width increases for the 180 nm particles

as the split $3d_{||}$ bands come together and the $3d_{\pi}$ band lowers to form the conduction band. The broadening in the region of the spectrum for metallic VO_2 is mainly due to an increase in free-electron damping as a result of the split $3d_{||}$ bands coming together to form the metallic VO_2 conduction band.

These results suggest that two different experiments may be conducted in order to take advantage of these findings. First, spherical NPs may be used to probe changes to ϵ''_{m} within a smaller wavelength band because they have been estimated to have the minimum shift in LSPR wavelength. This would allow for continuous monitoring of a specific energy band. A second experiment probing the arrays at an angle other than the normal may allow for an increased coupling between the plasmon and the strongly correlated electrons of the VO_2 by exciting the plasmonic mode along the 20 nm axis of the particle. This would lead to chemical interface damping and further broadening of the LSPR. Alternatively, spherical particles of diameter smaller than 20 nm may be used.

Finally, it was shown that the damping of the plasmon due to losses in the VO_2 significantly affects the optical characteristics of Au::VO_2 structures between 600 and 1200 nm, leading to broad resonances, but significantly lowered extinction efficiency compared to NPs in air. These broad plasmonic resonances due to the significant absorption in the optical-to-NIR by the VO_2, also limit applications for the structure in the visible by reducing the amplitude and increasing the width of the resonance. This limits the absorption that the Au NPs can contribute to Au::VO_2 structures in at wavelengths below 1500 nm. Analysis of the FOM and the sensitivity of the shift in LSPR wavelength to changes in ϵ_{m} suggests that optimizing the grating constant

will only result in a marginal improvement of ΔQ. The next chapter discusses the prospects of near-field interactions increasing the FOM.

CHAPTER IV

DIMER INTERACTIONS IN GOLD::VANADIUM DIOXIDE STRUCTURES

Abstract

The particle plasmon resonance (LSPR) wavelength and spectral width depend on particle shape, size, local dielectric function, and interparticle interactions.[43,44] Recently, it has been predicted by Jain *et al.* that the LSPR wavelength of spherical nanoparticle pairs, or nanodimers (NDs), exhibit enhanced sensitivity to changes in the local dielectric function compared to single nanoparticles (NPs).[39] We extend Jain's analysis to ellipsoidal arrays of NDs that are lithographically fabricated and coated with 60 nm of VO_2 that undergoes a semiconducting to metal phase transition (SMT) near 68°C. Extinction measurements were made above and below the critical temperature. Measurements showed a clear dependence of LSPR sensitivity to interparticle separation dependent on the state of the VO_2. However, damping of the plasmon due to the VO_2 interband transitions leads to a drastic reduction in coupling strength in the long-axis mode as dimer spacing increases. Damping due to interband transitions and increased coupling compete to broaden the LSPR at small spacing.

4.1 Introduction

The particle plasmon resonance (LSPR) wavelength and spectral width depend on particle shape, size, local dielectric function, and interparticle interactions.[43,44] For pairs of interacting NPs, known as nanodimers (NDs), near-field interactions dominate at edge-to-edge distances less than approximately 50 nm.[46,47] In arrays of single NPs with grating constant $D \approx \lambda$, far-field interactions dominate, resulting in a shift of the LSPR position and width with changes in D. For arrays of NDs, shown in Figure 4.1, with center-to-center gap $r \ll \lambda$, both far-field and near-field interactions must be considered, with the near-field interactions dominating between the pair of

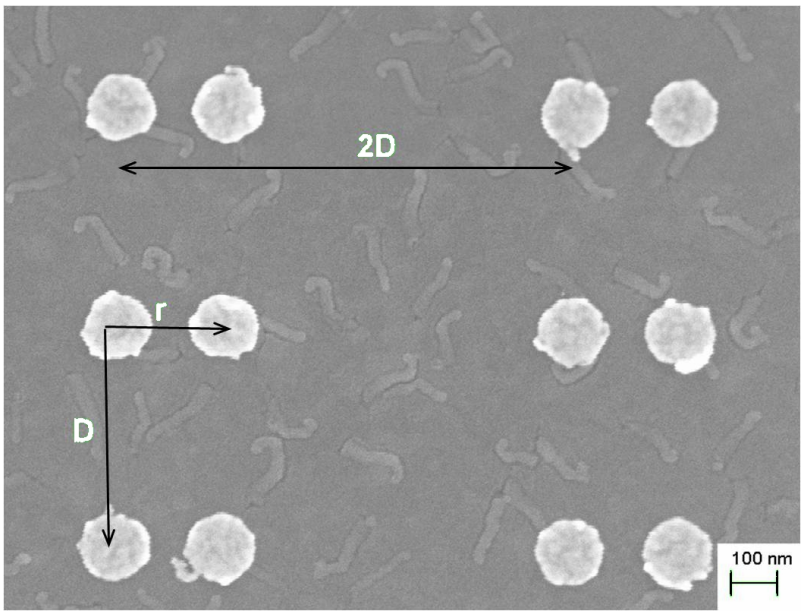

Figure 4.1: Typical scanning election microscopy image of Au ND arrays.

particles.[48–50,129–131] These interactions can be modeled as interacting point-dipoles within the quasistatic dipole approximation.[129,131]

Recent theoretical work by Jain *et al.* on spherical NDs, [39], predicts that the LSPR should exhibit enhanced sensitivity to changes in the local dielectric function for NDs over single NPs. That is, as the dielectric function increases, the LSPR wavelength for closely spaced dimers experiences a greater shift relative to the LSPR wavelength for dimers spaced farther apart. This implies that the LSPR wavelength will undergo a greater shift in position with changes in ND spacing if the particles are embedded in a medium with higher dielectric function than in air. The increase in sensitivity is manifested as an increase in slope in the LSPR wavelength as a function of r. Although interacting pairs of NDs have been well-studied in the literature,

these studies have used non-absorbing embedding media.[48,49,58,129–132] For a medium with absorption, the electric field outside of the particles is reduced,[133] leading to a reduction in the high electric field found in the ND gap. This decreased electric field reduces the EM coupling between the particles.

In this chapter, we extend the analysis by Jain *et al.* to include arrays of ellipsoidal particles embedded in an absorbing medium and measure the sensitivity of the Au::VO_2 ND LSPR to changes in the dielectric function of the VO_2. We will show that for Au::VO_2 structures excited at energies above the VO_2 band gap (0.7 eV),[26] the coupling of the VO_2 interband transitions to the Au LSPR leads to a reduction in coupling efficiency between the NDs. Polarization differences in interparticle interactions are also measured.

The work in this chapter also extends the analysis in Section 3.4, where we showed the effect of changing D on the sensitivity of the LSPR. We found that for 180 nm particles, a smaller grating constant increases the sensitivity. In the following sections, we explore the interactions between NPs more fully and derive an effective geometrical factor L_e as is done in [56]. First, the interactions of NDs in air will be presented, followed by interactions in VO_2. Our analysis shows that the short-axis mode is more sensitive to changes in r at larger distances than the long-axis mode due to a reduced near-field coupling strength between the particles and additional far-field coupling between the NDs. Furthermore, the absorption of EM energy through VO_2 interband transitions lead to a drastic reduction in coupling strength for the long-axis mode for metallic VO_2. The interband transitions and ND coupling also contribute to broadening the LSPR as ND spacing decreases.

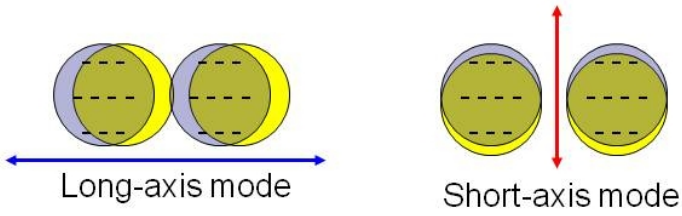

Figure 4.2: Schematic representation of the polarization dependent LSPR modes in NDs. The arrows indicate the polarization of the incident light.

4.2 Experimental Details

Samples were prepared lithographically as described in Section 2.1 to produce arrays of Au NDs of various particle diameters ($2R = 100$ nm, 150 nm, 180 nm) and center-to-center dimer spacing r. A scanning electron micrograph of a typical ND array is shown in Figure 4.1. We define the x-axis to be along the dimer axis, also known as the "long" axis, as shown in Figure 4.2. As r is varied, the grating constant D is kept unchanged in the y-direction (along the "short" axis) with $D = 500$ nm for the $2R = 180$ nm and $2R = 150$ nm NDs, while $D = 450$ nm for the $2R = 100$ nm. In the x-direction, the grating constant is set to $2D$ so that $r = D$ corresponds to the case of a square array. To test the effect of changes in the local dielectric function ϵ_m on ND coupling, a separate sample consisting of 180 nm diameter NDs with $D = 500$ nm was also prepared and covered with a 60 nm layer of VO_2 by PLD.

Extinction measurements were conducted as described in Sections 2.2.2 and 2.3.2. Since ND extinction is known to have a polarization dependence, a broadband linear polarizer was used to polarize the incident light. Typical ND extinction spectra for

particles on an ITO coated glass substrate exposed to air are shown in Figure 4.3a. The LSPR was redshifted for light polarized parallel to the long-axis relative to light polarized along the short-axis, consistent with theory and previous experiments.[129] The other plots in Figure 4.3 show the position of the resonance as a function of particle spacing r for particles in air and coated with VO_2. The shift in resonance is not very pronounced, especially at large distances, but can be significant for understanding the tradeoff between interband damping due to the VO_2 and damping due to the coupling between NDs. The error bars shown are set at 5% based on the signal-to-noise ratio of the unsmoothed transmission data (Figure 2.12).

4.3 Theoretical Discussion

Particle interactions within an array are essentially dipolar and the particles can be treated as point dipoles within the quasistatic approximation.[49,50,129,131] Close to the particle surface, this field is evanescent (non-radiative) and has a r^{-3} dependence, where r is the distance from the center of the particle. This field is strongly coupled to nearby particles. Near-field interactions dominate at surface-to-surface distances of less than approximately 50 nm.[43,129] As we increase the distance between particles so that r is comparable to the wavelength of incident light and the interactions are through far-field radiation, there is a r^{-1} dependence in the coupling strength. It is at these distances that diffractive effects can shift and broaden the resonance. Far-field coupling plays an important role in arrays of single NPs, as we discussed in Chapter III.[50]

For dimers within an array, the interactions are both near-field and far-field. As

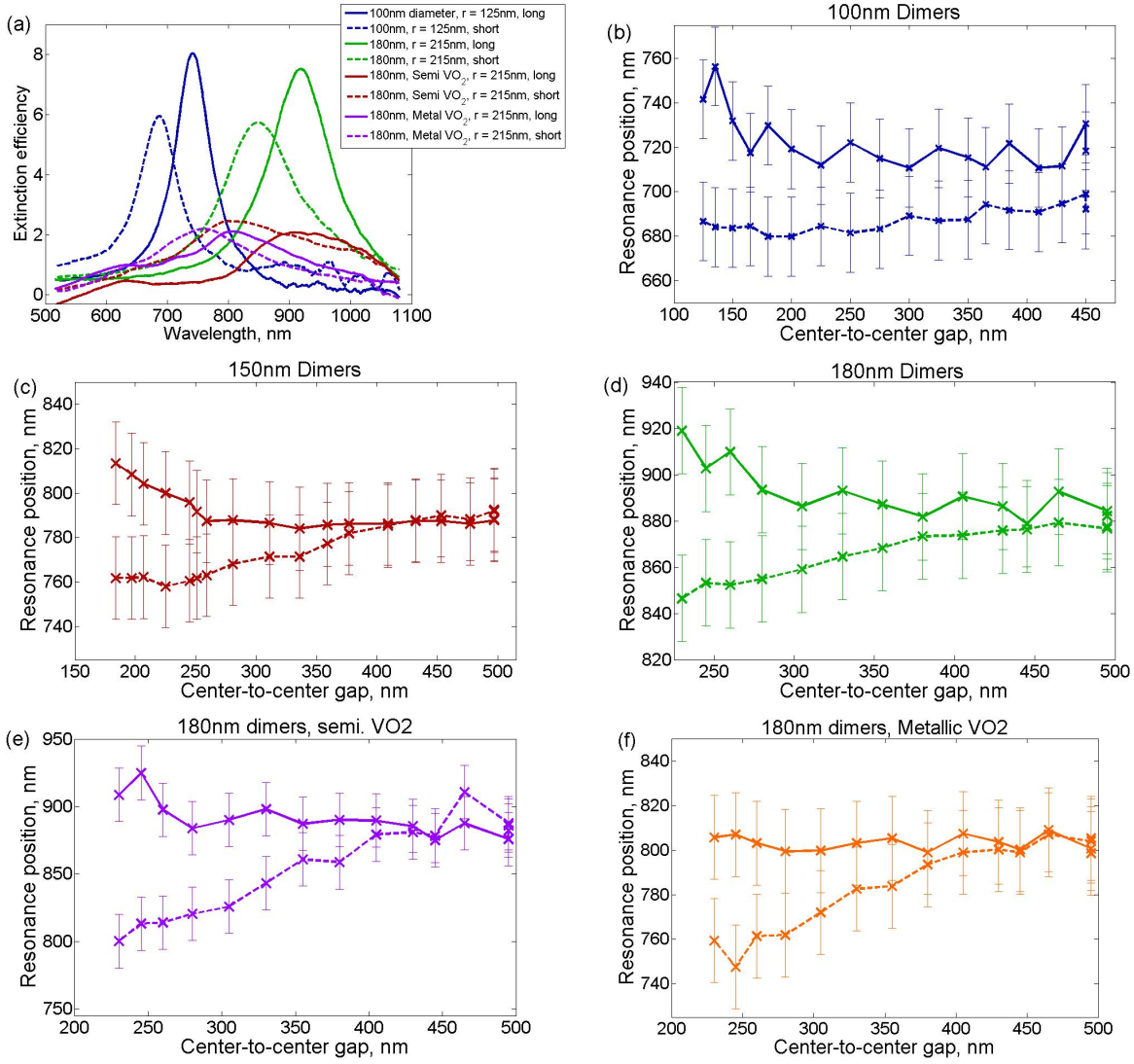

Figure 4.3: (a) Typical extinction spectra for Au NDs. Note that LSPR arising from long-axis polarization are redshifted relative to the resonances arising from light polarized along the short-axis. Other plots show the LSPR versus center-to-center gap r for (b) 100, (c) 150, and (d–f) 180 nm particles. Dashed lines indicate short-axis polarization, while the solid lines are the long-axis data. Error bars are estimated to be $\pm 2.5\%$ of the value based on the signal-to-noise ratio of the transmission measurements and the error analysis in Chapter III.

r decreases between two NPs, the interaction of the evanescent dipole fields breaks the symmetry of the single particle and splits the LSRP mode into two polarization-dependent oscillations.[58,129,132] Figure 4.2 presents a schematic representation of these modes. In the long-axis mode, the in-phase charge oscillation works to lower the restoring force of the plasmon. This redshifts the LSPR relative to the single particle case. For the short-axis polarization, the charge distribution works to increase the restoring force, and thus blueshifts the mode.[129]

This mode-splitting is analogous to the splitting of energy levels when atoms come together to form molecules, resulting in hybridization of NP energy states into radiative and non-radiative modes, as shown in Figure 4.4 and studied by Nordlander and colleagues.[58,132,134] For each polarization there is a symmetric, optically excited, bonding mode, as well as an anti-symmetric, optically dark, anti-bonding mode. The bonding and anti-bonding modes each exhibit a different dependence on r, where the bonding modes are consistent with the behavior described in the previous paragraph. In both the Nordlander and Jain studies (Figure 4.5), the ND LSPR dependence on r is predicted to be a smooth decrease in coupling strength proportional to r^{-3}. As the particles continue to separate, Dahmen *et al.* predict oscillations in the resonance energy and linewidth with a period approximately equal to the emission wavelength, as seen in Figure 4.6, and experimentally confirmed in [48] using scanning fiber probe microscopy.

Although useful for understanding plasmon interactions in NDs and other complex particles, Nordlander's calculations are difficult to implement for arrays of ellipsoidal particles. To model these interactions, the quasistatic electric dipole approximation

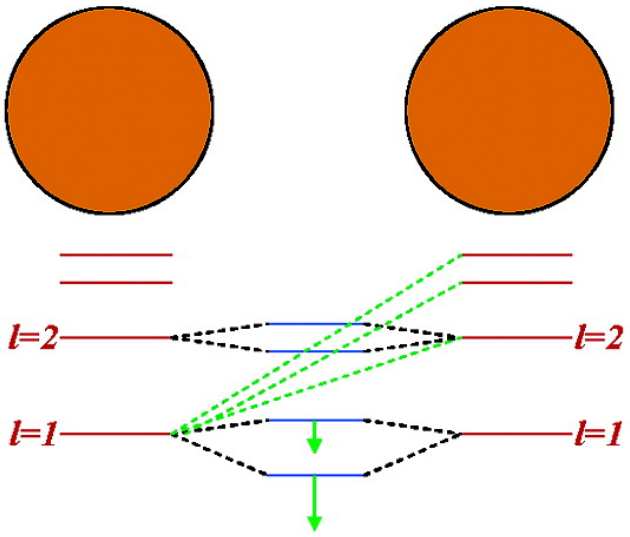

Figure 4.4: From [58], schematic of 10 nm diameter ND mode hybridization. As the particles approach, each mode can interact with multiple modes on the opposing particle, leading to mode splitting. For each polarization, two energy states, one bonding (the symmetrical mode) and one anti-bonding (the out of phase mode) are possible. The anti-bonding state is considered a dark mode that is difficult to excite optically.

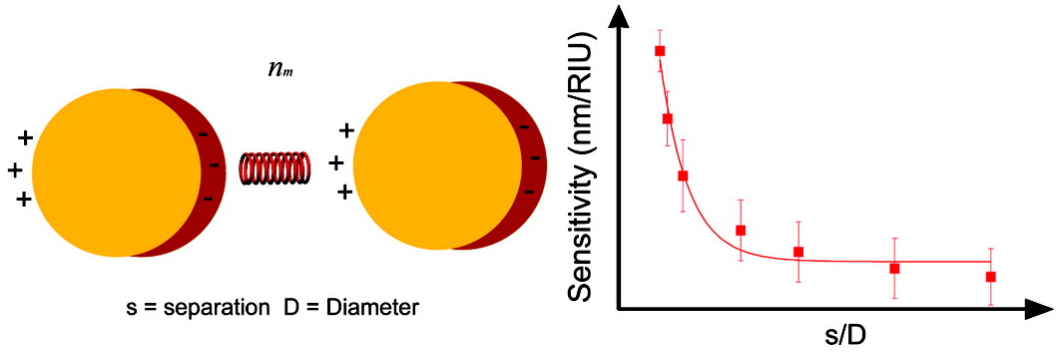

Figure 4.5: From [39], the sensitivity of spherical NDs to changes in dielectric constant as a function of distance. The fit is an exponential decay.

is used. We extend the methodology of Jain *et al.* to derive equations for ellipsoids and both long and short-axis polarizations that describe the coupling between NDs.

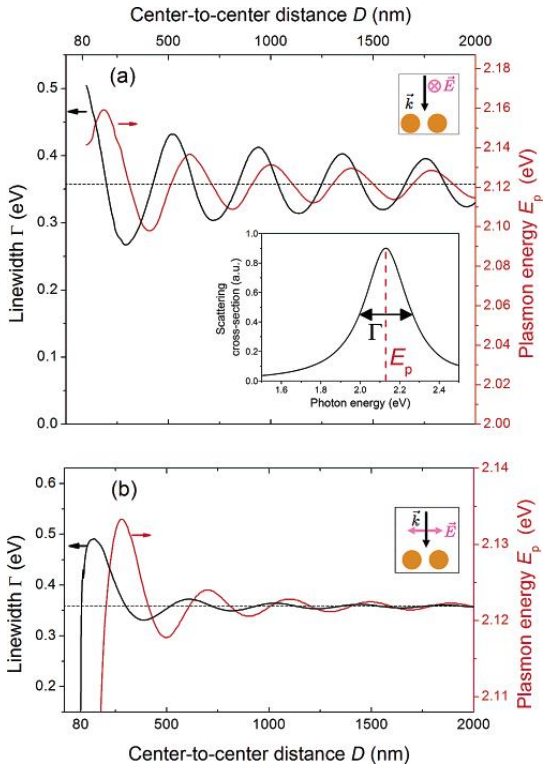

Figure 4.6: As the particle separation increases to several particle diameters in length and on the order of the emission wavelength, far-field coupling leads to oscillations in resonance energy and width. Figure taken from [131]. The diameter of the spheres is 80 nm in this study, and they are embedded in a medium with $n = 1.51$.

4.3.1 Dimers in the Quasistatic Electric Dipole Limit

We work in the quasistatic limit to find an effective dipole polarizability α_e for coupled particles.[39,49,56,126] Without loss of generality, we define the origin to be the center of one of the particles. This particle experiences a local electric field E_l given by

$$E_l = E_0 + E_d, \tag{4.1}$$

where E_0 is the incident light field and E_d is the dipole field at the origin due to other particles. This can be a single additional particle or an array, in which case

a summation over each particle in the array is included in E_d. Other corrections to the electric fields, such as the dipole mirror image due to the substrate, can also be incorporated into E_d.[33,51] We will assume that each particle in the system experiences the same local fields. In other words, we assume an infinite array and illumination spot larger than the array. The dipole field E_d is proportional to the dipole moment of the particles, and can be written as $E_d = S(r)P_d$, where $P_d = \alpha\epsilon_m E_l$ is the dipole moment of each additional particle and $S(r)$ is the dipole interaction function describing the coupling between the particles. Inserting this into (4.1) and solving for the local field yields

$$E_{loc} = \frac{1}{1 - S(r)\epsilon_m\alpha}E_0. \tag{4.2}$$

In general, both α and $S(r)$ are tensors, but we will assume that the polarization is along one of the major axes of the ND or ellipsoid.

If the dipole moment of the particle at the origin is $P = \alpha\epsilon_m E_{loc}$, we arrive at the α_e by (4.2). That is,

$$P = \alpha_e E_0 = \frac{\alpha}{1 - S(r)\epsilon_m\alpha}\epsilon_m E_0, \tag{4.3}$$

yields

$$\alpha_e = \frac{\alpha}{1 - S(r)\epsilon_m\alpha}. \tag{4.4}$$

Inserting the polarizability α for an ellipsoid, (1.4), into the above and simplifying, we get

$$\alpha_e = V\frac{\epsilon - \epsilon_m}{\epsilon_m + [L - VS(r)\epsilon_m](\epsilon - \epsilon_m)}, \tag{4.5}$$

which can be made to look identical to (1.4) by defining an effective geometrical factor

L_e as

$$L_e = L - VS(r)\epsilon_m. \tag{4.6}$$

Evidently, particle-particle interactions are effectively equivalent to distorting the shape of the particle. In other words, Coulomb interactions between particle plasmons can work to screen or enhance the restoring force between the electron cloud and the lattice, thus shifting the resonance frequency as does changing the shape of a particle. Furthermore, as will be clear in the following discussion, $S(r)$ can be complex and lead to increased or decreased damping of the LSPR, as seen by the changing width of the resonance in Figure 4.3. This formalism of effective geometrical factors is discussed further in [56].

Taking into account retardation effects, the electric field of an oscillating dipole can be written as

$$\vec{E}_d = \frac{e^{ikr}}{\epsilon_m}\left\{\frac{k^2}{r}\left(\hat{r}\times\vec{P}\right)\times\hat{r} + \left[3\hat{r}\left(\hat{r}\cdot\vec{P}\right) - \vec{P}\right]\left(\frac{1}{r^3} - \frac{ik}{r^2}\right)\right\}, \tag{4.7}$$

where k is the wavenumber and $\hat{r}$ is the unit vector in the direction of r. The first term corresponds to the far-field zone, while the second term, dependent on r^{-3}, corresponds to the near-field zone. The third term represents the intermediate zone.[5,61]

4.3.2 Near-field Dimer Interactions

We will now derive L_e for NDs as a function of separation. Assuming the particles are close enough that we can ignore retardation effects and the radiation and intermediate zone terms, as is done in [39], (4.7) simplifies to

$$\vec{E}_d = \frac{3\vec{P}\left(\vec{P}\cdot\hat{r}\right) - \vec{P}}{\epsilon_m r^3}, \tag{4.8}$$

where the unit vector $\hat{r}$ now specifically denotes the direction to the second particle. Considering each polarization state, we can see that

$$E_{d,L} = \frac{2P}{\epsilon_m r^3}, \tag{4.9}$$

and

$$E_{d,S} = \frac{-P}{\epsilon_m r^3}, \tag{4.10}$$

for the long and short axes, as denoted by the subscripts L and S, respectively. The field directions are parallel to the polarization of incident light. Therefore,

$$S_L = \frac{2}{\epsilon_m r^3} \tag{4.11}$$

and

$$S_S = \frac{-1}{\epsilon_m r^3}. \tag{4.12}$$

From (4.5) to (4.12), we can now discuss the dependence of the LSPR on ND spacing r. For the long-axis mode, as the particles come closer together, L_e decreases

and redshifts the LSPR as expected. For short-axis polarization, the negative sign in (4.10) causes L_e to increase and blueshift the LSPR. This behavior is qualitatively equivalent to the changes in LSPR associated with varying the axes of an ellipsoid.[44] Also, the long-axis polarization is more sensitive to the particle separation by a factor of two. The increased sensitivity of the long-axis mode is consistent with the literature, as reported for example in [129].

In this approximation of E_d, the dependence of L_e on ϵ_m vanishes when (4.11) and (4.12) are inserted into (4.6). The increase in sensitivity of the LSPR, as reported in [39], does not result from a difference in coupling strength between the dimers. It is rather a result of (1.6), where the sensitivity of the LSPR to changes in ϵ_m is proportional to $\kappa = 1 - L_e^{-1}$. The approximately linear dependence of the shift in LSPR on ϵ_m was shown experimentally in Figure 3.4. It is worth noting that in general, this is not the case. Using the full retarded dipole field, (4.7), the coupling strength depends on ϵ_m through the wavenumber k. The dipolar coupling functions for each polarization using the full retarded fields are

$$S_{L,ret} = \frac{2e^{ikr}}{\epsilon_m}\left(\frac{1}{r^3} - \frac{ik}{r^2}\right), \tag{4.13}$$

and

$$S_{S,ret} = \frac{e^{ikr}}{\epsilon_m}\left[\frac{k^2}{r} - \left(\frac{1}{r^3} - \frac{ik}{r^2}\right)\right]. \tag{4.14}$$

These equations demonstrate that the dependence of the LSPR wavelength on ϵ_m is not linear for coupled particles. One key difference between Equations (4.13)

and (4.14) is the dependence on the far-field radiation term. This term completely disappears in the calculation of E_d for long-axis polarization due to the orientation of the dipole field relative to the plasmon oscillation. For this reason, short-axis modes exhibit stronger coupling at larger distances than long-axis modes, although the long-axis mode is more sensitive to changes in r at close distances. Secondly, for an absorbing medium such as VO_2, both ϵ_m and k are complex, leading to several additional terms in Equations (4.13) and (4.14). Most importantly for our discussions, the coupling now contains a factor of $\exp(-k''r)$.

The differences in ND coupling dependence between non-absorbing and absorbing media, to our knowledge, have not been previously mentioned in the literature. Far-field oscillations due to the factor of $\exp(ik'r)$ occur over a period of hundreds of nanometers.[131] For example, in semiconducting VO_2 for 180 nm particles, it is estimated that the wavelength of the oscillation is approximately 440 nm compared to $r = D = 450$ nm for the largest center-to-center distance measured. Therefore, approximately one full oscillation may be present in the data, assuming that the reduced dielectric function estimated in Chapter III is accurate.

The changes in electric field intensity for interacting NDs in non-absorbing medium consisting of a glass substrate and air can be seen in FDTD calculations shown in Figure 4.7.[135] For long-axis polarization of incident light, the field in the center of the gap between the dimers is high, but falls off quickly as the gap opens. At close distances, this distorts the field distribution around the particle, lowering the field intensity on the surfaces farthest from the "hot spot" between the particles. As the gap opens, the field intensity distribution becomes more symmetric, indicating that

the coupling has decreased. At close distances for the short-axis polarization, the dipolar field distribution produces nearly zero field in the gap. Furthermore, the dipolar intensities of the short-axis mode are slightly distorted because of Coulomb repulsion so that the lobes of the charge distribution are repelled from one another. As the particles move apart along the dimer axis, the intensities of the short-axis electric field increases relative to that of the long axis, implying an increase in far-field and intermediate-zone coupling relative to the long-axis polarization. At 100 nm surface-to-surface separation, the short-axis modes show more pronounced signs of coupling than the long-axis mode at the same distance. However, by $r = 240$ nm the field distributions appear dipolar, with almost zero field intensity far from the particle surface.

4.4 Analysis of Experiment

The following analysis focuses on the near-field coupling dependence of the NDs. Taking advantage of the near linearity of ϵ between 600 and 1200 nm (Figure 1.7), the shift in LSPR is approximated as the difference in ϵ values at the LSPR wavelength using (1.6), as done in [39]. After some algebra, this yields

$$\Delta\lambda \propto \frac{-VS\epsilon_m}{L - VS\epsilon_m}\frac{\epsilon_m}{L}. \tag{4.15}$$

To account for the effects of substrate and the entire array, we parameterize (4.15) as

$$\frac{\Delta\lambda}{\lambda_0} = \frac{Ad^{-3}}{1 - Bd^{-3}}, \tag{4.16}$$

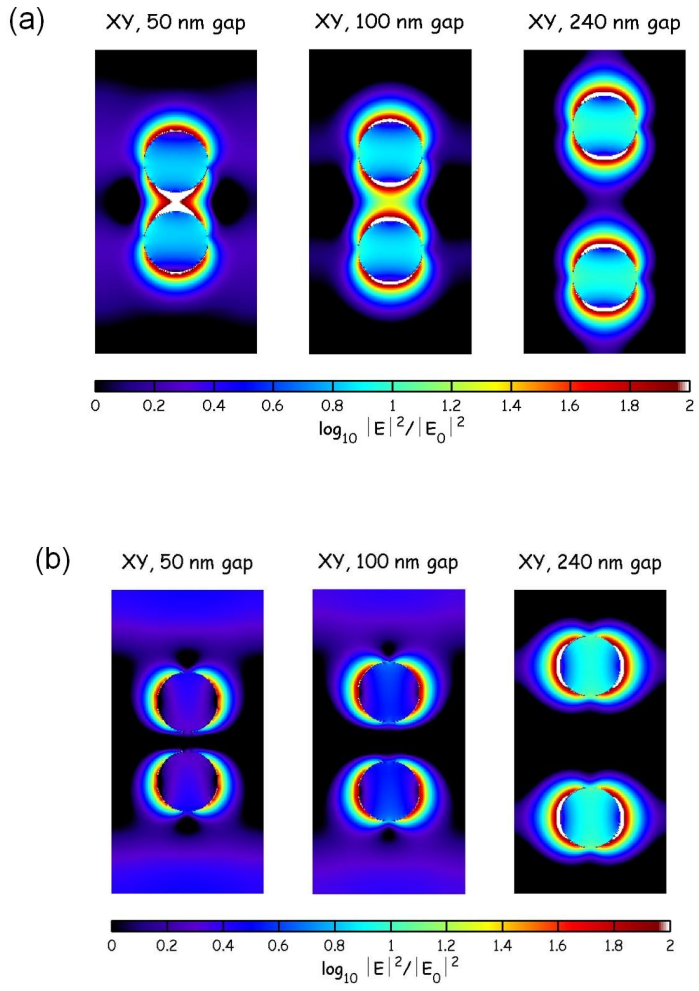

Figure 4.7: FDTD simulations of a ND system for (a) long-axis and (b) short-axis polarization modes showing the field intensity around the particles. These simulations were conducted using Optiwave FDTD software, Version 5, in collaboration with Kevin Tetz.

Table 4.1: The value of the fit parameters for the relative LSPR shift in Figure 4.8 using (4.16).

	Long-axis		Short-axis	
Diameter	A	B	A	B
100 nm	4.8	0.82	-28	-17
150 nm	2.3	1.2	-34	-5.7
180 nm				
air	4.2	1.1	-7.8	-0.04
VO_2 semi	4.7	0.84	-24	-0.23
VO_2 metal	29	-42	-19	-0.54

where d is the center-to-center distance normalized to the particle diameter $2R$, and A and B are dimensionless fit parameters. Table 4.1 lists the fit results while Figure 4.8 plots the per cent change of the LSPR versus center-to-center gap along with the fit.

As seen in Figure 4.8, the parameterization proposed in (4.16) provides a reasonable fit to the data and one that is consistent with other studies.[39,58,129] With the exception of 180 nm NDs embedded in metallic VO_2, the values of the fit parameters are consistent. The variations can be attributed to retardation effects in the field between the NDs. For the case of the long-axis mode, metallic VO_2, both parameters A and B are much larger than the other cases, resulting in essentially a line through the data. The flatness of the data for metallic VO_2 is most likely due to the exponential decay in coupling strength for NDs in absorbing media; measurements at smaller gap lengths may be necessary to measure this dependence.

The fit only accounts for near-field coupling. There appears to be substructure present in several of the data sets, especially the 180 nm particles with metallic

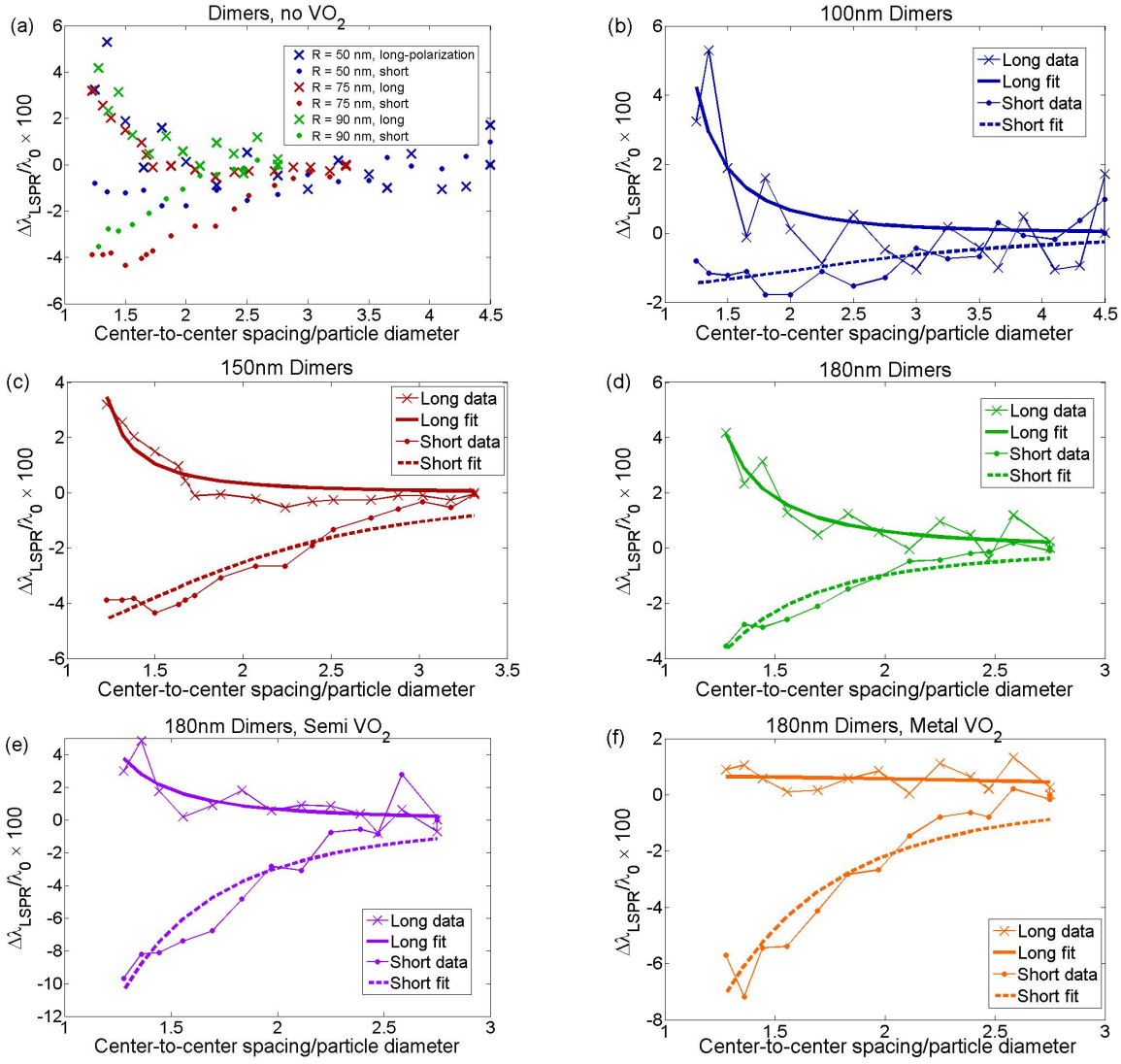

Figure 4.8: (a) For comparison, the fractional change of the LSPR wavelength versus ND spacing, $\Delta\lambda_{LSPR}/\lambda_0 \times 100$, where λ_0 is the LSPR wavelength of the square array. Other plots show the fractional change of LSPR versus center-to-center gap d for (b) 100, (c) 150, and (d–f) 180 nm particles. The 'x' ('•') indicates long-axis (short-axis) polarization data, while the solid (dashed) line is the parameterized fit.

VO_2. Due to the reduced wavelength of light in the VO_2, far-field oscillations may be present. Additionally, the array structure is changing as each ND gap increases in separation. This may be responsible for some of the structure present in the data but not captured in the fit.

4.4.1 Sensitivity of Nanodimers to Changes in Dielectric Function

Returning to the original motivation for this work, the increased sensitivity of NDs to changes in ϵ_m with decreased r, Figure 4.9 shows the three 180 nm particle data sets on the same plot. However, instead of normalizing r to the diameter of the particle, the center-to-center gap was normalized to λ_{LSPR}/n, where n is the real part of the effective index of refraction, estimated based on the analysis performed in Chapter III to be approximately 1.3, 1.5, and 1.9 for the particles in air, metallic VO_2, and semiconducting VO_2 respectively. For the long-axis polarization, there is at most a 0.01 increase in the fractional change of the LSPR at the smallest gap for the semiconducting state of VO_2 over the particles exposed to air (Figure 4.8) when plotted against r. There is about a 0.03 increase in the fractional change for the semiconducting state over the metallic state for the smallest ND gap. This is not expected based on our theoretical analysis and the work by Jain *et al.* since ϵ'_m for the metallic state of VO_2 is between that of the semiconducting VO_2 and air.[39] When normalizing to the reduced LSPR wavelength, as done in Figure 4.9a, it becomes clear that the semiconducting state experiences a much higher increase in sensitivity with decreasing gap length relative to air. On the other hand, the curves for the long axis polarization between the air and metallic state of VO_2 seem to line up. This

is likely due to the higher absorption in metallic VO_2. Apparently, the additional factor of $\exp(-k''r)$ drastically decreases the coupling strength between the NDs in metallic VO_2.

For the short-axis mode there is more than a doubling of the fractional change at the smallest gap for the particles coated with semiconducting VO_2 relative to the sample in air. The semiconducting state shows approximately twice the increase in shift relative to air over the metallic state. This is reasonable since the real part of the dielectric function of semiconducting VO_2 is roughly twice that of the metallic state. These results also show that for Au::VO_2 geometries, the short-axis polarization maintains sensitivity to changes in r at larger particle spacings than the long-axis polarization. This is due to the additional far-field coupling term found in (4.14).

The increased sensitivity of the LSPR to changes in ϵ_m as a function of particle spacing is clearly seen in Figure 4.9(b), where the fractional shift in LSPR wavelength for the square array is subtracted from the fractional shift in LSPR for the other data points. The result is fitted to (4.16). The fit results give the parameter values as: for the long axis polarization $A = 2.7$ and $B = 1.2$; for the short axis polarization $A = -8.2$ and $B = 0.3$. The LSPR shifts by 0.12 for the second to smallest gap and only 0.08 for the square array, giving a difference of 0.04. However, this increase in sensitivity is not mirrored in the short-axis data, where there is a decrease in sensitivity for decreasing gap size. The short-axis mode may be more sensitive to changes in the gap at further distances, but it is apparently not as sensitive to changes in the dielectric function, exhibiting a decrease of 0.05 from the smallest gap compared to the square array. This can be understood from (1.6) and (4.6). As r increases, L_e

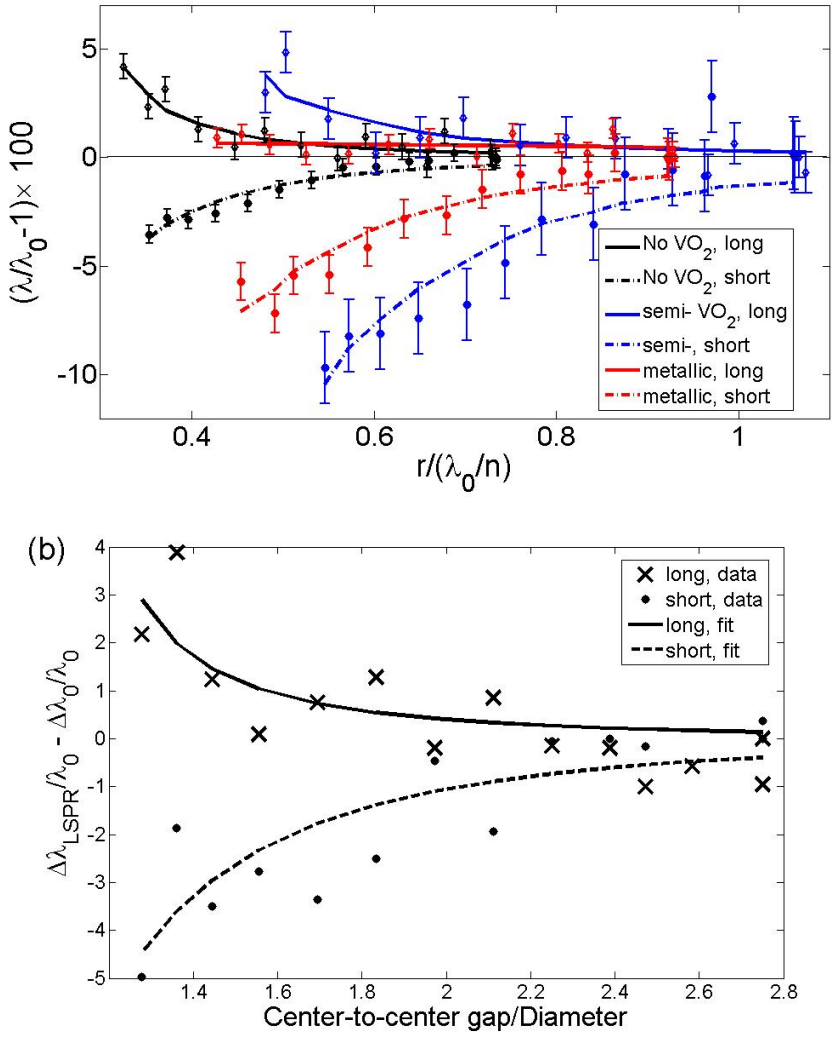

Figure 4.9: (a) The change of the LSPR $\Delta\lambda_{LSPR}$ normalized to the LSPR for the square array λ_0 versus ND spacing for the 180 nm particles. (b) The difference in wavelength shift from the square array due to the VO_2 phase transition as a function of particle spacing and fit. The fit parameters for (a) are found in Table 4.1.

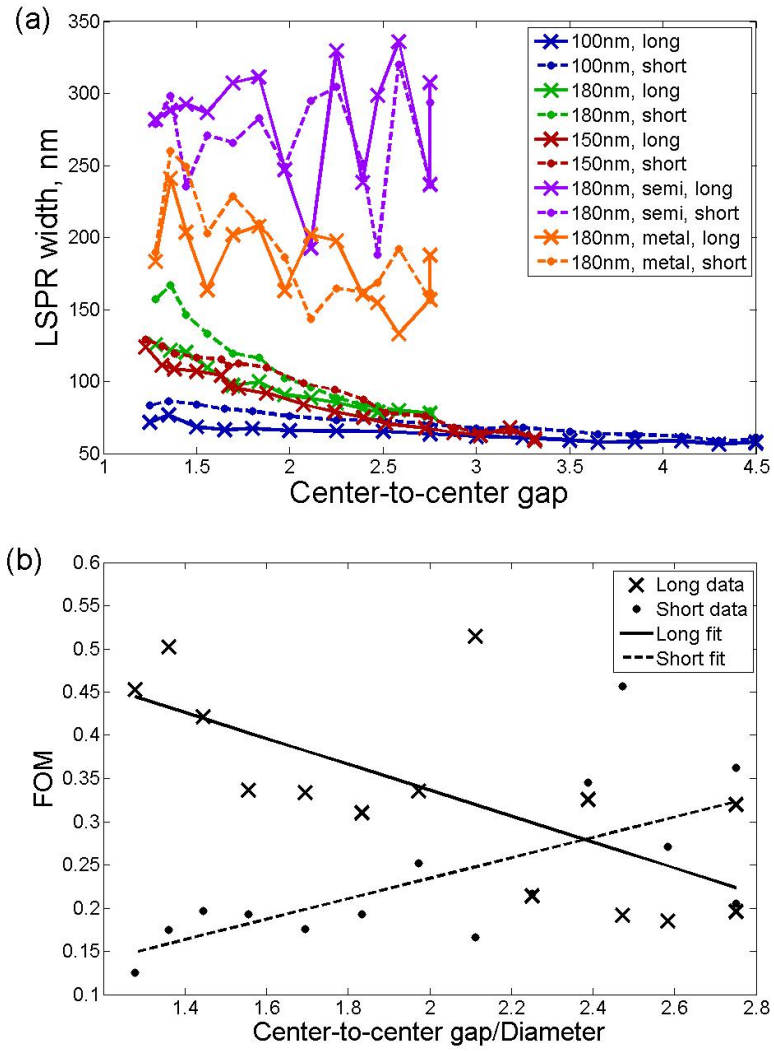

Figure 4.10: (a) The LSPR width for ND arrays. (b) The *FOM* for Au::VO_2 ND structures, as defined in (3.11).

increases for the long-axis mode and decreases for the short-axis mode. This means that as r increases, κ decreases for the long-axis mode and increases for the short-axis mode. Since the sensitivity of the LSPR to changes in ϵ'_m is proportional to κ, this reverse behavior between the long-axis and short-axis sensitivity to changes in dielectric function is expected.

Figure 4.10 shows the LSPR width as a function of r. For the particles in air, the full-width at half-maximum (FWHM) was measured directly from the data. However, for the NPs in VO_2, the full-width at 90% maximum (FW90M) was measured and the FWHM = 3×FW90M calculated as discussed in Chapter III. The presence of interband transitions leads to an LSPR width for the semiconducting Au::VO_2 structures that is nearly double that of the 180 nm NPs in air for the smallest gap. However, because of the increase in the shift in LSPR wavelength due to the VO_2 phase transition is achieved by decreasing the spacing between NDs, the improvement is approximately a factor 2 in the figure of merit FOM, as defined in (3.11). For both polarizations, the width of the LSPR increases with decreasing r. There are large variations in the LSPR width for the NDs in VO_2 film, possibly due to the increased error in determining the LSPR position and FW90M for these more damped NDs. The increased variations in FWHM for the NDs in VO_2 also leads to more variability in the FOM for these particles.

4.5 Conclusions

Interparticle interactions play an important role within NP arrays, and can include both near-field and far-field components. Not accounting for these interactions can be a major source of error when applying single-particle calculations to arrays of NPs. Rechberger *et al.* conducted a similar study focusing on lithographically prepared arrays of Au NPs in air, reporting ~ 0.03 fractional change in LSPR at $d = 1.25$ for both polarizations. This is consistent with our results. Jain *et al.* predicted increasing sensitivity to changes in ϵ_m for decreasing particle gap r based on an effective factor

$\kappa_e = 1 - L_e^{-1}$ and (1.6). Not only have we experimentally studied and confirmed this analysis, but we have extended it to include both polarization modes and ellipsiodal particles in an absorbing medium. For particles of different diameters, there is no significant change in LSPR dependence on r for the long axis. That is, each particle diameter shows a fractional change in LSPR of approximately 0.05 for the long-axis polarization. However, for the short-axis mode there are differences in sensitivity over a larger distance with an average maximum difference of approximately 0.04. This difference may be attributed to increased far-field coupling for short-axis modes.

For the arrays in air, the short-axis polarization retains sensitivity to changes in the gap for larger r since the coupling strength does not decrease as rapidly as for the long-axis mode. We extend the work of Jain *et al.* to the short-axis, showing that there is a far-field $1/r$ dependence that is not present for the long-axis mode. When the gap is normalized to the reduced LSPR wavelength, the difference in sensitivity to changes in the gap is even more pronounced, seen by extrapolating the VO_2 curves in Figure 4.9 to a normalized gap of 0.1. Again, this demonstrates far-field coupling as the near-field term rapidly decreases with r. The increased sensitivity of the short-axis mode at larger distances may allow applications to take advantage of the relatively larger gap to meet performance specifications where a high electric field in a small region is not necessary.

These results also suggest that applications reliant upon changes to ϵ_m to shift the LSPR should use the long-axis polarization mode. An interesting possibility would be to create a detection scheme using unpolarized incident light. Polarizers on the optical detector can help differentiate between polarization modes. A stimulus applied to a

Au::VO_2 ND structure resulting in a small shift in ϵ_m may be resolved by comparing shifts in both polarization states. For Au::VO_2 structures, any increase in sensitivity to changes in ϵ_m with decreasing r is accompanied by an increase in LSPR width. The resulting improvement to the FOM is still a factor 2. This suggests that using interparticle coupling as a means of increasing the FOM for Au::VO_2-based devices may be useful. However, the resonances are still highly damped by the VO_2 interband transitions, presenting a limitation to potential applications.

CHAPTER V

THERMODYNAMIC CONSIDERATIONS FOR GOLD::VANADIUM DIOXIDE STRUCTURES

Abstract

Lithographically prepared arrays of gold nanoparticles (NPs) of diameter 140 nm, 20 nm in height, and a 60 nm thick film of VO_2 were fabricated to study low-power laser induced transition characteristics of these hybrid structures. Transient absorption measurements were made using a mechanically shuttered 785 nm pump laser, corresponding to approximately the LSPR resonance of the Au NPs, and a 1550 nm CW probe. Results showed that the presence of Au NPs significantly lowers the threshold laser power required to induce the semiconducting to metal transition (SMT) by as much as 37% with a volumetric fraction of Au of 4.2%. Measurements on arrays of different grating constants (350 nm and 500 nm) support the hypothesis that the particles are acting as "nanoradiators" that increase the absorption and scattering of light within the film. The interband transitions of VO_2 dominate the absorption at 785 nm, and lead to increased damping of the LSPR in the NPs. This increased damping in the NPs contributes to the conversion of absorbed EM energy into thermal energy. Finite element modeling was performed to better understand the complex thermodynamics of the structure.

5.1 Introduction

Optically active nanocomposites (NCs) in which the semiconductor-to-metal transition (SMT) of vanadium dioxide (VO_2) alters the plasmonic response of embedded or adjacent silver (Ag) or gold (Au) nanostructures have recently been described in applications to sensors, optical elements, and memory elements.[12,16,17,20–22] It is known that Au::VO_2 structures exhibit high optical tunability[12–17,19,22,29,30] and can be used to increase the optical contrast over VO_2 thin films alone, especially at teraHertz frequencies in which the contrast between the semiconducting and metallic

dielectric function of VO_2 is greater than in the visible.[20] In these cases, a thermally induced SMT alters the dielectric environment of a metal nanostructure in contact with the VO_2 film, shifting the localized surface plasmon resonance (LSPR) of the metal and altering the optical response of the NC. There are, however, many applications in which *photochromic*, rather than thermochromic, regulation of a plasmonic response would be desirable, particularly if it could be accomplished with low-power lasers.

It is well known that the SMT in VO_2 films and nanoparticles (NPs) can be induced by ultrafast laser irradiation at high intensities; in this case, the initial response is a result of femtosecond band-gap renormalization.[80,81,87,88,93] In this case, the SMT occurs as a result of increased carrier-concentration ($\sim 5 \times 10^{21}/\mathrm{cm}^3$) in the conduction band at a threshold fluence of 7 $\mathrm{mJ/cm}^2$ at room temperature.[80] Hilton *et al.* investigated the temperature-dependent behavior of this photo-induced SMT and reported an expected lowering of the threshold fluence near the critical temperature T_c.[136] Subsequent cooling to the semiconducting state results from electron-phonon interactions on a sub-nanosecond time scale. Work by Lysenko *et al.* demonstrates that the photo-induced SMT dominates over thermal mechanisms at these ultrashort time-scales, though both electronic and thermal contributions play a role during relaxation of the film after the pulse.[94,137]

On the other hand, for low-power or long-pulse laser switching at photon energies above the VO_2 band-gap, a band-to-band electronic excitation drives the SMT by laser-induced heating from carrier-carrier and carrier-phonon interactions. In this case, relaxation to the semiconducting state occurs by all thermodynamic mechanisms

available to the VO_2 film, including interactions with the substrate or environment.[75] Low-power optical switching of VO_2 thin films has been recently demonstrated in the context of optical limiting, optical switching, and thermochromic windows.[72–75] Wang *et al.* investigated the optical limiting behavior of VO_2 using a 1.1 μm CW-laser at an intensity of 255 W/cm^2. The phase transition occurred in 200 ms and resulted in a maximum contrast of 60%.[73] Soltani *et al.* used a 980 nm CW-laser to pump 100 to 250 nm thick VO_2 films and probed the films at 1.55 μm. It was found that the power required to initiate the phase transition, the *critical pump laser power for transition* P_c, was between 18 and 23 mW; however, they did not provide a spot size for the beam.[74,75] Soltani and coworkers did not provide a beam spot size for their experiments.

Here, we demonstrate that embedding an array of Au nanoparticles in a VO_2 thin film at a volumetric concentration below 5% both (a) reduces the photochromic switching threshold by more than one third, and (b) reduces the time to complete the SMT by a factor of $\sim$5. This increased switching efficiency results from coupling of the LSPR to VO_2 interband transitions: the resulting plasmon damping increases the rate of laser heating of the film and compensates for energy loss to the substrate. First-principles analysis substantiate these conclusions. To our knowledge, the dynamical response of these structures under laser irradiation has not been measured. The increased damping of the LSPR resonance by the VO_2 interband transitions reduces the extinction of the particles while also converting EM energy absorbed by the plasmon into thermal energy lost to the film. We show that the presence of the Au NPs significantly reduces P_c by 37% for 140 nm diameter particles with a grating

constant of 350 nm and a volumetric packing fraction of 4.2%. Appendix B contains a version of this chapter submitted for publication to *Applied Physics Letters* with a more concise discussion of the physics found in this chapter.

5.2 Experimental Details

Two samples were used in this study. The first sample, denoted S1, consisted of arrays with dimensions of 0.5 mm on a side and 140 nm particles. The grating constant D of each array was 350 nm. The arrays were coated with a film of VO_2 of nominal thickness estimated to be 60 nm estimated from the number of laser shots during deposition and corroborated by profilometer measurements. As previously discussed, Figure 2.13 shows a contour map of the change in transmission across the area of the arrays. The map showed that the VO_2 varies in transmission by no more than $\pm 3\%$ in the region of the arrays. This indicates that the film coverage is uniform within the region of interest.

Figure 5.1a shows the LSPR resonance positions for these arrays in each VO_2 phase, taken as described in Sections 2.2.2 and 2.3.2. A second sample (S2) with 140 nm particles and $D = 500$ nm with side-length 250 μm was also fabricated. Although this array was too small for the pump and probe beam spot diameters, we present the results here for completion. Spectra for this array are shown in Figure 5.1b. In the following discussion, we shall primarily focus on the first sample unless otherwise noted. We will then compare S1 to S2 in order to understand the effects of changing the grating constant.

To gauge the quality of the VO_2 film, transmission hysteresis measurements were

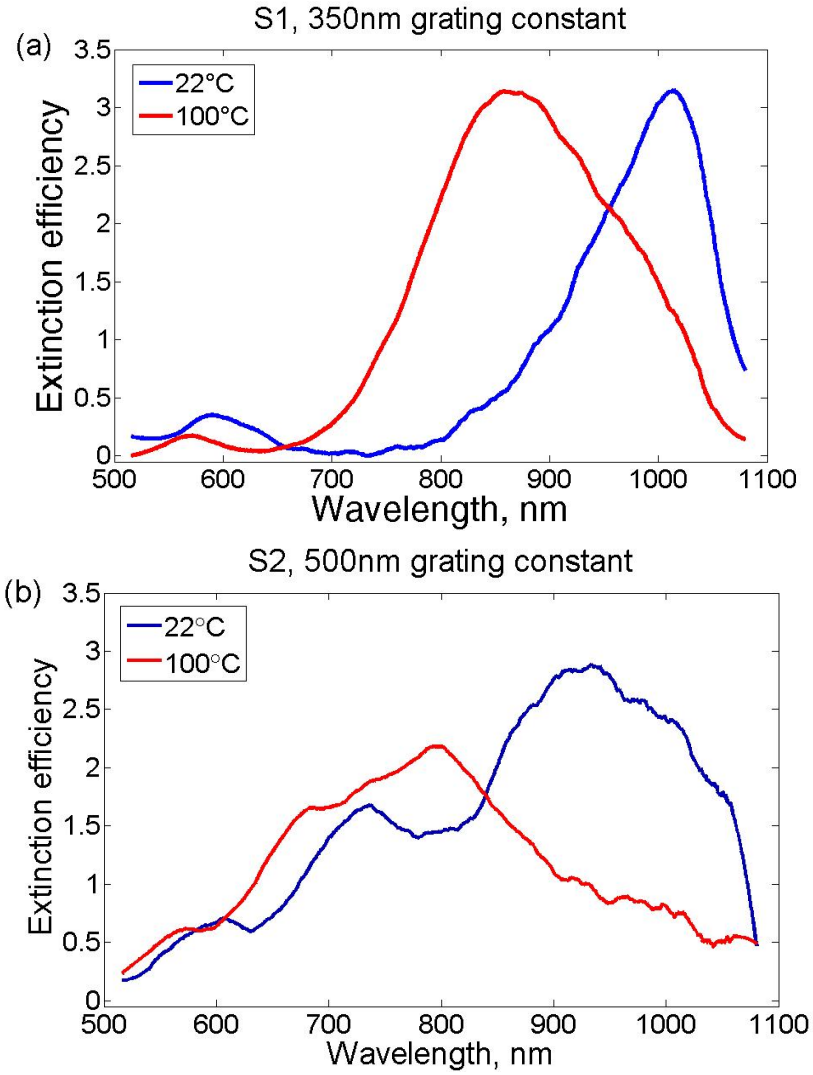

Figure 5.1: Extinction spectra for the (a) S1 and (b) S2 arrays. Note that LSPRs are blue-shifted when VO_2 transitions into its metallic state.

made on S1 and shown in Figure 5.2a. Note the more pronounced differences in the shape of the curves for the plain film and the Au::VO_2 structure. This is notably different than the transmission hysteresis curves shown in Figure 2.7, which only showed a change in optical contrast and not hysteresis shape; the difference is due to the higher areal packing fraction for this sample leading to stronger extinction from the array. The transmission hysteresis, taken with an InGaAs detector, is sensitive to NIR wavelengths. Figure 5.2b shows the integrated optical extinction hysteresis which is more sensitive to optical wavelengths than the InGaAs detector. It is clear from these results that the presence of the NPs is affecting the overall transmission through the film in the region of the LSPR. Also shown in Figure 5.2c is the transmission hysteresis at 785 nm as extracted from the extinction measurements. As the VO_2 switches, the film actually transmits more light. The LSPR of the arrays compensates for this increased transparency enough to lead to an overall decrease in transmission. This has a direct impact on the amount of heat absorbed in the film during laser irradiation.

The transient absorption measurements were made using the method and apparatus discussed in Section 2.3.1 and shown in Figure 2.9. The phase transition was induced by focusing a shuttered 785 nm heating (pump) beam with intensity I controlled by a variable neutral density filter; the SMT was monitored by a 1550 nm CW diode laser with intensity fixed at 18 W/cm^2. The heating and probe beams were normally incident about 10 mm apart on a 76 mm diameter glass lens with focal length 85 mm. The radii of the pump and probe beams at the focal spot were measured using a knife-edge technique to be 120$\pm$5 μm and 105$\pm$10 μm. The sample

was irradiated for 5.3 s, and allowed to recover completely between measurements.

Figure 5.3 shows the absorption coefficients for the film $\gamma_{\mathrm{film}}(T)$ and NC $\gamma_{\mathrm{NC}}(T)$, at 785 nm calculated from the transmission hysteresis shown in Figure 5.2c and measured reflectivity R_{semi} and R_{met} of semiconducting and metallic VO_2.[38] In a mean-field model, $R(T) = (1-f)R_{\mathrm{semi}} + fR_{\mathrm{met}}$, where $f(T)$ is the fraction of metallic VO_2 assuming a sigmoidal T-dependence with critical temperature $T_{\mathrm{c}} = 72°\mathrm{C}$. At low T, Figure 5.3 indicates that the NPs have only small absorption at 785 nm; calculations show that the 10% discrepency between film and array shown in Figure 5.3(c) can be accounted for by a difference $\Delta R_{\mathrm{semi}} = \pm 0.03$.

5.3 Results and Discussion

Contrast measurements of the 140 nm diameter NPs on S1 are shown in Figure 5.3 for the probe beam. Measurements were done at three different temperatures: 23°C, 55°C, and 75°C. Fifty-five degrees Celsius was chosen because initial measurements showed that it was the closest the sample could be held to the critical temperature and still recover the probe signal to its original level after laser irradiation. The data were smoothed using a an average over a moving window of 100 data points out of 5000 total (2%). The noise in the signal was approximately ±2% of the smoothed average. We defined a time t dependent normalized transmission, or contrast $C(t)$, of the probe to be the ratio of the measured transmission $\tau(t)$ to the initial transmission τ_0 taken before the pump was incident on the sample, (i.e., $t < 0$) for a given measurement.

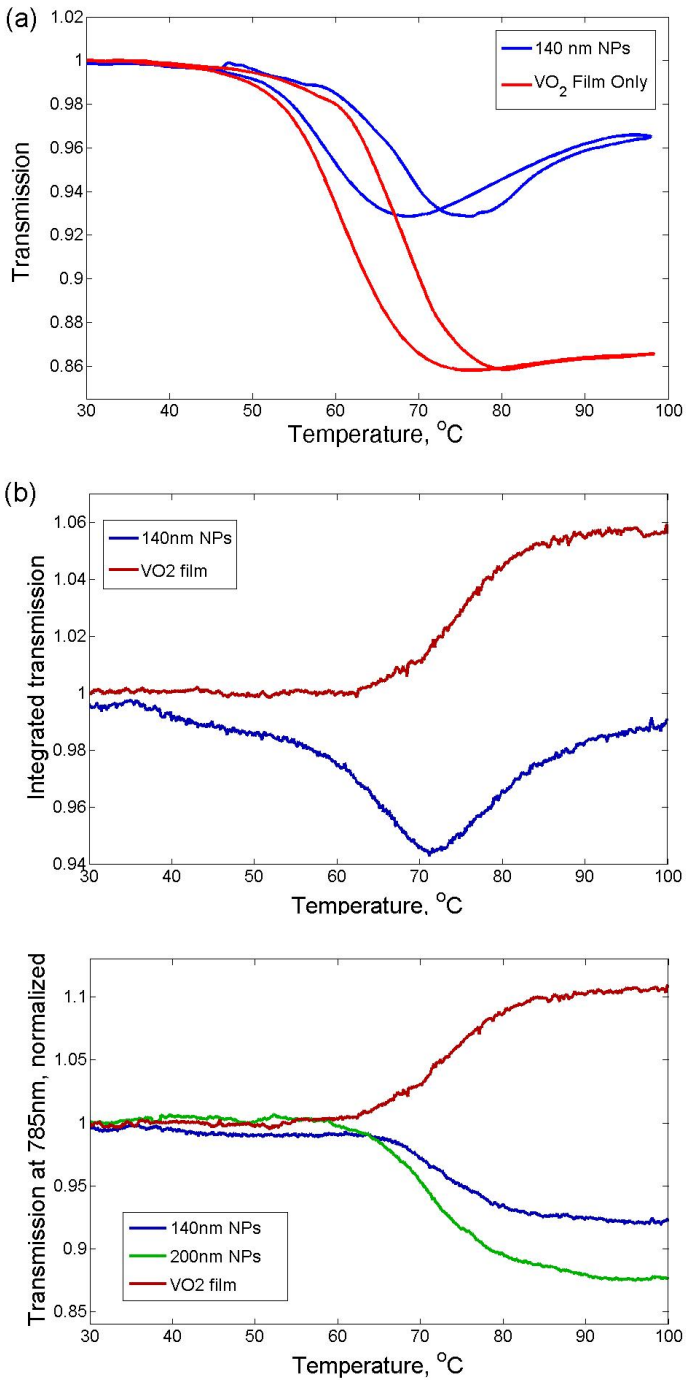

Figure 5.2: (a) Transmission hysteresis measurements of VO_2 film and VO_2 coated NP arrays from S1. The red curve represents the hysteresis of the VO_2 film, while the blue curve represents hysteresis measurements of the 140 nm diameter particles. Also shown are (b) the integrated extinction hysteresis and the (c) transmission hysteresis at 785 nm. In each case, the transmission is normalized to that of the VO_2 semiconducting state.

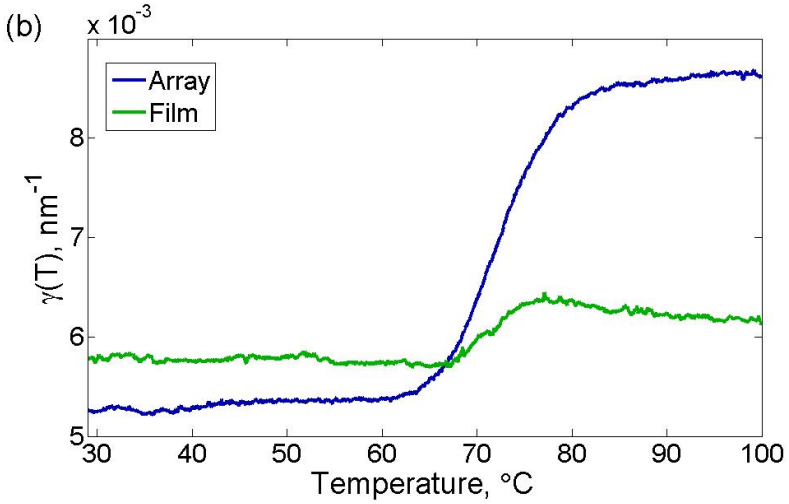

Figure 5.3: Estimated absorption coefficients at 785 nn for the NC and plain film structures.

That is,

$$C(t) \equiv \frac{\tau(t)}{\tau_0}. \tag{5.1}$$

This allowed us to measure changes in the transmission properties of the sample as the VO_2 undergoes the phase transition and to make comparisons at different laser powers. At $t = 0$, the decrease of the probe ($\lambda = 1550$ nm) transmission after the pump ($\lambda = 785$ nm) beam is triggered indicates that the film is switching to the metallic state. The transition took place over milliseconds, indicating that it is being driven thermally rather than optically; both the optical and electric field induced transitions are known to occur on a much faster time scale the thermally driven transition.[75,81,86]

At maximum I, when the shutter opens ($t = 0$), $C(t)$ decreases sharply as the laser drives the VO_2 toward the SMT; the VO_2 film takes $\sim$5 times as long to reach

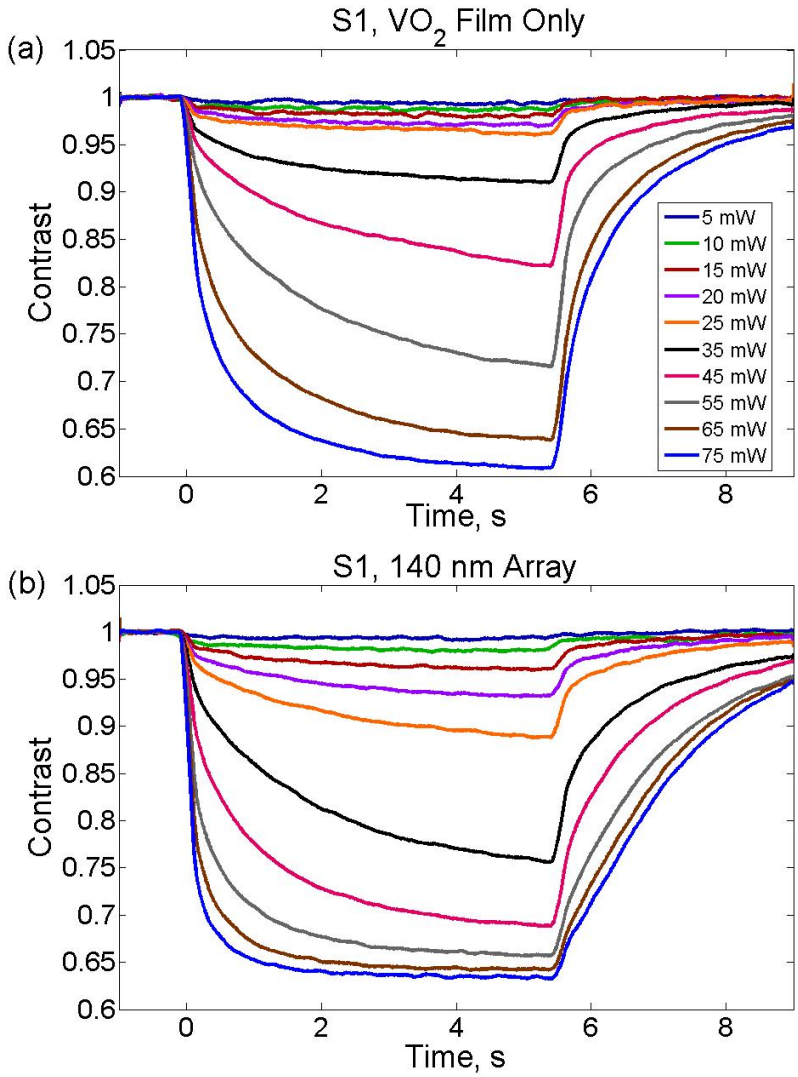

Figure 5.4: Typical transient contrast measurement for the 1550 nm probe beam (a) off and (b) on the 140 nm, NP array (S1) normalized to the initial transmission before the shutter of the pump is opened. The legend is the same for both plots.

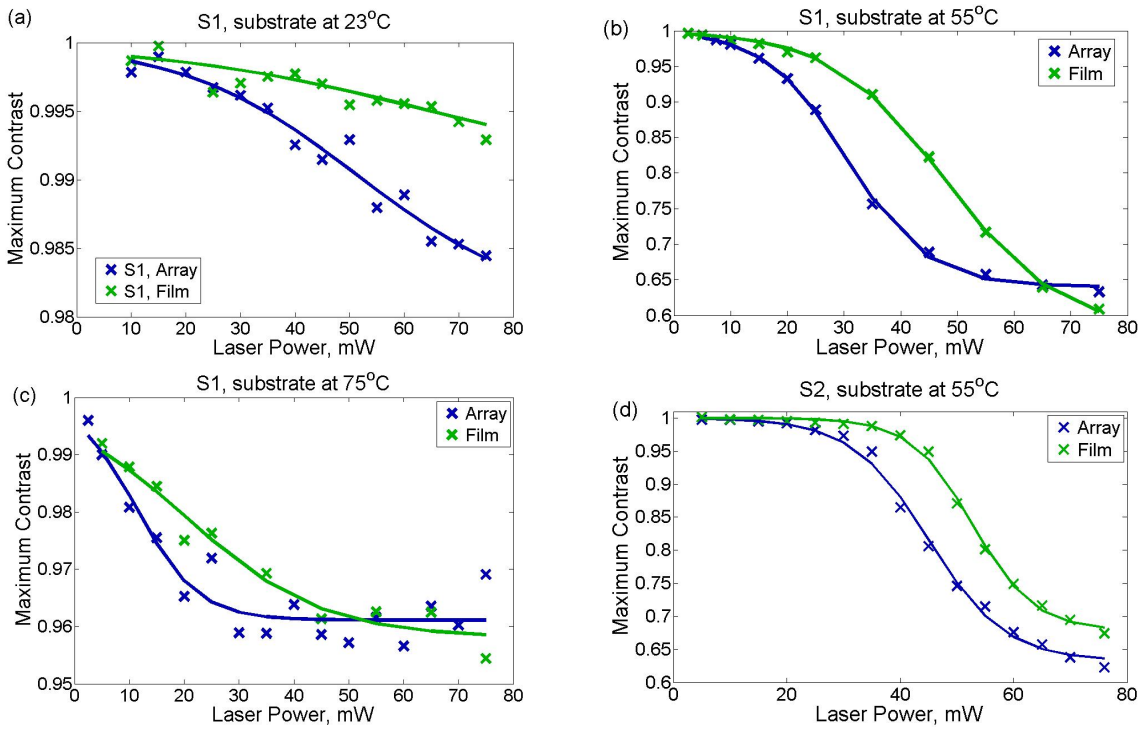

Figure 5.5: Maximum contrast $C_{\max}$ versus pump laser power corresponding to the transient absorption data for S1 at (a) $T = 23°C$, (b) 55°C, (b) 75°C, and (d) S2 at 55°C. Solid lines are fits to the data, but should only be taken as a guide for the eyes at temperatures other than 55°C. Error is calculated to be approximately the size of the data markers.

maximum contrast $C_{\max} \equiv C(5.3\text{ s})$ as the Au::VO_2 NC. Since Figure 5.3 shows that by 85°C the transition is essentially complete, Figure 5.4 suggests that at maximum I the NC reaches $T \approx 85°C$ at approximately 1 s, whereas the VO_2 film takes at least the full 5.3 s. Most of the change in contrast occurred in less than 500 ms, consistent with previous low-power switching studies.[72–75]

Figure 5.5 shows C_{m} as a function of pump laser power P. Errorbars were calculated from the variance of the $C(t)$ data to be approximately the size of the data markers in each figure. Note that the switching at room temperature was only about

1.5%. This is in sharp contrast with the Soltani work, which demonstrated switching at room temperature comparable to what we see at 55°C; however, direct comparisons are difficult without knowing the beam diameter used in their work.[74,75] At 75°C, we still see about 4% switching, which is expected since the fraction of the film that has transitioned at this point is approximately 75%.[88] Although all four plots in Figure 5.5 present fits to the data, the switching effect at substrate temperatures of 23°C and 75°C is smaller than the signal-to-noise ratio. Therefore, it is only the fit to the 55°C data that is discussed in the following paragraphs.

The dynamics of the NC and plain VO_2 film were analyzed by fitting $C_{\max}(I)$ with a three-parameter sigmoid similar to (2.1); that is,

$$C(P) = 1 - \frac{1 - C_{\mathrm{M}}}{1 + \exp\left[-\frac{P - P_{\mathrm{c}}}{P_{\mathrm{w}}}\right]}, \tag{5.2}$$

where P_{w} is the width of the transition and C_{M} is a fit parameter corresponding to the theoretical maximum contrast possible as the film transitions completely into the metallic state. The values of the fit parameters are recorded in Table 5.1. The effect of the NPs is to decrease P_{c} by approximately 37% and 15% for S1 and S2, respectively. Using the measured spot size, this suggests then the critical intensity decreases from $I_{\mathrm{c}} = 104$ W/cm^2 for the plain film to $I_{\mathrm{c}} = 66$ W/cm^2 for theAu::VO_2 NC. This is especially a significant difference considering the arrays had volumetric packing fractions of 4.2% and 2.1%. Similarly, I_{w} decreases by roughly the same factor for S1, from 21.9±1.3 W/cm^2 for the film to 15.5±1.3 W/cm^2 for the NC. The 4.2% volume fraction of Au NPs in the NC yields two key advantages over the

Table 5.1: Values of the fit parameters making up (5.2).

Sample	P_c, mW	P_w, mW	C_M
S1, Au::VO_2	30.43±0.86	7.132±0.616	0.6402±0.0082
S1, VO_2	47.96±0.95	10.07±0.59	0.5784±0.013
S2, Au::VO_2	44.96±1.25	6.808±0.998	0.6322±0.0162
S2, VO_2	52.74±0.78	5.429±0.614	0.6785±0.0114

plain VO_2: the NC (a) reaches $T_c \approx 72°C$ at 37% lower I_c and (b) exhibits increased sensitivity of $C(P)$ to changes in P during the SMT.

Numerical differentiation of $C(t)$ from Figure 5.4 shows that the maximum rate of change $\dot{C}_{max}$ occurs for $t \approx 0.1$ s. At that time, a thermodynamic tipping point has been reached: the thermal diffusion length $\sqrt{\alpha t}$ has reached approximately 100 μm, implying that the film-substrate system is then at the same T. As laser energy continues to be deposited into the system, both substrate and film rise in T at a slower rate; this is visible in both the NC and thin-film curves of Figure 5.4. The VO_2 continues to turn increasingly metallic until the system reaches steady-state T.

A plot of $\dot{C}_{max}(I)$ [Figure 5.6] shows that the values for $\dot{C}_{max}$ increase linearly at almost identical rates for the film and the NC up to their respective P_c, at which point $\dot{C}_{max}$ rises sharply for each. The sudden change in slope indicates that the system contains more metallic VO_2 than semiconducting, as one expects for $P > P_c$ determined from Figure 5.5(a). The near identical slopes for $\dot{C}_{max}$ before and after P_c suggest that the system is in equilibrium with the substrate, limiting the rise in T as expected.

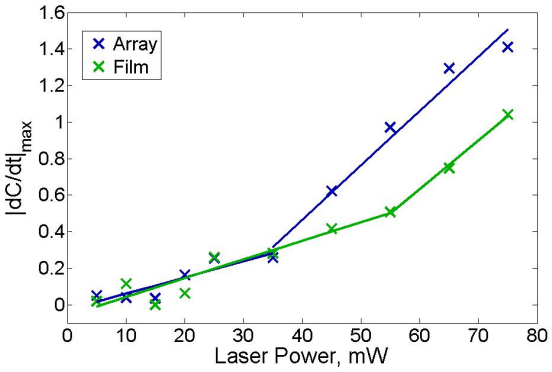

Figure 5.6: Maximum rate of contrast change $\dot{C}_{\max}$ as a function of power P with piecewise-linear fits.

5.3.1 Time Dependence of the Temperature

Finding the theoretical time dependence requires solving the heat-conduction equation with temperature dependent physical properties. However, the experimental data can be used to estimate $T(t)$ by inverting (2.1) and using the transient absorption data to provide the time dependence for $C(t)$. That is,

$$T(t) = T_{\mathrm{c}} - T_{\mathrm{w}} \ln \left[\frac{1 - C_{\max}}{1 - C(t)} - 1 \right]. \tag{5.3}$$

Using this technique, the maximum temperature rise in the film was estimated. Figure 5.7 shows $T_{\max}$ versus P plots for both S1 and S2. A linear fit was performed for S1, and the results recorded in Table 5.3. For S2, a piecewise linear fit was performed to account for the change in slope at approximately 35 mW. The significance of the fit is discussed in the next section.

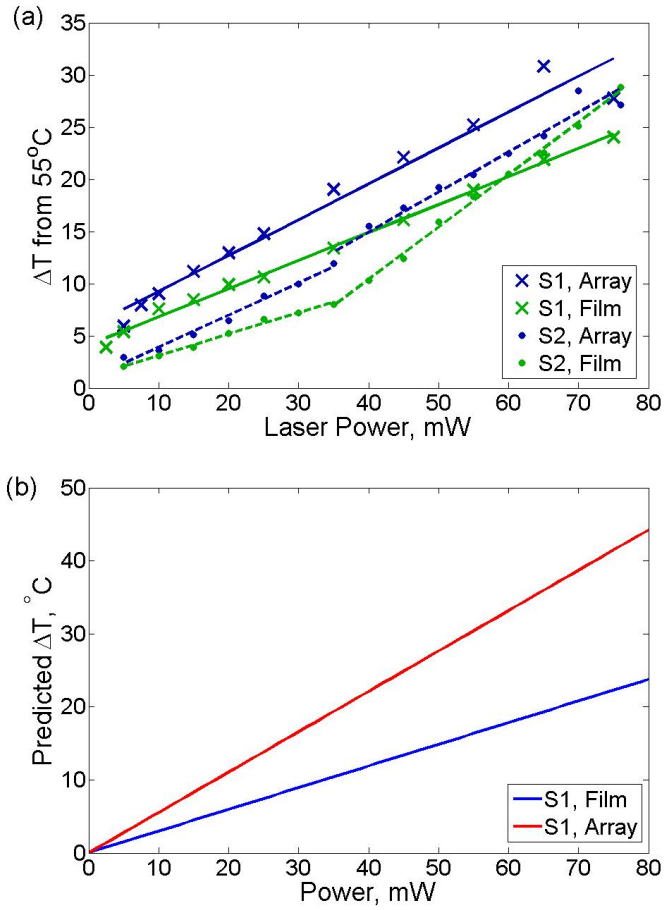

Figure 5.7: (a) The maximum change in temperature from 55°C versus pump laser power with linear fits. The blue curves are measurements on the array and the green are off of the array. The array with 350 nm grating constant is marked with 'x' and the 500 nm grating constant with '•'. (b) The predicted change in temperature for S1 based on analytical theory.

5.3.2 Theoretical Discussion I

To understand these results, we must consider the thermodynamics associated with the interaction between the laser and the film. A first-principles calculation requires solving the heat-conduction equation with temperature dependent physical constants and will be addressed in Section 5.3.3. Here we present a first-order treatment of the thermodynamics involved in laser-heating of the film. To simplify the discussion, we first consider the properties of the VO_2 only in the semiconducting state. Upon irradiation, the film absorbs energy at a rate per unit volume given by

$$q(x, y, z, t) = (1 - R)\gamma I(x, y, t)e^{-\gamma z}, \tag{5.4}$$

where R is the reflection coefficient between air and VO_2, $I(x, y, t)$ is the intensity profile of the laser, γ is the absorption coefficient of the film, and $z > 0$ is the position within the film.[123] The absorption in the glass is negligible compared to the VO_2 making it reasonable to assume that all of the energy used to heat the film and substrate is from absorption within the film. The pump beam is approximately at normal incidence ($< 5°$). The relevant optical and thermal material parameters for VO_2 and glass in are summarized in Table 5.2.

Table 5.2: The optical and thermal properties of VO_2 and glass. References [25, 94] were used for VO_2 properties and the Delta Glass material data sheet was used for glass. Calculated values were done following reference [123]. Values are for semiconducting VO_2 unless otherwise noted. The optical constants of VO_2 are cited for $\lambda = 785$ nm and given according to Verleur from reference [38] and the estimated values from Figure 5.3.

		Glass	VO_2 (Semi.)	VO_2 (Metal)
Heat Capacity	c_p [mJ/(g K)]	840	656	—
Thermal Conductivity	κ [mW/(cm K)]	11	65	—
Density	ρ [g/cm^3]	2.54	4.65	—
Enthalpy of Transition	ΔH [mJ/cm^3]	—	1.85×10^5	
Absorption Depth (Verleur)	$d_{ab} = 1/\gamma$ [nm]	—	150	82.8
Absorption Depth (Measured, film)		—	175	161
Absorption Depth (Measured, array)		—	188	116
Reflectivity, glass:VO_2 (Verleur)	R	—	0.108	
Reflectivity, air:VO_2 (Verleur)		—	0.25	0.16
Thermal Diffusivity	$\alpha = \frac{\kappa}{c_p \rho}$ [cm^2/s]	5.2×10^{-3}	21.3×10^{-3}	—
Thermal Penetration Depth	$d_{th} = \sqrt{\alpha t_{pulse}}$ [cm]	0.1612	0.3263	—
Thermal Confinement Time (Verleur)	$t_{th} = d_{ab}^2/\alpha$ [ns]	—	11	3.2

For VO_2, the ratio $d_{ab}/d_{th} \sim 10^{-5}$ indicates that the volume of the heated VO_2 is much greater than the volume in which laser absorption takes place.[123] The same can be said for the volume of glass that is affected by the deposited thermal energy. Assuming that little thermal resistance exists between the film and the substrate, the majority of the energy goes into heating the glass. Estimates of the effect of thermal resistance show an approximately 5°C gradient between the film and glass. Since the radius of the laser spot is small compared to d_{th} for both glass and VO_2, we can essentially treat the laser as a point source. The effective radius of the heat-affected volume r_{th} is then d_{th}, thus making the effective volume of the heated hemisphere $V_{eff} = \frac{2}{3}\pi r_{th}^3 = 8.6 \times 10^{-3}$ cm^3 in the glass. For the thin VO_2 film, the effective volume is effectively cylindrical and $V_{eff,\ film} = 2.1 \times 10^{-6}$ cm^3.[123] The orders of magnitude disparity between the effective volumes signifies that the VO_2 stays in thermal equilibrium with the glass on the time scales that we are observing. For the volume of VO_2 affected by the laser, the energy needed to complete the phase transition in the affected volume of VO_2 Q_{tr} is 0.389 mJ compared to the 146.4 mJ needed to raise the temperature of the affected volume of glass by 1°C and 6.4×10^{-3} mJ needed to raise the volume of VO_2 by 1°C. This suggests that most of the heat is being transported into the glass substrate by conduction before the laser is shuttered. Considering that the thermal confinement time of VO_2 is on the order of nanoseconds, it is reasonable to conclude that the film is in thermal equilibrium with the heated volume of the substrate.

Volume and time integration of (5.4) yields

$$Q_{\text{total}} = (1 - R_{\text{air}}) \left(1 - e^{-\gamma z_0}\right) t_{\text{pulse}} P_0, \tag{5.5}$$

where z_0 is the thickness of the VO_2, t_{pulse} is the duration of the laser irradiation, and P_0 is the laser power. In (5.5), the reflections from the VO_2:glass interface back into the VO_2 is assumed to be minimum. Accounting for the first reflection from the surface of the glass, (5.5) becomes

$$Q_{\text{total}} = \left(1 - R_{\text{air}} + R_{\text{glass}} e^{-\gamma z_0}\right) \left(1 - e^{-\gamma z_0}\right) t_{\text{pulse}} P_0. \tag{5.6}$$

Using the Verleur optical constants, the additional term contributes an extra 7% to the heat absorbed, with subsequent reflections contributing less. This correction is small compared to the uncertainly in physical parameters, such as the absorption constant of VO_2. Using (5.5) and assuming that the glass and VO_2 are at approximately at the same temperature, the estimated average temperature rise in the system is 5°C over the effective volume of the glass. Ignoring the substrate and assuming that all of the energy goes into raising the temperature of the film, the average temperature is over 14000°C. This clearly indicates that transport of heat into the substrate must be taken into account, and the temperature distribution over the affected volume is needed to determine the maximum temperature in the film.

It can be shown that for an semi-infinite solid ($z > 0$) with constant heat flux q through a circular region of radius a located at $z = 0$, the temperature rise ΔT is

given by

$$\Delta T = \frac{aq}{2\kappa} \int_0^\infty J_0(\lambda r)\, J_1(\lambda a)\, F(z,t)\, \frac{d\lambda}{\lambda}, \tag{5.7}$$

$$F(z,t) = e^{-\lambda z}\mathrm{erfc}\left[\frac{z}{2(\alpha t)^{\frac{1}{2}}} - \lambda(\alpha t)^{\frac{1}{2}}\right] - e^{\lambda z}\mathrm{erfc}\left[\frac{z}{2(\alpha t)^{\frac{1}{2}}} + \lambda(\alpha t)^{\frac{1}{2}}\right], \tag{5.8}$$

where J_0 and J_1 are Bessel functions and erfc is the complementary error function.[138] The contrast curves in Figure 5.4 have approximately reached the steady-state temperature, allowing the solution to be simplified. In the steady state, (5.7) reduces to

$$\Delta T = \frac{qa}{\kappa} \int_0^\infty e^{-\lambda z} J_0(\lambda r)\, J_1(\lambda a)\, \frac{d\lambda}{\lambda}. \tag{5.9}$$

Furthermore, the average temperature change $\Delta\bar{T}$ over the laser spot is

$$\Delta\bar{T} = \frac{8qa}{3\pi\kappa}. \tag{5.10}$$

From (5.5), the total energy absorbed in the film is linear with power P_0. By (5.10) this implies that the maximum temperature can be parameterized as

$$T \approx T_0 + A_{\mathrm{th}} P_0, \tag{5.11}$$

where

$$A_{\mathrm{th}} = \frac{8}{3\pi\kappa} \frac{(1 - R_{\mathrm{air}})(1 - e^{-\gamma z_0})}{\pi a}. \tag{5.12}$$

In this first-order approximation, A_{th} is constant. In reality, however, A_{th} varies with temperature since the physical parameters change with T, as is evident in the slope

change seen in the data for S2 in Figure 5.7 at approximately 35 mW. For both S1 and S2, the arrays show an increased slope compared to the plain film in Figure 5.7, as expected, below 35 mW. In the case of S1, the array has a 26% higher slope than the film alone. Interestingly, S2 shows a 48% increase in sensitivity on the array than the plain film, despite having a lower packing fraction than the former sample. However, at higher laser powers, the S2 array demonstrates a lower slope to changes in power than the film alone. Figure 5.7 also shows the predicted change in temperature for S1 using (5.12).

As mentioned, (5.2) is identical in form to (2.1). Setting the arguments in the exponent of each equation equal and inserting (5.11), we can connect the parameters of each fit, leading to

$$P_{\mathrm{w}} = \frac{T_{\mathrm{w}}}{A_{\mathrm{th}}} \tag{5.13}$$

and

$$P_{\mathrm{c}} = \frac{T_{\mathrm{c}} - T_0}{A_{\mathrm{th}}}. \tag{5.14}$$

Therefore, both P_{w} and P_{c} are inversely proportional to the absorption due to the film.

As discussed in Section 2.3.2, the presence of the Au NP array not only leads to absorption and scattering of the incident radiation, the scattering also increases the light absorbed by the embedding medium. Our definition of extinction in absorbing media accounts for this phenomenon. We define an effective absorption constant $\gamma_{\mathrm{eff}} \equiv \gamma_{\mathrm{film}} + \rho_{\mathrm{NP}} C_{\mathrm{e}}$ where ρ_{NP} and C_{e} are the particle number density and extinction cross-sections, respectively. Using γ_{eff} the difference between P_{c} on the array and on

the plain film can be quantified by taking the ratio ξ and simplifying to get

$$\xi = \frac{P_{\mathrm{c}}^{\mathrm{NP}}}{P_{\mathrm{c}}^{\mathrm{film}}} = \frac{A_{\mathrm{th}}^{\mathrm{film}}}{A_{\mathrm{th}}^{\mathrm{NP}}} = \frac{1 - e^{-\gamma_{\mathrm{film}} z_0}}{1 - e^{-\gamma_{\mathrm{eff}} z_0}}, \tag{5.15}$$

where the superscript NP is used to indicate that we are taking the measurement on the array.

A theoretical calculation of A_{th} using the values in Table 5.2 and the measured d_{abs} gives predictions of 0.50 for VO_2 only and 0.55 for the Au::VO_2 structure using the estimated absorption constants. This was done to account for the switching of the Au NPs. These numbers are higher than the experimentally measured fit values recorded in Table 5.3. This discrepency is probably due to overestimating the extinction efficiency by averaging between the VO_2 semiconducting and metallic states. Although, the formalae derived here allows us to understand the relationship between substrate, film, and array, to make accurate predictions one must take into account the effect of the phase transition on the absorption properties. Figure 5.8 plots the predicted temperature rise with time from (5.7) for $I = 76$ W/cm^2 (P =35 mW). Clearly the temperature rises faster and to a higher steady state than the experiment, as expected by $A_{\mathrm{th}} > A_{\mathrm{fit}}$.

Table 5.3: Values of the fit parameters making up (5.11). Numbers in parenthesis represent the fit at higher laser power for the second sample.

Sample	A_{fit} [°C/mW]	A_{th}	$T_{0,\text{fit}}$, °C
S1, Au::VO_2	0.34±0.05	0.54	60.8±2.04
S1, VO_2	0.27±0.01	0.30	59.1±0.52
S2, Au::VO_2	0.31±0.04 (0.38±0.07)	0.43	55.8±1.0 (54.6±3.8)
S2, VO_2	0.21±0.02 (0.50±0.02)	0.30	56.0±0.5 (45.3±1.3)

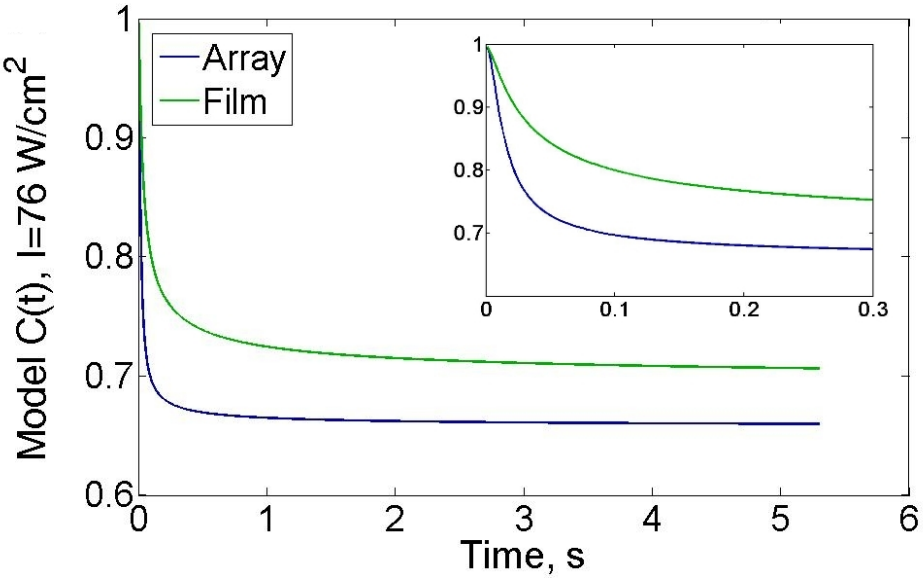

Figure 5.8: Calculated contrast as a function of time for the plain film and NC cases using (5.7) for $P = 35$ mW. The inset shows the a magnified view of the time dynamics.

5.3.3 Theoretical Discussion II: Temperature Dependent Properties

To account for the phase transition, the temperature dependent optical properties must be used in (5.4). Upon integration of the volume, we have

$$Q(t) = P_0 \int_0^t (1 - R_{\text{air}}(T)) \left(1 - e^{-\gamma(T) z_0}\right) dt, \tag{5.16}$$

where T is also function of time. We can assume that relevant physical constants R_{air} and γ have a temperature dependence proportional to the fraction $f(T)$ of VO_2 that has switched to the metallic state. For example,

$$\gamma(T) = (1 - f(T))\gamma_{\text{semi}} + f(T)\gamma_{\text{metal}}, \tag{5.17}$$

where we have denoted the appropriate VO_2 state with the subscripts. This leads to a more complicated relationship between $T_{\max}$ and P_0. Since the absorption within the VO_2 or the 140 nm diameter NP Au::VO_2 structure both increase as the film becomes metallic, an increase in slope of the curve is expected. This can explain the slope change seen in the S2 data. However, the data for S1 does not appear to exhibit the same change in slope near the phase transition. Due to the additional complexity of accounting for the phase change, simulations using COMSOL Multiphyics® were conducted.

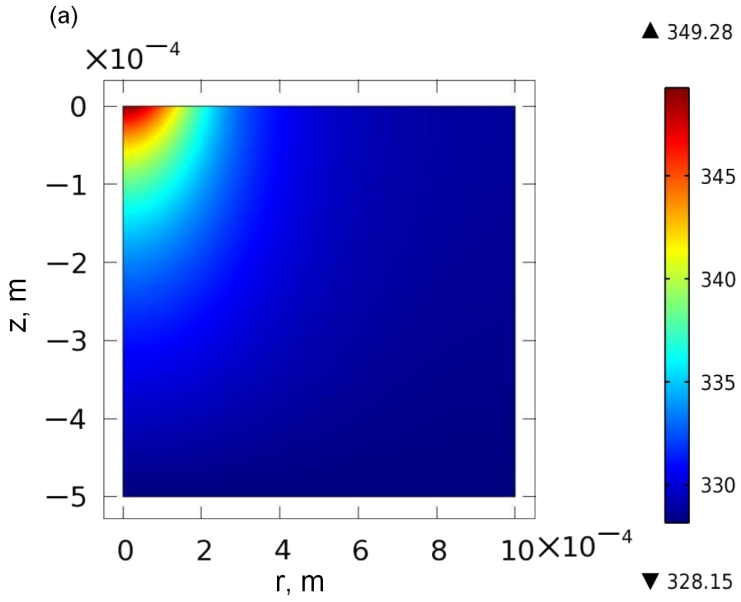

Figure 5.9: Simulations show that for a 121 μm radius spot size, 75 mW of incident power, and the measured optical constants of VO_2, a maximum temperature of 76°C and significant heating of the substrate occurs after 5.3 s.

5.4 COMSOL Simulations

To calculate the temperature distribution and maximum temperature in the VO_2 film, COMSOL Multiphysics® was used to solve the 3D heat equation subject to the appropriate boundary conditions; the simulation details were discussed in Section 2.4.2. The phase transition was accounted for by temperature dependent optical constants, such as (5.17). This is justified since the energy needed to induce the phase transition is small compared to the energy needed to increase the temperature in the affected volume of glass. The simulated beam radius was 121μm.

As can be seen in Figure 5.9, the temperature rise calculated by COMSOL is 67°C and smaller than what we expect from experimental data. Reducing the mesh and

adding convective cooling to the boundary at $x = 0$ had no significant effect on the maximum temperature. The discrepancy is likely due to a higher absorption constant in the VO_2 than estimated. Figure 5.10 shows the effect of changing the absorption constant d_{ab} Figure 5.10a), reflectivity R (5.10b), and the laser spot size a (5.10c) calculated from analytical theory. The measurement of the spot size had a standard deviation from a linear trend of 2.25 μm, which is not enough to significantly change the temperature. Large variations of reflectivity only change the temperature by, at most, 6°C. On the other hand, changes in the absorption constant can lead to large variations in temperature. The important thing to note from the simulations is that significant heat is transported into the substrate. Increasing the efficiency of laser heating can be achieved by increasing the thickness of the film. Although this increases the amount energy needed to switch the VO_2, it also compensates for the amount of energy absorbed by the substrate.

Figure 5.11 shows the maximum temperature calculated with COMSOL as a function of laser power. There is a notable change in slope once the temperature reaches approximately 63°C This slope change occurs at the same temperature as the change in slope for S2, and apparently is due to the changing absorption properties in the film as a result of the SMT. Although it is not as obvious, there is a change in slope present in the S1 data at about the same temperature.

5.5 Conclusions

The presence of Au NPs within the VO_2 film leads to an increase in sensitivity to low-power laser irradiation over the VO_2 film alone by increasing the heat absorbed

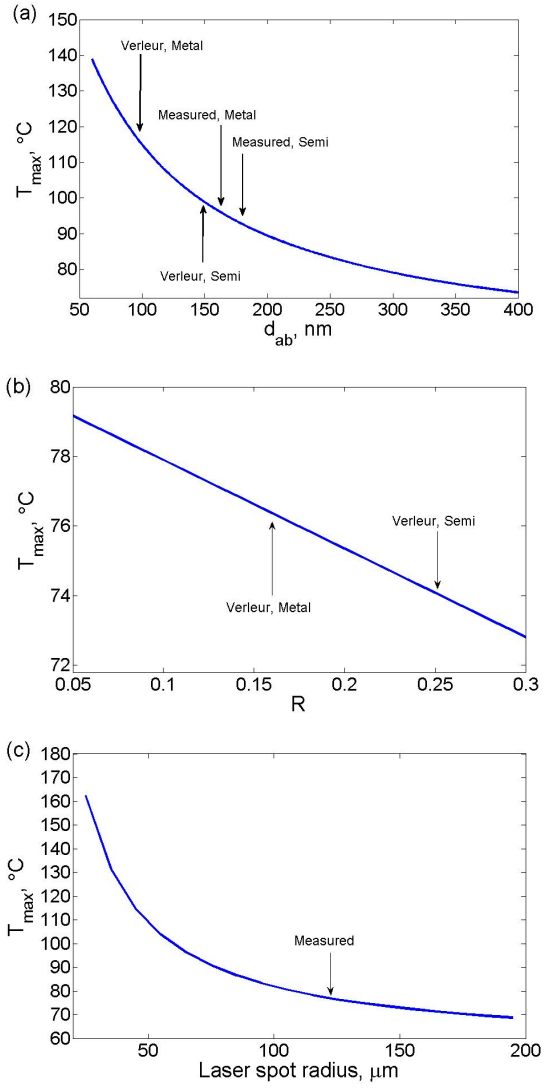

Figure 5.10: By varying the physical parameters (a) d_{ab}, (b) R, and (c) a, the effect of the maximum temperature can be seen.

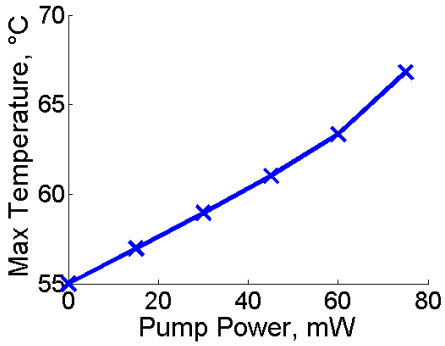

Figure 5.11: The maximum temperature versus power calculated using COMSOL Multiphysics®.

in the system; this result, though never studied for Au::VO_2 structures, is consistent with the literature.[40,41] Although nearly all of the laser absorption took place within the thin film, the substrate played a crucial role in determining the thermodynamics. Most of the heat was quickly transported into the substrate and lowered the available energy for the phase transition. To fully take advantage of the relatively low thermal energy needed to switch a VO_2 thin film, the thermal resistance between the film and substrate should be increased. Our results also show that when designing VO_2 and Au::VO_2 structures for applications, not only does the thickness of the film need to be optimized to account for optical specifications, but also for thermal considerations. In this regard, considering the electron injection behavior of nano-junctures of VO_2 and Au as reported by Xu *et al.*,[15] nano-patterned VO_2 structures and Au NPs present an interesting possibility for improving the performance of a device which relies on the thermochromic behavior of VO_2 by reducing the threshold power for transition. These same structures may also present interesting results concerning their photochromic

behavior; further studies should include ultra-fast pump-probe measurements.

The interband transitions within the $3d_{||}$ band are responsible for absorption in the VO_2 at 785 nm. These transitions also damp the Au LSPR by dissipating the energy of the plasmon into thermal energy in the film. This directly leads to the difference between the temperature maximum on the array and the plain film. One way to corroborate this is to pump the sample at wavelengths far above the LSPR resonance.

CHAPTER VI

CONCLUSIONS AND FUTURE DIRECTIONS

In the previous chapters, we have focused on the EM interactions within Au::VO_2 array structures; on the other hand, much of the literature concentrates on the tunability of the hybrid structure and its applications as reviewed in Chapter I. Within this geometry and at wavelengths below the bandgap of VO_2, the interband transitions of VO_2 played a central role in determining the properties of the LSPR. There were several significant findings in our results, but also several questions were raised. In the following pages, we will discuss the implications of this work for understanding Au::VO_2 structures within the larger context of nanoplasmonics.

6.1 Nanoantennas: Probing the Phase Transition

As discussed in Chapter III, the LSPR is highly sensitive to the dielectric properties of the surrounding medium and can serve as a probe of the phase transition. The change in the real part of the VO_2 dielectric function upon phase transition blueshifts the LSPR by hundreds of nanometers and is the primary reason for interest in Au::VO_2 structures. Changes to the imaginary part of the dielectric function lead to changes in the width of the LSPR. The array geometry is ideal for studying the homogeneous broadening of the LSPR as it minimizes the differences between particles. We have shown that the LSPR is highly sensitive to changes in the imaginary part of the VO_2 dielectric function. Also, we have demonstrated how particles

resonant between 800 and 1000 nm can be used to probe the changes in the split *d*-bands during the phase transition.

An interesting possibility for future experiments would be to use Au particles with radii smaller than 20 nm to increase the sensitivity of the LSPR to chemical interface damping. Alternatively, probing the arrays described in Chapter III at non-normal incidence would excite the plasmon along the 20 nm axis of the particle. In this size regime, the mean free path of the Au electron oscillation is the same size or larger than the radius of the particle, and the interactions with the interface lead to additional broadening of the resonance. The report by Xu *et al.* showing that Au-VO_2 nanojunctures exhibited a decreased transition temperature, which they explained by an electron injection mechanism, suggests interesting interactions within nanostructures of this size.[15] The measurements described in Chapter III demonstrate that Au NPs can be used to probe the structure of the dielectric function resulting from particular electronic transitions of VO_2. Probing the VO_2 phase transition through chemical interface damping may be a way to directly measure changes to the local dielectric properties of VO_2 that would go beyond those predicted by effective medium models that use bulk dielectric functions.

6.2 Nanodimers: Plasmonic Interactions in VO_2

In Chapter IV we discussed interactions between Au NPs and the VO_2, where we extended the derivation by Jain *et al.* to include ellipsoids and short axis polarization. Interactions between particles with polarization along the short axis proved to retain sensitivity to changes in dielectric function and interparticle spacing at larger

distances than the long-axis modes. Near-field particle interactions in absorbing media have not been as thoroughly studied as interactions in non-absorbing media, and future experiments with trimers (three coupled particles) and chains of particles may lead to interesting behavior within Au::VO_2 structures. The field-enhancement on the surface of nanostructures has been shown to be reduced when the structure was embedded an absorbing medium.[133] However, the phase transition of VO_2 may be used to modulate the field enhancement magnitude and resonant wavelength, especially for strongly coupled NDs; this modulation may allow the gain curve of surface-enhanced plasmon based sensors to be thermally tuned.

The analysis performed in Chapter IV did not account for intermediate and far-field interactions within the array structure. The effect of the complex wavenumber k in (4.13) and (4.14) on far-field coupling within an array has not been addressed in the literature. Complex wavenumbers are also present in gain media, which have have been investigated as a way to amplify plasmon properties, such as the propagation length of surface plasmons.[139–141] Understanding the coupling between plasmonic nanostructures embedded in absorbing and gain media may have important consequences for future applications.

Recent work by Sheikholeslami *et al.* has shown that in heterodimer configurations consisting of particles of different sizes or composition the optically dark, anti-binding modes discussed in Chapter IV can be excited. Furthermore, in ND structures consisting of a one Ag and one Au particle, coupling between the Ag plasmon and Au interband transitions lead to an anomalous shift in resonance wavelength for the system that is not accounted for in free-electron hybridization models.[142] A

similar experiment can be performed using a modified Au::VO_2 structure; an optically transparent medium, such as SiO_2, can be used as a spacer to create a heterodimer structure consisting of vertically stacked Au and VO_2 NPs.

6.3 Nanoradiators: Plasmonic Enhanced Low-Power Photochromism of VO_2

The results presented in Chapter V have important consequences for many applications, such as VO_2 bolometers and calorimeters, optical limiting, and protective coatings for sensors.[20,71–73,75] Structures designed to take advantage of the switching behavior of VO_2 can also take advantage of the resonant extinction of the particles to increase the sensitivity of the structure to laser irradiation of a particular wavelength. In this work, the 140 nm particles were not resonant with the laser while the VO_2 was in the semiconducting state. As the film heated up, the particles became more efficient absorbers. Alternatively, structures can be designed that show decreasing absorption in the metallic state at a particular wavelength. This thermal regulating of the transmission may become the basis for several applications of smart materials.[30]

The presence of the Au NP array increased the light absorbed within the Au::VO_2 structure. This decreased the laser intensity required to heat the film by as much as 37% in our samples, which can be useful for optical limiting and switching applications designed to operate at specific wavelengths. What has not been tested is the effect of the Au::VO_2 structure on ultrafast optical switching of VO_2. These structures can contribute to the optically induced SMT in two ways. First, the Au NPs can raise the temperature of the surrounding VO_2 and lower the critical fluence. Second, the ultrafast pulse may contribute to inducing the SMT by temporarily injecting electrons

into the surrounding material on a time scale of less than 10 fs, corresponding to the plasmon dephasing time, especially in particles small enough to experience chemical interface damping. This increase in carrier concentration on the time scale of the phase transition may change the dynamics of the transition. Ultrafast experiments with Au::VO_2 structures with LSPR near 800 nm would directly interrogate the interaction between the plasmon and the split 3*d*-bands. Furthermore, by pumping the system with a laser at wavelengths on and off the LSPR resonance in either state or by tuning the LSPR to coincide with different transition bands, a wide range of configurations can be tested.

6.4 Optical Properties of the Composite Structure

In Section 2.3.2 we discussed the concept of extinction in an absorbing medium. Light scattered into the medium by the NPs experienced a longer path-length through the absorbing material than it would if the NPs were not there; the definition of extinction discussed in Chapter II accounts for this. Figures 1.1 and 4.3 show that coating 180 nm particle arrays with VO_2 reduces the extinction efficiency of the particles by roughly a factor of 3, which presents a challenge that must be overcome for applications that rely on strong plasmonic absorption. For such applications of Au::VO_2 structures at wavelengths below 1500 nm, it is often desirable to maximize the contrast C, defined as the ratio of transmission in the high-temperature state to that of the low-temperature state. Figure 6.1 shows the spectroscopic contrast at each wavelength for VO_2 film, the 180 nm particle array, and the 100 nm particle array described in Chapter III. With this definition, a contrast greater than 1 allows

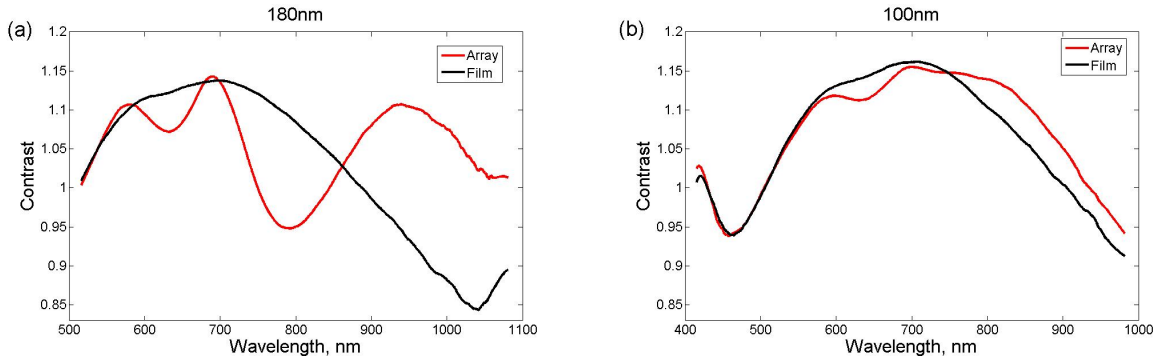

Figure 6.1: Contrast spectra, defined as the transmission at temperature T divided by transmission at room temperature, for (a) 180 nm particle array and the (b) 100 nm particle array.

more light to transmit through the sample in the high-temperature state. Note that the measurements were made at two different center wavelengths for each structure. For comparison, the VO_2 contrast is also shown for both center wavelengths.

The most striking feature of the VO_2 contrast is that between approximately 500 nm and 900 nm the film actually has increased transmission in the metallic state compared to the semiconducting state; note the isosbestic point at 900 nm and discussed in Section 1.4.2.[82,104] If we are to design a structure that can selectively block light of a particular wavelength within this band for metallic VO_2, then we not only must design nanostructures with a high temperature LSPR at this wavelength, the extinction must be high enough to overcome the increased transmission of the VO_2 film. This is easily understood by considering Beer's Law, Equation (2.2), applying our definition of contrast, and simplifying to get

$$C_{\mathrm{t}}(\lambda_{\mathrm{t}}) = \exp\left[-\left(\Delta\alpha_{\mathrm{film}} z + f_P \Delta Q\right)\right], \tag{6.1}$$

where z is the thickness of the VO_2 film, Q is the extinction efficiency of the NPs, f_P is the NP areal packing fraction, and C_t is the target contrast for a particular application at a target wavelength λ_t. Here we have assumed a single layer of NPs. Clearly, if $\Delta\alpha_{film} < 1$ so that absorption by the film decreases, as is the case for the VO_2 film, then one must either increase f_P or increase ΔQ in order to compensate. The geometry and specific application place physical limits on both of these quantities, which must be considered when designing an array for a specific application. The change in extinction efficiency is dictated by the sensitivity of the NPs to the changes in ϵ_m. Nanodimers, for example, display an increased sensitivity to changes in ϵ_m at small particle spacing (Chapter IV).

For the 100 nm particle array in this study, it is apparent from Figure 6.1 that this geometry does not compensate sufficiently for the increased transmission of VO_2 in the VS to NIR to bring the contrast below 1. However, the array does measurably alter the contrast, especially at $\lambda = 650$ nm, close to the 700 nm resonance of this array, by a change of approximately 3%. Given that f_P is less than 4%, it is reasonable to assume that a higher packing fraction could enhance this difference considerably. The contrast spectrum for the 180 nm array, with $f_P = 12.6\%$, shows a larger distinction from the 100 nm array. In Figure 6.1, we see that at the Au NP LSPR wavelength for VO_2 in the metallic state, $\lambda_{res} = 800$ nm, the 180 nm array elimates approximately 6% of the transmission through the array for VO_2 in the metallic state compared to the semiconducting state and 13% more light on the array than the film alone in the metallic state. Although the contrast is not as impressive as that achieved at microwave frequencies,[20] this is a significant change in optical absorption

for the Au::VO_2 structure over the film alone in the NIR. Also, as the LSPR shifts from 1000 nm in the semiconducting state to 800 nm in the metallic state for the 180 nm array, thus the LSPR actually reverses the contrast from the film alone in the region above 900 nm. If high enough contrast could be achieved, this could allow for switching between two narrow-band laser sources based on the thermochromic or photochromic response of the VO_2.

Equation (6.1) provides a good starting point for designing tunable dielectric metamaterials or other structures with specific filtering applications in mind. Applying the equation, however, requires a detailed understanding of the dielectric functions of the embedding medium (VO_2 in this case) and the Au. This is not only required for calculating $\Delta\alpha_{\text{film}}$, but for modeling ΔQ_{NP}. Also, we can estimate Q_{NP} for ellipsoidal NPs based on (1.4), but the presence of the substrate, the array geometry, and the proximity of other nanostructures shift the resonance and change the width significantly.[50,51,129,130] Lumerical and other FDTD solvers help account for the array and substrate but still depend on accurate dielectric functions.

For the 180 nm and 100 nm arrays, the figures of merit FOM are calculated to be 0.88 and 0.61. These are significantly higher than what is reported in [21] for split-ring resonators. However, the maximum contrast achieved is still less than 10% due to the damping of the resonance.

Our analysis of (6.1) suggests two ways to increase the contrast for Au::VO_2 structures in the visible to NIR. First, an increase in packing fraction leads to both increased contrast and higher overall extinction within the Au::VO_2 structure. For some applications, the higher extinction may not be desirable. Second, the contrast

can be improved by increasing the sensitivity of the LSPR wavelength to changes in the dielectric function while minimizing Γ; this increases ΔQ by increasing the FOM.

The array structure can help minimize the damping of the LSPR by providing feedback to the LSPR with the second term in Equation (4.2) providing an effective gain coefficient $g = S(r)\epsilon_m\alpha$.[56] Choosing the right grating constant can significantly narrow and increase the extinction of the array.[50] As seen in Figure 3.12, the grating constant by itself is not enough to produce a significantly sharp resonance in the Au::VO_2 structure. Structures that minimize the amount of VO_2 in contact with the metal, such as split-ring resonators (SRRs) where VO_2 is only in the gap, may lead to greater extinction efficiency. In the case of SRRs, precisely designing the structure small enough to operate at optical wavelengths with only VO_2 in contact with the SRR in the gap is very challenging due to technological limitations. Another possibility is stacked NP structures consisting of Au and VO_2 NPs with the interstitial VO_2 removed; this would increase the overall transmission through the structure and could significantly increase the contrast. Perhaps the most physically interesting possibility would be structures that combine Au and VO_2 with a gain medium that can minimize the losses due to the VO_2 interband transitions.[139–141]

6.5 Dielectric Constant of VO_2

The most significant challenge for analyzing our results has been the poor agreement between the literature values of the optical constants of VO_2 (e.g., the Verleur dielectric functions) and the apparently lower values needed to model the systems studied here. As discussed in Section 1.4.2, several experiments have presented con-

tradictory results regarding the dielectric function of VO_2 thin films.[38,82,101–104] Some researchers, such as Dicken *et al.*, have performed their own ellipsometry measurements of the dielectric function for modeling purposes. Modeling plasmon resonances and interactions in metal NPs requires a detailed understanding of the dielectric function describing the embedding medium, and the uncertainties in the dielectric function for VO_2 need to be addressed by researchers.

Attempts at Vanderbilt University to measure the dielectric function of the VO_2 films using ellipsometry have not been successful at finding an oscillator model, such as the Lorentz model described by (1.15), that will work for different samples created on the same type of substrate. Figure 6.2 shows one set of preliminary results taken on a Si substrate with approximately 100 nm VO_2 at room temperature. Equipment limitations prevented temperature-dependent measurements and data with wavelengths above 1000 nm. Measurements that have been made on Si and fitted with a dielectric function model using Lorentzian oscillators show a reduction in magnitude for ϵ'_{semi} and ϵ''_{semi} by approximately a factor of 2 (close to that predicted in Chapter III); however, structural features in ϵ''_{m} that are known to exist appear to be absent in the model. For example, the oscillator structure centered at 1.4 eV corresponding to interband transitions between $3d$ bands has been well established in the literature and in the results presented in Chapter III is not present in Figure 6.2.[38,101–103]

Furthermore, variations between VO_2 films deposited on the same type of substrate make finding a generalized model a challenge. It is known that thin film properties can vary with thickness and substrate, especially for films thinner than 100 nm in thickness.[67,143,144] Verleur *et al.* used a VO_2 film grown on sapphire in

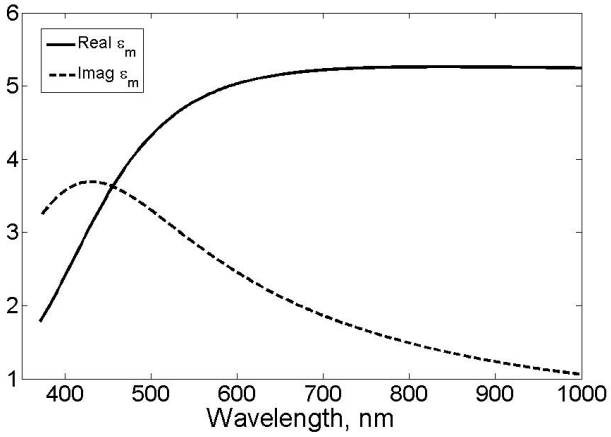

Figure 6.2: Preliminary results of modeling the dielectric function of semiconducting VO_2 from ellipsometry measurements.

their experiments; our experiments dealt exclusively with VO_2 deposited on ITO-coated glass. Currently, efforts are underway at Vanderbilt University to study VO_2 thin film growth under different conditions; these results will help in developing a model to describe how the dielectric properties of the film vary with thickness and substrate.[143,144] Also, upgrades to the ellipsometer that extend the wavelength range and allow for temperature-dependent measurements are now in progress and will provide the means to studying the dielectric function of VO_2 resulting from different growth conditions.

The band structure of VO_2 has been well-studied in the literature,[26,92,96,97] and the Lorentz oscillator energies (approximately 3.5 and 1.4 eV) reported by Verleur *et al.* and Kakiuchida *et al.* agree with these studies.[38,101] The discrepancies between dielectric functions discussed in the previous section likely arise from mostly from large differences in the amplitude and broadening of these oscillators with only small

changes in the oscillator energy.

6.6 Final Remarks

The results presented in Chapters III through V show that the Au::VO_2 nanostructures studied in this work are more sensitive to the detailed shape and magnitude of the dielectric function of VO_2 compared to studies conducted on plain VO_2 thin films. At wavelengths below 1500 nm, the interband transitions of VO_2 dominate the EM interactions between the Au NPs and the VO_2 film. Relatively small changes in the energies, amplitudes, and widths of the Lorentzian oscillators used to describe the dielectric function of VO_2 can result in significant shifts in LSPR position and width. This is partly a result of the large negative slope of the real part of the Au dielectric function. Small changes in ϵ'_{m} can lead to a large shift in LSPR wavelength and allows for sensitive probing of the VO_2 dielectric function. The complex shape of ϵ''_m resulting from the interband transitions lead to large variations of the width of the LSPR as the resonance shifts. This, in turn, affects the interactions of the LSPR with not only the VO_2 film (Chapter III), but also other nanostructures within the geometry (Chapter IV), the EM absorption of the incident light, and the thermodynamics of the system (Chapter V).

Applications of Au::VO_2 structures at VS to NIR wavelengths are hampered by the VO_2 interband transitions. Using structures with the interstitial VO_2 removed or gain media to reduce losses may help increase the extinction due to the LSPR. As discussed in this chapter, there are several key experiments that should be done to better understand Au::VO_2 structures at these wavelengths, all of which will lead to

a better understanding of the interactions between the plasmon and the interband transitions of VO_2. However, the most interesting applications, are probably the ones that are not as obvious and are as yet to be discovered.[145]

APPENDIX A

QUASISTATIC DIPOLE CALCULATIONS

MATLAB® code for analyzing the extinction measurements that were used for the plasmonic hysteresis experiments is copied below. This code is representative of the analysis process for all extinction measurements. Following this is the code for calculating LSPR position and width that was also used in the modeling for Chapter III.

```
%%%%%% Code for analyzing extinction data %%%%%%%%%%%%%%%%%

        %Since we are analyzing two sets of data simultaneously, we want to
        %know how many files are in each.

        N180 = 1:61; %File numbers corresponding to the 180nm particles
        N100 = 62:121; %The 100nm particles



    %Read the data
    if isRead
        D = read_winspecasciiframes(1:121);
        Temp2 = load('temp180.txt');
        Tempflat = Temp2(:, 1);
        TempSpec = Temp2(:, 2);
        TempAvg = (Tempflat + TempSpec) ./ 2;
        Temp(N180) = TempAvg;
        [TempMax(1), nTMx(1)] = max(Temp(N180));

        clear Temp2 Tempflat TempSpec TempAvg

        Temp2 = load('temp100.txt');
        Tempflat = Temp2(:, 1);
        TempSpec = Temp2(:, 2);
        TempAvg = (Tempflat + TempSpec) ./ 2;
        Temp(N100) = TempAvg;
        [TempMax(2), nTMx(2)] = max(Temp(N100));
```

```
        nTMx(2) = nTMx(2) + 61;

    end

    %We only have two x-axis for this data set, so let's not
    %store it multiple times.

    x(1, :) = D{1}(1).x;
    x(2, :) = D{62}(1).x;


    %Get the data in a usable form
    for iDat = 1:length(D)
        for colnum = 1:length(D{iDat}(:))
            wD = D{iDat}(colnum);
            dat = wD.dat;

            %Let's average over the CCD rows and frames.
            yavg = mean(dat, 2);
            yraw(iDat, colnum, :) = mean(yavg(:,:), 2);

            %Do we want to smooth the data?  Do we want an extinction
            %spectra or transmission?  OD?
            if isSmooth
%                 span = 15;
%                 method = 'sgolay';
                y(iDat, colnum, :) = smooth(...
                    yraw(iDat, colnum, :), span, method);
            else
                y(iDat, colnum, :) = yraw(iDat, colnum, :);
            end

            if isExtinct
                y(iDat, colnum, :) = -log(y(iDat, colnum, :));
            end

            %Now let's get where the plasmon resonance occurs.  Let's keep in
            %mind that for extinction spectra, we want the max, while in
            %transmission, we want the min.  We can also get the FWHM, etc.
            if isExtinct
                [yMx(iDat, colnum), xpMx(iDat, colnum)] = ...
                    max(squeeze(y(iDat, colnum, :)));
            else
                [yMx(iDat, colnum), xpMx(iDat, colnum)] = ...
                    min(squeeze(y(iDat, colnum, :)));
            end
```

```
            if iDat < 62
                S = 1;
            else
                S = 2;
            end

            foofwhm(iDat, colnum) = ...
             bandpass2(x(S, :), squeeze(y(iDat, colnum, :)));
            decaywidth50(iDat, colnum) = foofwhm(iDat, colnum).bw50;
            decaywidth90(iDat, colnum) = foofwhm(iDat, colnum).bw90;

            %Any other data processing that requires "the loop" would go here.



            %Done processing?  Let's close the cloop.
        end
    end

%%%%%%% Modeling LSPR position and width  %%%%%%%%%%%%%%%

    load metals_nk; %Load Au optical constants

    reff = [0 0];

    la = [180 100]./2 + reff;
    lb = la;
    lc = 20    /2;
    V = (4*pi/3).*la.*lb.*lc;

    ecc = sqrt(1 - lc^2./la.^2);
    L = (sqrt((1-ecc.^2)./ecc.^2)./(2*ecc.^2)).*((pi/2)...
     -atan(sqrt((1-ecc.^2)./ecc.^2)))-...
        (1-ecc.^2)./(2.*ecc.^2);

%     figure(1), clf
%     hold on
%     figure(2), clf
%     hold on

%     C = {'b.'; 'r.'};



    Tw = 2.73;
```

```
    lambda = (920).';

    eps1 = metals_nk.au.n(lambda).^2 - metals_nk.au.k(lambda).^2;
    eps2 = 2*metals_nk.au.n(lambda).*metals_nk.au.k(lambda);
    eps = eps1 + j*eps2;

    [epsVsr, epsVsi, epsVmr, epsVmi] = epsVO2(lambda);
    %For the 180s
%     a1 = 0.53;
%     a2 = 0.33;
%     b1 = 0.75;
%     b2 = 0.69;

    %For the 100s
    a1 = 0.67;
    a2 = 0.25;
    b1 = 0.80;
    b2 = 1.4;
    isSize = 0;

    epsV1 = (a1*epsVsr + b1*1i*epsVsi).';
    epsV2 = (a2*epsVmr + b2*1i*epsVmi).';

    epsVin = 1;
%     fin = 0.3954;
    fin = 0.25;
    epsV(:, 1) = epsV1;
    epsV(:, 2) = epsV2;
%     [nI kI] = epsITO(lambda);
    nI = 1.775;
    kI = 0.012;
    epsS1 = nI.^2 - kI.^2;
    epsS2 = 2.*nI.*kI;

    wS = 1;
    epsS = (wS.*(epsS1 + 1i*epsS2) + (1-wS)*2.25).';

%     f = [0 1];


    fmax = 1;
    scale = 1;  %[0.367 0.236];
    %Calculate the cross-section
    for ii = 1:length(D)

        if ii < nTMx(1)
```

```
            Tt = 74;
            S = 1;
            jj = 1;
        elseif ii >= nTMx(1) && ii < 62
            Tt = 62;
            S = 2;
            jj = 1;
        elseif ii >= 62 && ii < nTMx(2)
            Tt = 74;
            S = 3;
            jj = 2;
        elseif ii > nTMx(2)
            Tt = 62;
            S = 4;
            jj = 2;
        end

        f(ii) = fmax*(1-1./(1+exp((Temp(ii)-Tt)/Tw)));
        epsVeff(:, ii) = ((1-f(ii))*epsV(:, 1) + f(ii)*epsV(:, 2));
%
%       BR Effective Medium
%         epsVeff(:, ii) = 0.25*(epsV(:, 1).*(2-3*f(ii)) + ...
epsV(:, 2).*(3*f(ii)-1) +...
%             sqrt((epsV(:, 1).*(2-3*f(ii)) + ...
epsV(:, 2).*(3*f(ii)-1)).^2 + 8*epsV(:, 1).*epsV(:, 2)));
%
%         FOr modeling MG
%         epsVeff(:, ii) = epsV(:, 1).*(epsV(:, 2).*(1+2*f(ii)) - ...
epsV(:, 1).*(2*f(ii)-2))./...
%             (epsV(:, 1).*(2 + f(ii))+epsV(:, 2).*(1-f(ii)));
%
        epsM(:, ii) = (epsVeff(:, ii) + epsS)./2;
%         epsM(:, ii) = epsVeff(:, ii);

%           epsM(:, ii) = 2.25;

        % To account for size effects, set isSize to 1;
        if isSize == 1
            A = -0.4865*L(jj) - 1.046*L(jj).^2 + 0.8481*L(jj).^3;
            B = 0.01909*L(jj) + 0.1999*L(jj).^2 + 0.6077*L(jj).^3;
            xx = pi*la(jj)./lambda;

            alpha(:, ii) = V(jj)./((L(jj)+(epsM(:, ii)./(eps-epsM(:, ii)))) ...
                + A*epsM(:, ii).*xx.^2 + B*epsM(:, ii).^2.*xx.^4 - ...
                j*((4/3)*pi^2*epsM(:, ii).^(3/2).*(V(jj)./lambda.^3)) );
        else
                alpha(:, ii) = V(jj).*(eps - epsM(:, ii))./ ...
```

```
                (epsM(:, ii) + L(jj)*(eps - epsM(:, ii)));
        end
        km = 2*pi*sqrt(epsM(:, ii))./lambda;
        Cabs(:, ii) = real(km).*imag(alpha(:, ii));
        Csca(:, ii) = abs(km).^4.*abs(alpha(:, ii)).^2/(6*pi);
        Cext = Cabs + Csca;

%         Cext = abs(alpha);
        [yTMx(ii), xpTMx(ii)] = max(Cext(1:end, ii));

%     [yTMx(ii), xpTMx(ii)] = ...
min(abs(real(epsM(:, ii) + L(jj)*(eps-epsM(:, ii)))));


      foofwhmT(ii) = bandpass2(lambda, Cext(:, ii));
            dw50(ii) = foofwhmT(ii).bw50;
            dw90(ii) = foofwhmT(ii).bw90;

    end


    figure(1), clf
    hold on

%     ss = 1;
%     scale = 16;
%     scale2 = 1e-7;
%     Acell = 450^2;
%     plot(lambda, Cabs(:, ss)/Acell, 'b')
%         plot(lambda, Csca(:, ss)/Acell, 'r')
%             plot(lambda, Cext(:, ss)/Acell, 'k')
%     plot(lambda, scale2*abs(real(alpha(:, ss))), 'g')
%     plot(x(1, :), scale*squeeze(y(ss, 2, :)), 'g')
    subplot(1, 2, 1)
    hold on
    plot(Temp(1:nTMx(1)), x(1, xpMx(1:nTMx(1), 2)), 'r.', ...
        Temp(nTMx(1):61), x(1, xpMx(nTMx(1):61, 2)), 'b.')

    plot(Temp(1:nTMx(1)), lambda(xpTMx(1:nTMx(1))), 'r-', ...
        Temp(nTMx(1):61), lambda(xpTMx(nTMx(1):61)), 'b-')
%

    xlim([20 100]);
    xlabel('Temperature, ^{o}C')
    ylabel('LSPR, nm')
    title('180nm')
%
```

```
    subplot(1, 2, 2)
    hold on
    plot(Temp(1:nTMx(1)), decaywidth90(1:nTMx(1), 2), 'r.', ...
        Temp(nTMx(1):61), decaywidth90(nTMx(1):61, 2), 'b.')

    plot(Temp(1:nTMx(1)), dw90(1:nTMx(1)), 'r-', ...
        Temp(nTMx(1):61), dw90(nTMx(1):61), 'b-')
    xlabel('Temperature, ^{o}C')
    ylabel('Full width, 90% maximum, nm')
    legend('Heating Data', 'Cooling Data', 'Heating fit', 'Cooling fit')
    figure(2), clf
    hold on

    subplot(1, 2, 1)
    hold on
    plot(Temp(62:nTMx(2)), x(2, xpMx(62:nTMx(2), 2)), 'g.',...
       Temp(nTMx(2):end), x(2, xpMx(nTMx(2):end, 2)), 'c.')

    plot(Temp(62:nTMx(2)), lambda(xpTMx(62:nTMx(2))), 'g-', ...
        Temp(nTMx(2):end), lambda(xpTMx(nTMx(2):end)), 'c-')


    xlim([20 100]);
    xlabel('Temperature, ^{o}C')
    ylabel('LSPR, nm')
    title('100nm')

    subplot(1, 2, 2)
    hold on
    plot(Temp(62:nTMx(2)), decaywidth90(62:nTMx(2), 2), 'g.', ...
        Temp(nTMx(2):121), decaywidth90(nTMx(2):121, 2), 'c.')
%
    plot(Temp(62:nTMx(2)), dw90(62:nTMx(2)), 'g-', ...
        Temp(nTMx(2):121), dw90(nTMx(2):121), 'c-')
    xlabel('Temperature, ^{o}C')
    ylabel('Full width, 90% maximum, nm')
    legend('Heating Data', 'Cooling Data', 'Heating fit', 'Cooling fit')
    xlim([20 100]);

%     figure(1)
%     plot(x(1, :), squeeze(y(1, 2, :)), 'b--');
% %     plot(x(1, :), squeeze(y(nTMx(1), 2, :)), 'r--');
%     figure(2)
%     plot(x(2, :), squeeze(y(62, 2, :)), 'b--');
% %     plot(x(2, :), squeeze(y(nTMx(2), 2, :)), 'r--');
%
% %     f = fmax*(1-1./(1+exp((Temp(iDat)-Tt)/Tw)));
```

```
%
% %     plot(Temp(iDat), , char(C(S)))
```

APPENDIX B

PLASMON-ENHANCED LOW-INTENSITY LASER SWITCHING OF GOLD::VANADIUM DIOXIDE NANOCOMPOSITES

As submitted to *Applied Physics Letters*: **Abstract** Transient absorption of gold nanoparticle arrays (NPs) covered by a 60 nm thick film of VO_2 was measured using a mechanically shuttered 785 nm pump laser and a 1550 nm CW probe. Even though the Au NPs constitute only 4% by volume of the nanocomposite, they increase the effective absorption coefficient by a factor 1.5 and reduce the threshold laser power required to induce the semiconducting to metal transition (SMT) by as much as 37%. It is argued that the NPs function as thermal initiators for the SMT and as "nanoradiators" to increase the scattering and absorption of light into interband transitions of the VO_2.

Optically active nanocomposites (NCs) in which the semiconductor-to-metal transition (SMT) of vanadium dioxide (VO_2) alters the plasmonic response of embedded or adjacent silver (Ag) or gold (Au) nanostructures have recently been described in applications to sensors, optical elements, and memory elements.[12,16,17,20–22] In these cases, a thermally induced SMT alters the dielectric environment of a metal nanostructure in contact with the VO_2 film, shifting the localized surface plasmon resonance (LSPR) of the metal and altering the optical response of the NC. There are, however, many applications in which *photochromic*, rather than thermochromic, regulation of a plasmonic response would be desirable, particularly if it could be accomplished with low-power lasers.

It is well known that the SMT in VO_2 films[93] and nanoparticles (NPs) can be induced by ultrafast laser irradiation at high intensities; in this case, the initial response

is a result of femtosecond band-gap renormalization. Subsequent cooling to the semiconducting state results from electron-phonon interactions on a sub-nanosecond time scale. On the other hand, for low-power or long-pulse laser switching at photon energies above the VO_2 band-gap, a band-to-band electronic excitation drives the SMT by laser-induced heating from carrier-carrier and carrier-phonon interactions. In this case, relaxation to the semiconducting state occurs by all thermodynamic mechanisms available to the VO_2 film, including interactions with the substrate or environment.[75]

Low-power optical switching of VO_2 thin films has been recently demonstrated in the context of optical limiting, optical switching, and thermochromic windows.[72,73,75] Here, we demonstrate that embedding an array of Au nanoparticles in a VO_2 thin film at a volumetric concentration below 5% both (a) reduces the photochromic switching threshold by more than one third, and (b) reduces the time to complete the SMT by a factor of $\sim$5. This increased switching efficiency results from coupling of the LSPR to VO_2 interband transitions: the resulting plasmon damping increases the rate of laser heating of the film and compensates for energy loss to the substrate. First-principles analysis substantiate these conclusions.

Square arrays of 140 nm diameter Au NPs, 500 μm on a side and with a grating constant of 350 nm, were fabricated on an indium-tin-oxide coated glass substrate by standard electron beam lithography techniques using a poly(methyl methacrylate) resist, as illustrated in Fig. B.1(a). Gold was subsequently deposited by electron-beam evaporation to a thickness of 20 nm as measured by a quartz crystal microbalance. A 60 nm film of VO_2 was deposited over the array by pulsed laser ablation of a vanadium target in 10 mTorr O_2 background gas (KrF laser pulsed at 25 Hz, fluence 1.2 J/cm^2)

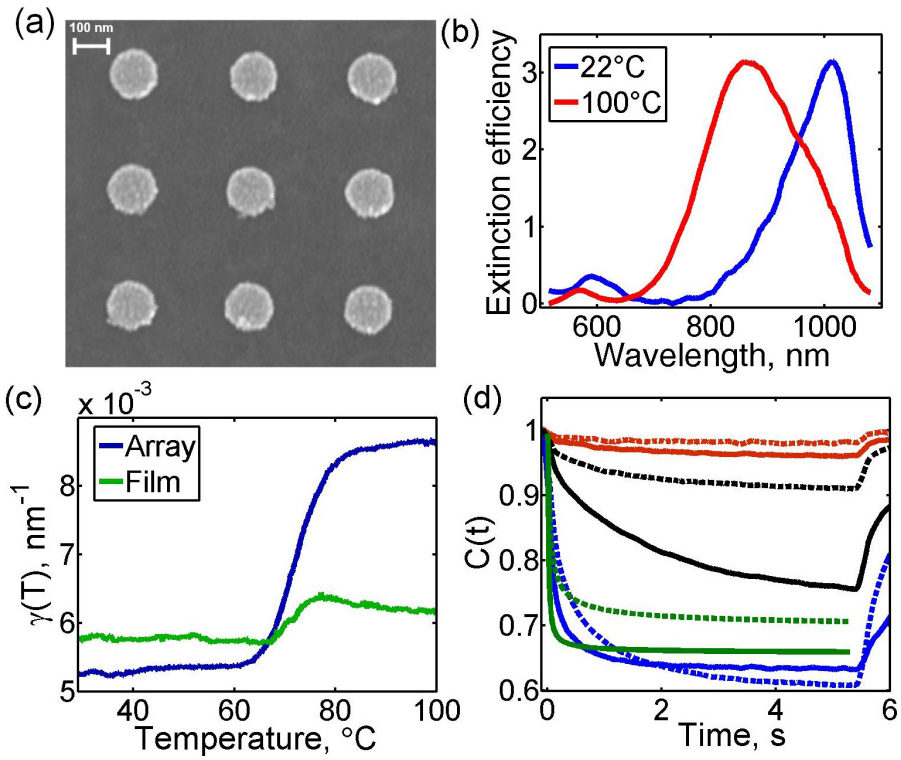

Figure B.1: (a) A scanning electron microscopy image of the 140 nm Au NP array before deposition of the VO_2 film. (b) Extinction spectra of 140 nm NP arrays in each VO_2 phase. (c) Absorption coefficient $\gamma(T)$ taken at 785 nm and calculated from transmission measurements. (d) Typical $C(t)$ measurements through a plain VO_2 film (dashed) and on the Au::VO_2 structure (solid) for 33 (red), 76 (black), and 163 W/cm^2 (blue); theoretical prediction from Eq. B.2 for 76 W/cm^2 is shown in green.

followed by annealing for 45 minutes in 250 mTorr O_2 at 450°C; the thickness was confirmed by profilometry.[114] The sample was mounted on a Cu block heated by a Peltier element; a thermocouple surface-mounted to a witness substrate monitored the temperature. A broadband tungsten lamp was used for spectrally resolved white-light extinction measurements; transmission in the VO_2 film surrounding the arrays varied across the sample by ±2%, confirming that the film was reasonably uniform.

Extinction spectra of the Au::VO_2 sample in each VO_2 phase referenced to the plain VO_2 film, Fig. B.1(b), show that the peak of the LSPR shifts by approximately 250 nm during the VO_2 SMT. Fig. B.1(c) shows the absorption coefficients for the film $\gamma_{\rm film}(T)$ and NC $\gamma_{\rm NC}(T)$, at 785 nm calculated from our measured transmission spectra and measured reflectivity $R_{\rm semi}$ and $R_{\rm met}$ of semiconducting and metallic VO_2.[38] In a mean-field model, $R(T) = (1-f)R_{\rm semi} + fR_{\rm met}$, where $f(T)$ is the fraction of metallic VO_2 assuming a sigmoidal T-dependence with critical temperature $T_{\rm c} = 72°$C. At low T, Fig. B.1(c) indicates that the NPs have only small absorption at 785 nm; calculations show that the 10% discrepency between film and array shown in Fig. B.1(c) can be accounted for by a difference $\Delta R_{\rm semi} = \pm 0.03$.

The phase transition was induced by focusing a shuttered 785 nm heating (pump) beam with intensity I controlled by a variable neutral density filter; the SMT was monitored by a 1550 nm CW diode laser with intensity fixed at 18 W/cm^2. The heating and probe beams were normally incident about 10 mm apart on a 76 mm diameter glass lens with focal length 85 mm. The radii of the pump and probe beams at the focal spot were measured using a knife-edge technique to be 120$\pm$5 μm and 105$\pm$10 μm. The sample was irradiated for 5.3 s, and allowed to recover completely between measurements. The temperature of the substrate was clamped at 55°C to insure reproducible initial conditions.

The contrast $C(t)$, defined as the probe transmission normalized to semiconducting VO_2, is shown in Fig. B.1(d) for the VO_2 film (dashed) and the Au::VO_2 NC (solid). At maximum I, when the shutter opens ($t = 0$), $C(t)$ decreases sharply as the laser drives the VO_2 toward the SMT; the VO_2 film takes $\sim$5 times as long

to reach maximum contrast $C_{\max} \equiv C(5.3\text{ s})$ as the Au::VO_2 NC. Since Fig. B.1(c) shows that by 85°C the transition is essentially complete, Fig. B.1(d) suggests that at maximum I the NC reaches $T \approx 85$°C at approximately 1 s, whereas the VO_2 film takes at least the full 5.3 s.

The dynamics of the NC and plain VO_2 film were analyzed by fitting $C_{\max}(I)$ with a three-parameter sigmoid given by

$$C(I) = 1 - \frac{1 - C_{\mathrm{H}}}{1 + \exp\left(-\frac{I - I_{\mathrm{c}}}{I_{\mathrm{w}}}\right)}, \tag{B.1}$$

where I_{c} is the critical switching intensity defined at the midpoint of the SMT, I_{w} is the width of the transition, and C_{H} is the high-T contrast. The fit to the data of Fig. B.2(a), indicate that I_{c} decreases from 104±2 W/cm^2 for the plain VO_2 film to 66.2±1.9 W/cm^2 for the NC, or a factor of 1.5. Similarly, I_{w} decreases by roughly the same factor, from 21.9±1.3 W/cm^2 for the film to 15.5±1.3 W/cm^2 for the NC. The 4.2% volume fraction of Au NPs in the NC yields two key advantages over the plain VO_2: the NC (a) reaches $T_{\mathrm{c}} \approx 72$°C at 37% lower I_{c} and (b) exhibits increased sensitivity of $C(I)$ to changes in I during the SMT.

The enhanced switching performance of the NC compared to the VO_2 film can be explained using first-principles thermodynamics. The film or NC is responsible for nearly all laser absorption in this experiment; however, at low power, heat conduction across the VO_2-glass interface is significant over the time required for either the film or the NC to complete the SMT. Because of the thickness of the VO_2 or NC films relative to the substrate, the system can be treated as a thin membrane, heated by

the laser, sitting atop a semi-infinite substrate. Assuming constant average surface heat flux q within a radius a and insulating boundary conditions, the temperature rise at the interface $\Delta T(r = 0, z = 0, t)$ is

$$\Delta T = \frac{2q\sqrt{\alpha t}}{\kappa}\left[\frac{1}{\sqrt{\pi}} - \text{ierfc}\left(\frac{a}{2\sqrt{\alpha t}}\right)\right], \tag{B.2}$$

where $q = I\,(1 - R)\,[1 - \exp\,(-\gamma_{\text{eff}} z_0)]$ is the energy absorbed in the plain film or NC, $\alpha = 5.3 \times 10^{-3}$ cm^2/s and $\kappa = 9.6$ mW/(cm °C) are the thermal diffusivity and conductivity of the glass substrate, R is the reflectivity at the VO_2-air interface, γ_{eff} is the effective laser absorption coefficient, and z_0 is the thickness of the film.[138] In our calculation, we used the experimental data to estimate $T(5.3\text{ s})$, and subsequently $R(5.3\text{ s})$ and $\gamma_{\text{eff}}(5.3\text{ s})$. The same mean-field model used for R yields a predicted normalized contrast $C_{\text{th}}[T(t)] = [1 - f(T)] + f(T)C_{\text{H}}$.

For both the VO_2 film and Au::VO_2 NC at $I = 76$ W/cm^2, Eq. B.2 predicts faster decreases in $C(t)$ and increased $C_{\max}$ than what is observed experimentally [Fig. B.1(d)]. However, this method over-weights the contribution of the high-T absorption in the calculation, leading to an over-predicted $C_{\max}$. The model also does not account for the granular nature of the VO_2 film, which inhibits lateral heat diffusion out of the laser focal spot. However, the essential features of the experiment are reproduced by the analysis; specifically, for a given I, the NC reaches a higher VO_2 metallic fraction, and therefore a higher $C_{\max}$, faster than a plain VO_2 film.

Numerical differentiation of $C(t)$ from Fig. B.1(d) shows that the maximum rate of change $\dot{C}_{\max}$ occurs for $t \approx 0.1$ s. At that time, a thermodynamic tipping point has

been reached: the thermal diffusion length $\sqrt{\alpha t}$ has reached approximately 100 μm, implying that the film-substrate system is then at the same T. As laser energy continues to be deposited into the system, both substrate and film rise in T at a slower rate; this is visible in both the NC and thin-film curves of Fig. B.1(d). The VO_2 continues to turn increasingly metallic until the system reaches steady-state T.

A plot of $\dot{C}_{\max}(I)$ [Fig. B.2(b)] shows that the values for $\dot{C}_{\max}$ increase linearly at almost identical rates for the film and the NC up to their respective I_c, at which point $\dot{C}_{\max}$ rises sharply for each. The sudden change in slope indicates that the system contains more metallic VO_2 than semiconducting, as one expects for $I > I_c$ determined from Fig B.2(a). The near identical slopes for $\dot{C}_{\max}$ before and after I_c suggest that the system is in equilibrium with the substrate, limiting the rise in T as expected.

As the T in the NC increases towards T_c, the LSPR redshifts and NP extinction at 785 nm increases sharply [Fig. B.1(b)–(c)]. The resulting positive feedback from the LSPR increases the scattering and absorption of light within the VO_2. The scattered light is subsequently absorbed by VO_2 interband transitions; light absorbed by Au NPs is converted to heat by electron-phonon scattering and communicated to the VO_2 by phonon-phonon scattering across the Au-VO_2 interface. From Eq. B.2, the average steady-state increase in temperature at the surface of the glass for $r < a$ is $\overline{\Delta T} = 8aq/3\pi\kappa$. Hence the 37% decrease in I_c for the Au::VO_2 system is consistent with γ_{NC} increased by 0.0033/nm, in close agreement with the change in $\gamma_{NC}(T)$ from Fig. B.1(c); this increased absorption leads to higher T in the NC by compensating for the heat transport across the interface. Effectively, the presence of the Au NPs

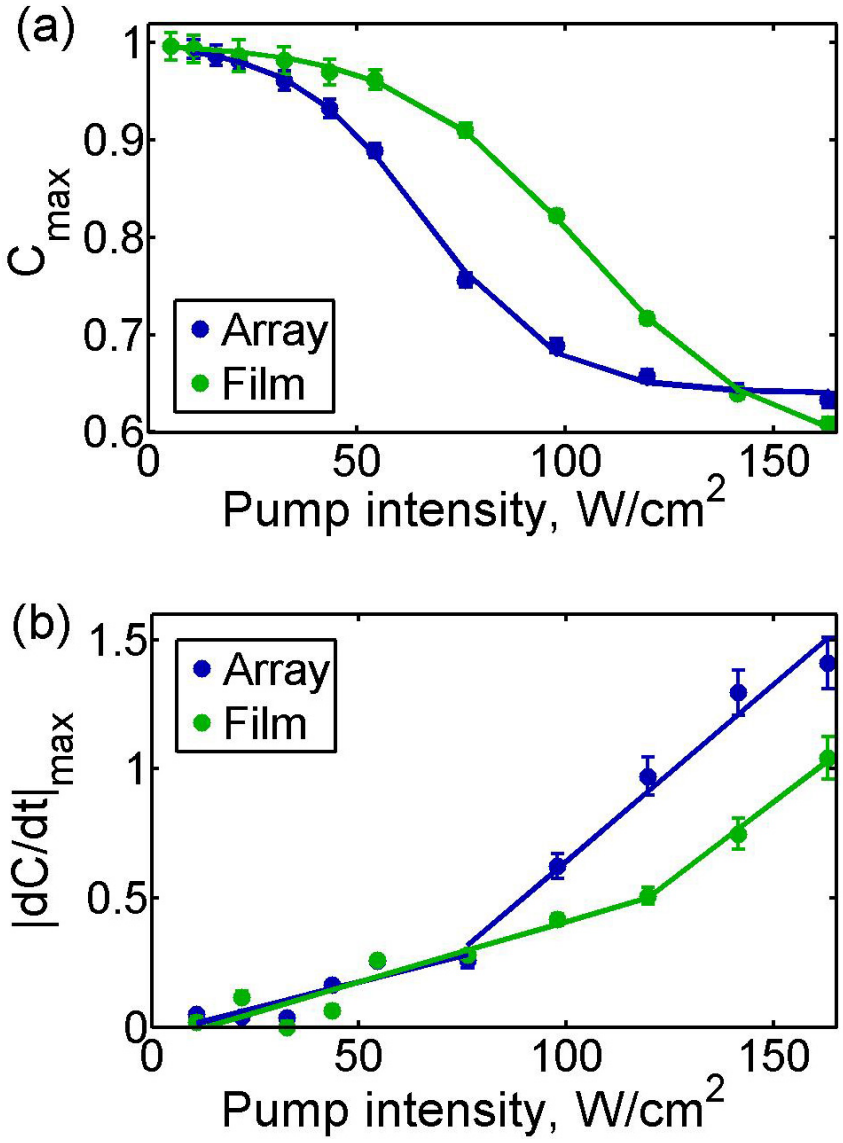

Figure B.2: (a) Maximum contrast vs. pump intensity for 140 nm NP arrays and VO_2 film at $t = 5.3$ s. (b) Maximum rate of contrast change $\dot{C}_{\max}$ as a function of intensity.

compensates for about 40 W/cm^2 of laser intensity needed to switch the film by acting as a "nanoradiator" and enhancing the rate of energy deposition in the film.

Our analysis is consistent with a recent model of thermal self-regulation in Au NPs capped by a VO_2 shell,[30] suggesting that an optimized substrate-NC system for low-power laser-induced switching can be designed using the LSPR shift driven by the VO_2 SMT if one fully accounts for the thermal properties of the system.

Acknowledgments This work was supported by the U.S. Department of Energy, Office of Science (DE-FG02-01ER45916) and the ITT Corporation's National Security Technology Applications Division. ERM gratefully acknowledges a William and Nancy McMinn Honor Scholarship for the Natural Sciences.

APPENDIX C

HEAT TRANSPORT CALCULATIONS

MATLAB® code for modeling the temperature rise due to laser-heating, as described in Chapter V.

```
%%% Optical Constants and Physical Parameters %%%
a = 121e-4; %cm Laser spot radius
K = 9.6; %mW/cm/K of glass
D = 5.2e-3; %cm^2/s of glass
I = 0.9*76e3; %W/cm^2 Laser intensity

%%% Prepare figure
figure(1)
hold on

%%% Do the calculation and plot it
for ii = 1:2;
% for I = [20:20:160]*1e3
    if ii == 1
        CM = 0.64;
%         d = 0.0074^(-1);
        d = 0.0074^(-1);
        f = 0.32;
    %     K = 9;
    %     I = 163e3;
        R = 0.18;
%         R = 0.15;
    elseif ii == 2
        CM = 0.57;
        d = 0.0058^(-1);
%         d = 0.0044^(-1);
        f = 0.77;
    %     K = 12;
    %     I = 0.9*163e3;
        R = 0.23;
    end
Q = ((1-R)*I*(1-exp(-60/d)))  %Heat absorbed
trans = I*(1-R)*exp(-60/d)
t = 0.001:0.001:5.3; %Time scale
```

```
t2 = t-0.001;
z = 0;

%Define ierfc function
ierfc = @(x) (1/sqrt(pi)).*exp(-x.^2) - x.*erfc(x);

%Calculate Temperature
T = @(z, t, a, q) 55 + (2*q*sqrt(D*t)/K).*(ierfc(z./(2*sqrt(D*t)))-...
ierfc(sqrt(z.^2 + a^2)./(2.*sqrt(D*t))));

%Contrast
C = @(T) 1-(1-CM)./(1+exp(-(T-72)/2.75));


figure(1)
plot(t+0.1, C(T(z, t, a, Q)), 'color', colord(ii))

end
% end
legend('Array', 'Film')
xlabel('Time, s', 'FontSize', 30)
xlim([0 6])
ylabel('Contrast, I=76 W/cm^{2}', 'FontSize', 30)
```

REFERENCES

[1] M. Faraday, "Experimental relations of gold (and other metals) to light," *Philosophical Transactions of the Royal Society of London* **147**, p. 145, 1857.

[2] D. Thompson, "Michael Faraday's recognition of ruby gold: the birth of modern nanotechnology," *Gold Bulletin* **40**(7), pp. 267–269, 2007.

[3] J. W. Strutt, "XXXVI. on the light from the sky, its polarization and colour," *Philosophical Magazine Series 4* **41**, pp. 274–279, 1871. Note: John William Strutt is best remembered by his title, the third Baron Rayleigh.

[4] V. Twersky, "Rayleigh scattering," *Applied Optics* **3**, pp. 1150–1162, 1964.

[5] S. A. Maier, *Plasmonics: Fundamentals and Applications*, Springer Science+Business Media, LLC, New York, NY, 2007.

[6] P. K. Jain, X. Huang, I. H. El-Sayad, and M. A. El-Sayed, "Review of some interesting surface plasmon resonance-enhanced properties of noble metal nanoparticles and their applications to biosystems," *Plasmonics* **3**, pp. 107–118, 2007.

[7] B. Sepúlveda, A. Calle, L. M. Lechuga, and G. Armelles, "Highly sensitive detection of biomolecules with the magneto-optic surface-plasmon-resonance sensor," *Optics Letters* **31**(8), pp. 1085–1087, 2006.

[8] M. I. Stockman, "Nanofocusing of optical energy in tapered plasmonic waveguides," *Physical Review Letters* **93**(13), p. 137404, 2004.

[9] D. Schurig, J. J. Mock, B. J. Justice, S. A. Cummer, J. B. Pendry, A. F. Starr, and D. R. Smith, "Metamaterial electromagnetic cloak at microwave frequencies," *Science* **314**(5801), pp. 997–980, 2006.

[10] D. R. Smith, J. B. Pendry, and M. C. K. Wiltshire, "Metamaterials and negative refractive index," *Science* **305**, pp. 788–792, 2004.

[11] A. Sihvola, "Metamaterials in electromagnetics," *Metamaterials* **1**(1), pp. 2–11, 2007.

[12] M. Maaza, O. Nemraoui, C. Sella, A. C. Beye, and B. Baruch-Barak, "Thermal induced tunability of surface plasmon resonance in Au–VO_2 nano-photonics," *Optics Communications* **254**, pp. 188–195, 2005.

[13] Gang Xu, Chun-Ming Huang, Ping Jin, Masato Tazawa, and De-Ming Chen, "Nano-Ag on vanadium dioxide. I. Localized spectrum tailoring," *Journal of Applied Physics* **104**, p. 053101, 2008.

[14] Gang Xu, Chun-Ming Huang, Masato Tazawa, Ping Jin, and De-Ming Chen, "Nano-Ag on vanadium dioxide. II. Thermal tuning of surface plasmon resonance," *Journal of Applied Physics* **104**, p. 053101, 2008.

[15] Gang Xu, Chun-Ming Huang, Masato Tazawa, Ping Jin, De-Ming Chen, and L. Miao, "Electron injection assisted phase transition in a nano-Au-VO_2 junction," *Journal of Applied Physics* **104**, p. 053101, 2008.

[16] Gang Xu, C. Huang, Masato Tazawa, Ping Jin, and L. Chen, "Tunable optical properties of nano-Au on vanadium-dioxide," *Optics Communications* **282**, pp. 896–902, 2009.

[17] J. Y. Suh, E. U. Donev, D. W. Ferrara, K. A. Tetz, L. C. Feldman, and R. F. Haglund, Jr., "Modulation of gold particle-plasmon resonance by the metal-semiconductor transition of vanadium dioxide," *Journal of Optics A: Pure and Applied Optics* **10**, p. 055202, 2008.

[18] J. Y. Suh, E. U. Donev, R. Lopez, L. C. Feldman, and R. F. Haglund, Jr., "Modulated optical transmission of subwavelength hole arrays in metal-VO_2 films," *Applied Physics Letters* **88**, p. 133115, 2006.

[19] D. W. Ferrara, J. Nag, E. MacQuarrie, K. Appavoo, and R. F. Haglund, Jr., "Far-field coupling in arrays of gold and gold::vanadium dioxide nanodimers," *Proceedings of SPIE* **7394**, p. 73942Q, 2009.

[20] M. Seo, J. Kyoung, H. Park, S. Koo, H. Kim, H. Bernien, B. J. Kim, J. H. Choe, Y. H. Ahn, H. Kim, N. Park, Q. Park, K. Ahn, and D. Kim, "Active terahertz nanoantennas based on VO_2 phase transition," *Nano Letters* **10**(6), pp. 2064–2068, 2010.

[21] M. J. Dicken, K. Aydin, I. M. Pryce, L. A. Sweatlock, E. M. Boyd, S. Walavalkar, J. Ma, and H. A. Atwater, "Frequency tunable near-infrared metamaterials based on VO_2 phase transition," *Optics Express* **17**(20), pp. 18330–18339, 2009.

[22] T. Driscoll, S. Palit, M. M. Qazilbash, M. Brehm, F. Keilmann, B.-G. Chae, S.-J. Yun, H.-T. Kim, S. Y. Cho, N. M. Jokerst, D. R. Smith, and D. N. Basov, "Dynamic tuning of an infrared hybrid-metamaterial resonance using vanadium dioxide," *Applied Physics Letters* **93**, p. 024101, 2008.

[23] T. Driscoll, H.-T. Kim, B.-G. Chae, B.-J. Kim, Y.-W. Lee, N. M. Jokerst, S. Palit, D. R. Smith, M. D. Ventra, and D. N. Basov, "Memory metamaterials," *Science* **325**, p. 1518, 2009.

[24] A. W. Clark, A. K. Sheridan, A. Glidle, D. R. S. Cumming, and J. M. Cooper, "Tuneable visible resonances in crescent shaped nano-split-ring resonators," *Applied Physics Letters* **91**, p. 093109, 2007.

[25] C. N. R. Rao and G. V. S. Rao, *Transition Metal Oxides: Crystal Chemistry, Phase Transition and related Aspects*, National Bureau of Standards, *49*, 1974.

[26] V. Eyert, "The metal-insulator transitions of VO_2: A band theoretical approach," *Annalen der Physik (Leipzig)* **11**(9), pp. 650–702, 2002.

[27] H. Nishi, T. Asahi, and S. Kobatake, "Light-controllable surface plasmon resonance absorption of gold nanoparticles covered with photochromic diarylethene polymers," *Journal of Physical Chemistry C* **113**(40), pp. 17359–17366, 2009.

[28] J. A. Dionne, K. Diest, L. A. Sweatlock, and H. A. Atwater, "PlasMOStor: A Metal-Oxide-Si field effect plasmonic modulator," *Nano Letters* **9**(2), p. 897902, 2009.

[29] R. Castillo-Garza, C.-C. Chang, D. Jimenez, G. L. Klimchitskaya, V. M. Mostepanenko, and U. Mohideen, "Experimental approaches to the difference in the Casimir force due to modifications in the optical properites of the boundary surface," *Physical Review A* **75**, p. 062114, 2007.

[30] M. B. Cortie, A. Dowd, N. Harris, and M. J. Ford, "Core-shell nanoparticles with self-regulating plasmonic functionality," *Physical Review B* **75**, p. 113405, 2007.

[31] S. Guenneau, A. Movchan, G. Pétursson, and S. A. Ramakrishna, "Acoustic metamaterials for sound focusing and confinement," *New Journal of Physics* **9**, p. 399, 2007.

[32] A. Alù and N. Engheta, "Plasmonic and metamaterial cloaking: physical mechanisms and potentials," *Journal of Optics A: Pure and Applied Optics* **10**, p. 093002, 2008.

[33] T. Yamaguchi, S. Yoshida, and A. Kinbara, "Effect of retarded dipole-dipole interactions between island particles on the optical plasma-resonance absorption of a silver-island film," *Journal of the Optical Society of America* **64**, pp. 1563–1568, 1974.

[34] D. A. Genov, ShuangZhang, and X. Zhang, "Mimicking celestial mechanics in metamaterials," *Nature Physics* **5**, pp. 687–692, 2009.

[35] P. A. Huidobro, M. L. Nesterov, L. Martin-Moreno, and F. J. Garcia-Vidal, "Transformation optics for plasmonics," *Nano Letters* , p. DOI: 10.1021/nl100800c, 2010.

[36] Y. Liu, T. Zentgraf, G. Bartel, and X. Zhang, "Transformational plasmon optics," *Nano Letters* , p. DOI: 10.1021/nl1008019c, 2010.

[37] E. Lidorikis, S. Egusa, and J. D. Joannopoulos, "Effective medium properties and photonic crystal superstructures of metallic naoparticle arrays," *Journal of Applied Physics* **101**, p. 054304, 2007.

[38] H. W. Verleur, A. S. Barker, and C. Berglund, "Optical properties of VO_2 between 0.25 and 5 eV," *Physical Review* **172**(3), pp. 788–798, 1968.

[39] P. K. Jain and M. A. El-Sayed, "Noble metal nanoparticle pairs: Effect of medium for enhanced sensing," *Nano Letters* **8**, pp. 4347–4352, 2008.

[40] S. Lal, S. E. Clare, and N. J. Halas, "Nanoshell-enabled photothermal cancer therapy: Impending clinical impact," *Accounts of Chemical Research* **41**(12), pp. 1842–1851, 2008.

[41] W. Hasan, C. L. Stender, M. H. Lee, and C. L. Nehl, "Tailoring the structure of nanopyramids for optimal heat generation," *Nano Letters* **9**(4), pp. 1555–1558, 2009.

[42] R. Ritchie, "Plasma losses by fast electrons in thin films," *Physical Review* **106**, pp. 874–881, 1957.

[43] U. Kreibig and M. Vollmer, *Optical Properties of Metal Clusters*, Springer-Verlag, Berlin, 1995.

[44] C. F. Bohren and D. R. Huffman, *Absorption and Scattering of Light by Small Particles*, Wiley-Interscience, New York, 1983.

[45] B. K. Canfield, S. Kujalal, K. Jefimovs, T. Vallius, J. Turunen, and M. Kauranen, "Polarization effects in the linear and nonlinear optical responses of gold nanoparticle arrays," *Journal Of Optics A-Pure And Applied Optics* **7**, pp. S110–S117, 2005.

[46] C. Tabor, R. Murali, M. Mahmoud, and M. A. El-Sayed, "On the use of plasmonic nanoparticle pairs as a plasmon ruler: The dependence of the near-field dipole plasmon coupling on nanoparticle size and shape," *Journal of Physical Chemistry A* **113**, pp. 1946–1953, 2008.

[47] P. K. Jain, W. Huang, and M. A. El-Sayed, "On the universal scaling behavior of distance decay of plasmon coupling in metal nanoparticle pairs: A plasmon ruler equation," *Nano Letters* **7**, pp. 2080–2088, 2007.

[48] P. Olk, J. Renger, M. T. Wenzel, and L. M. Eng, "Distance dependent spectral tuning of two coupled metal nanoparticles," *Nano Letters* **8**, pp. 1174–1178, 2008.

[49] C. L. Haynes, A. D. McFarland, L. Zhao, R. P. V. Duyne, G. C. Schatz, L. Gunnarsson, J. Prikulis, B. Kasemo, and M. Käll, "Nanoparticle optics: The importance of radiative dipole coupling in two-dimensional nanoparticle arrays," *Journal of Physical Chemistry B* **107**, pp. 7337–7342, 2003.

[50] B. Lamprecht, G. Schider, R. T. Lechner, H. Ditlbacher, J. R. Krenn, A. Leitner, and F. R. Aussenegg, "Metal nanoparticle gratings: Influence of dipolar particle interaction on the plasmon resonance," *Physical Review Letters* **84**, pp. 4721–4724, 2000.

[51] M. W. Knight, Y. Wu, J. B. Lassiter, and P. Nordlander, "Substrates matter: Influence of an adjacent dielectric on an individual plasmonic nanoparticle," *Nano Letters* **9**(5), pp. 2188–2192, 2009.

[52] I. Freestone, N. Meeks, M. Sax, and C. Higgett, "The Lycurgus Cup - a Roman nanotechnology," *Gold Bulletin* **40**(7), pp. 270–277, 2007.

[53] G. Mie, "Beitrge zur optik trber medien, speziell kolloidaler metallsungen," *Annalen der Physik, Series IV* **25**(3), pp. 377–345, 1908. English translation by Patricia Newman, Sandia Labs, 1978.

[54] M. D. McMahon, D. Ferrara, C. Bowie, R. Lopez, and R. F. Haglund, Jr., "Second harmonic generation from resonantly excited arrays of gold nanoparticles," *Applied Physics B* **87**, pp. 259–265, 2007.

[55] A. N. Lebedev, M. Gartz, U. Kreibig, and O. Stenzel, "Optical extinction by spherical particles in an absorbing medium: Application to composite absorbing films," *European Physical Journal D* **6**, pp. 365–373, 1999.

[56] A. Wokaun, "Surface-enhanced electromagnetic processes," *Solid State Physics* **38**, pp. 223–294, 1984.

[57] U. Kreibig, "Interface-induced dephasing of mie plasmon polaritons," *Applied Physics B* **93**, pp. 79–89, 2008.

[58] P. Nordlander, E. Prodan, K. Li, and M. I. Stockman, "Plasmon hybridization in nanoparticle dimers," *Nano Letters* **4**(5), pp. 899–903, 2004.

[59] H. Kuwata, H. Tamaru, K. Esumi, and K. Miyano, "Resonant light scattering from metal nanoparticles Practical analysis beyond Rayleigh approximation," *Applied Physics Letters* **83**(22), pp. 4625–4628, 2003.

[60] C. Kittel, *Introduction to Solid State Physics, 8th ed.*, John Wiley and Sons, New York, 2005.

[61] J. D. Jackson, *Classical Electrodynamics*, John Wiley & Sons, Inc., New York, NY, 3rd ed., 1999.

[62] P. Drude, "Zur elektronentheorie der metalle," *Annalen der Physik* **306**(3), pp. 566–613, 1900.

[63] P. Drude, "Zur elektronentheorie der metalle; II. Teil. galvanomagnetische und thermomagnetische effecte," *Annalen der Physik* **308**(11), pp. 369–402, 1900.

[64] P. Johnson and R. Christy, "Optical constants of the noble metals," *Physical Review B* **6**, pp. 4370–4379, 1972.

[65] A. D. Rakić, A. B. Djurišić, J. M. Elazar, and M. L. Majewski, "Optical properties of metallic films for vertical-cavity optoelectronic devices," *Applied Optics* **37**(22), pp. 5271–5283, 1998.

[66] M. D. McMahon, R. Lopez, H. M. Meyer, III, L. C. Feldman, and R. F. Haglund, Jr., "Rapid tarnishing of silver nanoparticles in ambient laboratory air," *Applied Physics B* **80**, pp. 915–921, 2005.

[67] G. K. Pribil, B. Johs, and N. J. Ianno, "Dielectric function of thin metal films by combined in situ transmission ellipsometry and intensity measurements," *Thin Solid Films* **455-456**, pp. 443–449, 2004.

[68] P. G. Etchegoin, E. C. L. Ru, and M. Meyer, "An analytic model for the optical properties of gold," *Journal of Chemical Physics* **125**, p. 164705, 2006.

[69] F. Hao and P. Nordlander, "Efficient dielectric function for fdtd simulation of the optical properties of silver and gold nanoparticles," *Chemical Physics Letters* **446**, p. 115, 2007.

[70] E. Dagotto and Y. Tokura, "Strongly correlated electronic materials: Present and future," *MRS Bulletin* **33**, pp. 1037–1045, 2008.

[71] C. Chen and Z. Zhou, "Optical phonons assisted infrared absorption in VO_2 based bolometer," *Applied Physics Letters* **91**, p. 011107, 2007.

[72] S. Chen, H. Ma, X. Yi, T. Xiong, H. Wang, and C. Ke, "Smart VO_2 thin film for protection of sensitive infrared detectors from strong laser radiation," *Sensors and Actuators A* **115**, pp. 28–31, 2004.

[73] W. Wang, Y. Luo, D. Zhang, and F. Luo, "Dynamic optical limiting experiments on vanadium dioxide and vanadium pentoxide thin films irradiated by a laser beam," *Applied Optics* **45**(14), pp. 3378–3381, 2006.

[74] M. Soltani, M. Chaker, E. Haddad, R. V. Kruzelesky, and D. Nikanpour, "Optical switching of vanadium dioxide thin films deposited by reactive pulsed laser deposition," *Journal of Vacuum Science and Technology A* **22**(3), pp. 859–864, 2004.

[75] M. Soltani, M. Chaker, E. Haddad, and R. Kruzelesky, "1×2 optical switch devices based on semiconductor-to-metallic phase transition characteristics of VO_2 smart coatings," *Measurement Science and Technology* **17**, pp. 1052–1056, 2006.

[76] F. J. Morin, "Oxides which show a metal-to-insulator transition at the Neel temperature," *Physical Review Letters* **3**, pp. 34–36, 1959.

[77] J. B. Goodenough, "Direct cation–cation interactions in several oxides," *Physical Review* **117**, p. 1442, 1960.

[78] A. Zylbersztejn and N. F. Mott, "Metal insulator transition in vanadium dioxide," *Physical Review B* **11**(11), pp. 4383–4395, 1975.

[79] V. A. Lobastov, J. Weissenrieder, J. Tang, and A. H. Zewail, "Four-dimensional imaging and diffraction of nanostructures during phase transitions," *Nano Letters* **7**(9), pp. 2552–2558, 2007.

[80] A. Cavalleri, C. Tóth, C. W. Siders, and J. A. Squier, "Femtosecond structural dynamics in VO_2 during an ultrafast solid-solid phase transition," *Physical Review Letters* **87**(23), p. 237401, 2001.

[81] A. Cavalleri, T. Dekorsy, H. H. W. Chong, J. C. Kieffer, and R. W. Schoenlein, "Evidence for a structurally-driven insulator-to-metal transition in VO_2: A view from the ultrafast timescale," *Physical Review B* **70**, p. 161102(R), 2004.

[82] M. M. Qazilbash, M. Brehm, B.-G. Chae, P.-C. Ho, G. O. Andreev, B.-J. Kim, S. J. Yun, A. V. Balatsky, M. B. Maple, F. Keilmann, H.-T. Kim, and D. N. Basov, "Mott transition in VO_2 revealed by infrared spectroscopy and nano-imaging," *Science* **318**, p. 1750, 2007.

[83] J. Wei, Z. Wang, W. Chen, and D. H. Cobden, "New aspects of the metal-insulator transition in single-domain vanadium dioxide nanobeams," *Nature Nanotechnology* , p. DOI: 10.1038/NNANO.2009.141, 2009.

[84] J. G. Ramírez, A. Sharoni, Y. Dubi, M. E. Gómez, and I. K. Schuller, "First-order reversal curve measurements of the metal-insulator transition in VO_2: Signatures of persistent metallic domains," *Physical Review B* **79**, p. 235110, 2009.

[85] D. Ruzmetov, S. D. Senanayake, V. Narayanamurti, and S. Rananathan, "Correlation between metal-insulator transition characteristics and electronic structure changes in vanadium dioxide thin films," *Physical Review B* **77**, p. 195442, 2008.

[86] G. Gopalakrishnan and D. Ruzmetov, "On the triggering mechanism for the metal-insulator transition in thin film VO_2 devices: electric field versus thermal effects," *Journal of Material Science* **44**, pp. 5345–5353, 2009.

[87] S. Lysenko, A. Rua, F. Fernandez, and H. Liu, "Optical nonlinearity and structural dynamics of VO_2," *Journal of Applied Physics* **105**, p. 043502, 2009.

[88] P. U. Jepsen, B. M. Fischer, A. Thoman, H. Helm, J. Y. Suh, R. Lopez, and R. F. Haglund, Jr., "Metal-insulator transition in a VO_2 thin film observed with terahertz spectroscopy," *Physical Review B* **74**, p. 205103, 2006.

[89] J. Sakai and M. Kuriso, "Effect of pressure on the electric-field-induced resistance switching of VO_2 planar-type junctions," *Physical Review B* **78**, p. 033106, 2008.

[90] M. F. Becker, A. B. Buckman, R. M. Walser, T. Lépine, P. Georges, and A. Brun, "Femtosecond laser excitation of the semiconductor-metal phase transition in VO_2," *Applied Physics Letters* **65**(12), pp. 1507–1509, 1994.

[91] M. F. Becker, A. B. Buckman, R. M. Walser, T. Lépine, P. Georges, and A. Brun, "Femtosecond laser excitation dynamics of the semiconductor-metal phase transition in VO_2," *Journal of Applied Physics* **79**(5), pp. 2404–2408, 1996.

[92] A. Cavalleri, M. Rini, H. H. W. Chong, S. Fourmaux, T. E. Glover, P. A. Heimann, J. C. Kieffer, and R. W. Schoenlein, "Band-selective measurements of electron dynamics in VO_2 using femtosecond near-edge x-ray absorption," *Physical Review Letters* **95**, p. 067405, 2005.

[93] C. Kübler, H. Ehrke, R. Huber, R. Lopez, A. Halabica, R. F. Haglund, Jr., and A. Leitenstorfer, "Coherent structural dynamics and electronic correlations during an ultrafast insulator-to-metal phase transition in VO_2," *Physical Review Letters* **99**, p. 116401, 2007.

[94] S. Lysenko, A. Rua, V. Vikhnin, F. Fernández, and H. Liu, "Insulator-to-metal phase transition and recovery processes in VO_2 thin films after femtosecond laser excitation," *Physical Review B* **76**, p. 035104, 2007.

[95] S. Biermann, A. Poteryaev, A. I. Lichtenstein, and A. Georges, "Dynamical singlets and correlation-assisted peierls transition in VO_2," *Physical Review Letters* **94**, p. 026404, 2005.

[96] J. M. Tomczak and S. Biermann, "Effective band structure of correlated materials: the case of VO_2," *Journal of Physics: Condensed Matter* **14**, p. 251, 2007.

[97] M. W. Haverkort, Z. Hu, A. Tanaka, W. Reichelt, S. V. Streltsov, M. A. Korotin, V. I. Anisimov, H. H. Hsieh, H. J. Lin, C. T. Chen, D. I. Khomskii, and L. H. Tjeng, "Orbital-assisted metal-insulator transition in VO_2," *Physical Review Letters* **95**, p. 196404, 2005.

[98] P. Baum, D. S. Yang, and A. H. Zewail, "4D visualization of transitional structures in phase transformations by electron diffraction," *Science* **318**, p. 788, 2007.

[99] J. Rozen, R. Lopez, R. F. Haglund, Jr., and L. C. Feldman, "Two-dimensional current percolation in nanocrystalline vanadium dioxide films," *Applied Physics Letters* **88**, p. 081902, 2006.

[100] A. Sharoni, J. G. Ramírez, and I. K. Schuller, "Multiple avalanches across the metal-insulator transition of vanadium oxide nanoscaled junctions," *Physical Review Letters* **101**, p. 026404, 2008.

[101] H. Kakiuchida, P. Jin, S. Nakao, and M. Tazawa, "Optical properties of vanadium dioxide film during semiconductive-metallic phase transition," *Japanese Journal of Applied Physics* **46**(5), pp. L113–L116, 2007.

[102] M. Nagashima and H. Wada, "Near infrared optical properties of laser ablated VO_2 thin films by ellipsometry," *Thin Solid Films* **312**, pp. 61–65, 1998.

[103] R. T. Kivaisi and M. Samiji, "Optical and electrical properties of vanadium dioxide films prepared under optimized rf sputtering conditions," *Solar Energy Materials and Solar Cells* **57**, pp. 141–152, 1999.

[104] E. U. Donev, J. Y. Suh, E. Villegas, R. Lopez, R. F. Haglund, Jr., and L. C. Feldman, "Optical properties of subwavelength hole arrays in vanadium dioxide thin films," *Physical Review B* **73**, p. 201401(R), 2006.

[105] S. Szunerits, V. G. Praig, M. Manesse, and R. Boukherroub, "Gold island films on indium tin oxide for localized surface plasmon sensing," *Nanotechnology* **19**(19), p. 195712, 2008.

[106] J. Bartella, J. Schroeder, and K. Witting, "Characterization of ITO- and TiO_xN_y films by spectroscopic ellipsometry, spectraphotometry, and XPS," *Applied Surface Science* **179**(1-4), pp. 181–190, 2001.

[107] G. Franz, B. Lange, and S. Sotier, "Characterization of sputtered indium tin oxide layers as transparent contact material," *Journal Vacuum Science and Technology A* **19**(5), pp. 2514–2521, 2001.

[108] PMMA and EBL technology have become highly standardized. The MicroChem website (`http://www.microchem.com/products/pmma.htm`) offers much documentation for the process.

[109] E. P. Rai-Choudhury, *SPIE Handbook of Microlithography, Micromachining, and Microfabrication, Volume 1: Microlithography*, SPIE Press, 1997. As of the time of this writing, the chapter on electron-beam lithography techniques is available online at `http://www.cnf.cornell.edu/cnf_spietoc.html`.

[110] C. Vieu, F. Carcenac, A. Ppin, Y. Chen, M. Mejias, A. Lebib, L. Manin-Ferlazzo, L. Couraud, and H. Launois, "Electron beam lithography: resolution limits and applications," *Applied Surface Science* **164**(1-4), pp. 111–117, 2000.

[111] D. B. Chrisey and G. K. Hubler, *Pulsed Laser Deposition of Thin Films*, Wiley-Interscience, New York, 1994.

[112] R. Eason, ed., *Pulsed Laser Deposition of Thin Films: Applications-Led Growth of Functional Materials*, John Wiley and Sons, Inc., New York, 2007.

[113] J. Nag and R. F. Haglund, Jr., "Synthesis of vanadium dioxide thin films and nanoparticles," *Journal of Physics: Condensed Matter* **20**, p. 264016, 2008.

[114] J. Y. Suh, R. Lopez, L. C. Feldman, and R. F. Haglund, Jr., "Semiconductor to metal phase transition in the nucleation and growth of VO_2 nanoparticles and thin films," *Journal of Applied Physics* **96**, p. 1209, 2004.

[115] A. Savitzky and M. J. E. Golay, "Smoothing and differentiation of data by simplified least-squares procedures," *Analytical Chemistry* **36**(8), p. 16271639, 1964.

[116] C. F. Bohren and D. P. Gilra, "Extinction by a spherical particle in an absorbing medium," *Journal of Colloid Interface Science* **72**, pp. 215–221, 1979.

[117] G. Videen and W. Sun, "Yet another look at light scattering from particles in absorbing media," *Applied Optics* **42**(33), pp. 6724–6727, 2003.

[118] K. S. Yee, "Numerical solution of initial boundary value problems involving Maxwell's equations in isotropic media," *IEEE Transactions on Antennas and Propagation* **14**, pp. 302–307, 1966.

[119] A. Taflove, "Review of formulation and applications of the finite-difference time-domain method for numerical modeling of electromagnetic wave interactions with arbitrary structures," *Wave Motion* **10**, pp. 547–582, 1988.

[120] Much of the information here is from discussions with Lumerical representatives at their training program, October 2009, Vancouver, BC, and from their website, `http://www.lumerical.com`.

[121] K. L. Shlager and J. B. Schneider, "A selective survey of finite-difference time-domain literature," *IEEE Antennas and Propagation Magazine* **37**(4), pp. 39–56, 1995.

[122] T. J. R. Hughes, *The Finite Element Method: Linear, Static, and Dynamic Finite Element Analysis*, Dover Publications, Inc., Mineola, New York, 2000.

[123] J. C. Miller and R. F. Haglund, *Laser Ablation and Desorption, Volume 30: Experimental Methods in the Physical Sciences*, Academic Press, San Diego, CA, 1998.

[124] S. A. Maier and H. A. Atwater, "Plasmonics: Localization and guiding of electromagnetic energy in metal/dielectric structures," *Journal of Applied Physics* **98**, p. 011101, 2005.

[125] C. Sönnichsen, T. Franzl, T. Wilk, G. v. Plessen, J. Feldmann, O. Wilson, and P. Mulvaney, "Drastic reduction of plasmon damping in gold nanorods," *Physical Review Letters* **88**(7), p. 077402, 2002.

[126] L. Zhao, K. L. Kelly, and G. C. Schatz, "The extinction spectra of silver nanoparticle arrays: Influence of array structure on plasmon resonance wavelength and width," *Journal of Physical Chemistry B* **107**, pp. 7343–7350, 2003.

[127] B. N. Khlebtsov and N. G. Khlebtsov, "Multipole plasmons in metal nanorods: Scaling properties and dependence on particle size, shape, orientation, and dielectric environment," *Journal of Physical Chemistry C* **111**, pp. 11516–11527, 2007.

[128] F. Zhou, Z.-Y. Li, Y. Liu, and Y. Xia, "Quantitative analysis of dipole and quadrupole excitation in the surface plasmon resonance of metal nanoparticles," *Journal of Physical Chemistry C* **112**, pp. 20233–20240, 2008.

[129] W. Rechberger, A. Hohenau, A. Leitner, J. Krenn, B. Lamprecht, and F. Aussenegg, "Optical properties of two interacting gold nanoparticles," *Optical Communications* **220**, pp. 137–141, 2003.

[130] A. Bouhelier, R. Bachelot, J. S. Im, and G. P. Wiederrecht, "Electromagnetic interactions in plasmonic nanoparticle arrays," *Journal of Physical Chemistry B* **109**, pp. 3195–3198, 2005.

[131] C. Dahmen, B. Schmidt, and G. von Plessen, "Radiation damping in metal nanoparticle pairs," *Nano Letters* **7**, pp. 318–322, 2007.

[132] J. Zuloaga, E. Prodan, and P. Nordlander, "Quantum description of the plasmon resonances of a nanoparticle dimer," *Nano Letters* **9**(2), pp. 887–891, 2009.

[133] R. A. Dynich, A. N. Ponyavina, and V. V. Filippov, "Local field enhancement near spherical nanoparticles in absorbing media," *Journal of Applied Spectroscopy* **76**(5), pp. 705–710, 2009.

[134] E. Prodan, C. Radloff, N. J. Halas, and P. Nordlander, "A hybridization model for the plasmon responce of complex nanostructures," *Science* **302**, pp. 419–422, 2003.

[135] These simulations were done using OptiFDTD® software, version 5, by Optiwave.

[136] D. J. Hilton, R. P. Prasankumar, S. Fourmaux, A. Cavalleri, D. Brassard, M. A. E. Khakani, J. C. Kieffer, A. J. Taylor, and R. D. Averitt, "Enhanced photosusceptibility near T_c for the light-induced insulator-to-metal phase transition in vanadium dioxide," *Physical Review Letters* **99**, p. 226401, 2007. Also, erratum published at PRL 100, 019906 (2008).

[137] S. Lysenko, A. J. Rua, V. Vikhnin, F. Fernandez, and H. Liu, "Light-induced ultrafast phase transitions in VO_2 thin film," *Applied Surface Science* **252**, pp. 5512–5515, 2006.

[138] H. S. Carslaw and J. C. Jaeger, *Conduction of Heat in Solids, Second Edition*, Oxford University Press, New York, NY, 2008.

[139] M. A. Nogninov, G. Zhu, M. Bahoura, J. Adegoke, C. Small, B. A. Ritzo, V. P. Drachev, and V. M. Shalaev, "The effect of gain and absorption on surface plasmons in metal nanoparticles," *Applied Physics B* **86**, pp. 455–460, 2007.

[140] M. A. Nogninov, G. Zhu, M. Bahoura, J. Adegoke, C. Small, B. A. Ritzo, V. P. Drachev, and V. M. Shalaev, "Enhancement of surface plasmons in ag aggregate by optical gain in a dielectric medium," *Optics Letters* **31**(20), pp. 3022–3024, 2006.

[141] A. Y. Smuk and N. M. Lawandy, "Spheroidal particle plasmons in amplifying media," *Applied Physics B* **84**, pp. 125–129, 2006.

[142] S. Sheikholeslami, Y. Jun, P. K. Jain, and A. P. Alivisatos, "Coupling of optical resonances in a compositionally asymmetric plasmonic nanoparticle dimer," *Nano Letters* **10**, p. 26552660, 2010.

[143] J. Nag, R. F. Haglund, Jr., E. A. Payzant, and K. L. More, "Room temperature vs. high temperature grown epitaxial VO_2 films for better nanoscale applications," In preparation.

[144] J. Nag, R. F. Haglund, Jr., E. A. Payzant, and K. L. More, "Non-congruence of thermally driven structural and electronic transitions in vanadium dioxide," 2010. In preparation; arXiv: 1003.3876.

[145] I. I. Smolyaninov and E. E. Narimanov, "Metric signature transitions in optical metamaterials," *Physical Review Letters* **105**, p. 067402, 2010.